Land Surface Fluxes in Natural and Urban Landscapes in Arid and Semiarid Regions

by

Elí Rafael Pérez Ruiz

A Dissertation Presented in Partial Fulfillment
of the Requirements for the Degree
Doctor of Philosophy

Approved October 2021 by the
Graduate Supervisory Committee:

Enrique R. Vivoni, Chair
Osvaldo E. Sala
Heather L. Throop
Kelin X. Whipple
Enrico A. Yepez

ARIZONA STATE UNIVERSITY

December 2021

ABSTRACT

In arid and semiarid areas of the southwestern United States and northwestern México, water availability is the main control on the interactions between the land surface and the atmosphere. Seasonal and interannual variations in water availability regulate the response of water and carbon dioxide fluxes in natural and urban landscapes. However, despite sharing a similar dependance to water availability, landscape characteristics, such as land cover heterogeneity, landscape position, access to groundwater, microclimatic conditions, and vegetation functional traits, among others, can play a fundamental role in modulating the interactions between landscapes and the atmosphere. In this dissertation, I study how different landscape characteristics influence the response of water and carbon dioxide fluxes in arid and semiarid urban and natural settings. The study uses the eddy covariance technique, which calculates the vertical turbulent fluxes within the boundary layer, to quantify water, energy, and carbon dioxide fluxes within local patches. Specifically, the study focused on three main scopes: (1) how vegetation, anthropogenic activity, and water availability influence carbon fluxes in four urban landscapes in Phoenix, Arizona, (2) how access to groundwater and soil-microclimate conditions modulate the flux response of three natural ecosystems in northwestern México during the North American monsoon, and (3) how the seasonal hydrologic partitioning in a watershed with complex terrain regulates the carbon dioxide fluxes of a Chihuahuan Desert shrubland. Results showed a differential response of landscapes according to their land cover composition, access to groundwater or functional traits. In Chapter 2, in urban landscapes with irrigation, vegetation activity can counteract carbon dioxide emissions during the day, but anthropogenic sources from the

built environment dominate the carbon dioxide fluxes overall. In Chapter 3, across an elevation-groundwater access gradient, low elevation ecosystems showed intensive water use strategies linked to a dependance to shallow or intermittent access to soil moisture, while a high elevation ecosystem showed extensive water use strategies which depend on a reliable access to groundwater. Finally, in Chapter 4, the mixed shrubland in complex terrain showed an evenly distributed bimodal vegetation productivity which is supported by an abundant water availability during wet seasons and by carry-over moisture in deeper layers of the soil during the dry season. The results from this dissertation highlight how different forms of water availability are responsible for the activity of vegetation which modulates land surface fluxes in arid and semiarid settings. Furthermore, the outcomes of this dissertation help to understand how landscape properties regulate the flux response to water availability in urban and natural areas.

DEDICATION

I dedicate this dissertation to my two sons, Abdel Eli and Rafael Antonio. My love for you is infinite. Everything I am is because of you. You are the main reason I keep moving forward.

ACKNOWLEDGEMENTS

First, I would like to thank my advisor, Prof. Enrique R. Vivoni, for all the support, guidance, empathy, patience, advice, and friendship. I could not have a better advisor in this hard road I decided to follow. I would like to thank my dissertation committee, Prof. Osvaldo E. Sala, Prof. Heather Throop, Prof. Kelin X. Whipple, and Prof. Enrico Yepez for all the support and comments that helped me improve my research, but overall, helped to find the right path when I thought I was lost.

I would like to thank all the past and current members of the ASU Hydrologic Science, Engineering and Sustainability research group who directly or indirectly helped me through my Ph.D., including Nolie Templeton, Adam Schreiner-McGraw, Kristen Whitney, Eric Escoto, Zhaocheng Wang, Zac Keller, Mercedes Kindler, Josh Cederstrom, Luisa Orci, Charles Kimsal and Agustin Robles-Morúa. I also would like to thank all the people involved in the SRER or JER, especially Dr. Russell Scott, John Anderson and David Thatcher.

I want to thank Mary Triny for all the support during the last 14 years. This journey could not be possible without your help and support. Thanks to my family for all the unconditional love and support.

Finally, I would like to acknowledge financial support of the Fulbright Foreign Student Program, the Consejo Nacional de Ciencia y Tecnología de México, and the Programa de Desarrollo Profesional Docente SES-SEP through all my Ph.D., as well as the Jornada Basin Long-Term Ecological Research Program (DEB 2025166), the Central Arizona-Phoenix LTER and the University of Arizona for additional financial support.

TABLE OF CONTENTS

Page

APPENDIX Page

LIST OF TABLES

Table Page

Table Page

Table Page

LIST OF FIGURES

Figure Page

Figure Page

Figure Page

Figure Page

Figure Page

Figure Page

Figure Page

CHAPTER 1

INTRODUCTION

Motivation

In arid and semiarid landscapes, biophysical processes of water-limited ecosystems are controlled by water availability, which respond to the onset and demise of water input through changes in pulses of microbial activity, leaf and canopy development, and plant photosynthesis (Noy-Meir, 1973; Reynolds et al., 2000; 2004; Méndez-Barroso et al., 2014; Biederman et al., 2018; Verduzco et al., 2018). In southwestern US and northwestern México, water input in ecosystems occur during the winter and summer seasons, generating a bimodal regime of water availability (Sponseller et al., 2012). During the summer, the North American Monsoon (NAM) dominates the water input through a substantial increase of rainfall from July to September and combined with a higher radiation and atmospheric water demand, leads to generalized changes in ecosystem conditions and land-atmosphere interactions as well as higher water losses (Adams & Comrie, 1997; Méndez-Barroso & Vivoni, 2010; Pérez-Ruiz et al., 2010, 2021; Vivoni et al., 2007, 2008, 2010; Forzieri et al., 2011). Contrary, lower intensity rainfall events during the winter, when radiation and atmospheric water demand are much lower, favor the storage of water in deeper layers of the soil (Wilcox et al., 2006; Anderson-Teixeira et al., 2011; Scott and Biederman, 2019). As a result, biogeochemical processes in arid and semiarid landscapes are closely tied to the hydrological cycle, particularly the water, energy and carbon fluxes between the land surface and the atmosphere (Huxman et al., 2004; Scott et al., 2006; Williams et al., 2006; Lohse et al., 2009; Yahdjian et al., 2011).

Despite a clear dependance of biophysical processes to precipitation and water availability, landscapes characteristics can clearly influence the differential response of ecosystems to water availability, not only in total amounts of water input but also in timing and seasonality of water availability (Barron-Gafford et al., 2013; Pérez-Ruiz et al., 2020). Landscape controls, such topographical position, elevation, complex terrain, access to groundwater, microclimatic conditions or land cover heterogeneity, can play a fundamental role in differentiating the individual responses of ecosystems, either by defining the phenological traits or strategies of vegetation or by defining the land surface actors which contributes to the mass and energy exchanges (Barron-Gafford et al., 2013; Jia et al., 2014; Rodríguez-Iturbe et al., 2001; Rodríguez-Robles et al., 2017; Scott et al., 2014; Shao et al., 2016; Wang et al., 2011, 2016; Pérez-Ruiz et al., 2021). In this dissertation, the influence of different landscape characteristics on land surface-atmosphere fluxes is explored, especially the response of water and carbon dioxide fluxes in arid and semiarid urban and natural settings and the relationship between them. In particular, the dissertation focusses in the analysis of three different landscape controls in water and carbon fluxes in arid and semiarid landscapes: (1) how different land covers contribute or influence the carbon fluxes within four urban landscapes?; (2) how elevation-induced landscape characteristics affect the water-energy carbon fluxes?; and (3) how the seasonal hydrologic partitioning affect vegetation productivity in a landscape with complex terrain?.

Changes in land surface characteristics due to urbanization have a clear impact in local energy, water, and carbon dioxide fluxes (Oke, 1988; Mills, 2007; Velasco and Roth, 2010; Chow et al., 2014). In arid and semiarid regions, the trend in urbanization is

even more pronounced than in other climate settings, which is crucial since about 30% of the global population is currently residing in cities in arid and semiarid climates (White et al.,2003; Georgescu et al., 2012; Lazzarini et al., 2015). Urban areas are generally considered net sources of carbon dioxide to the atmosphere due to fluxes being controlled by anthropogenic emissions, such as fuel combustion from vehicles, industries, and buildings, rather than by biological processes (Pataki et al., 2006; Vogt et al., 2006; Kordowski and Kuttler, 2010; Crawford et al., 2011). However, urban vegetation could potentially counteract anthropogenic emissions, as urban vegetation effect is modulated by the amount of available water, provided in arid and semiarid cities through irrigation (Velasco et al., 2013, 2016; Volo et al., 2014, 2015; McHale et al., 2017).

Water-limited ecosystems in the NAM area have a strong connection with the temporal distribution of rainfall, which strongly affects the exchange of water, energy, and carbon with the atmosphere (Méndez-Barroso et al., 2014; Scott et al., 2010; Verduzco et al., 2018). A wide-spread vegetation greening as a result of the synchronized availability of rainfall and solar radiation is thought to be a controlling factor on water-energy-carbon fluxes (Forzieri et al., 2011, 2014; Méndez-Barroso et al., 2014; Vivoni et al., 2010). However, it is not well known how variations in access to groundwater and elevation-induced microclimatic and soil conditions might modulate the individual response of ecosystems, as vegetation traits linked to intensive and extensive water use dominate the ecosystem phenological response during the summer season in a groundwater access and elevation gradient (Barron-Gafford et al., 2013; Jia et al., 2014; Lagergren et al., 2008; Rodríguez-Iturbe et al., 2001; Scott et al., 2014; Shao et al., 2016; Wang et al., 2011, 2016).

Vegetation productivity in arid and semiarid landscapes is controlled by water availability, and seasonality variations of water input and sources may have a greater impact modulating the productivity of ecosystems rather than total annual rainfall, especially in landscape with complex terrain, where hydrologic partitioning can constrains the availability and use of water by vegetation (Noy-Meir, 1973; Reynolds et al., 2004; Scott et al., 2015; Biederman et al., 2016, 2018; Jia et al., 2016 Ukkola et al., 2021). The regime of hydrological and ecological processes in the shrublands of the Chihuahuan Desert offers an excellent opportunity to explore the seasonal dynamics of the water balance and carbon fluxes, as some shrubland ecosystems follow a bimodal productivity regime that is controlled both by the winter and summer seasons, characterized by high intensity, localized convective storms during the summer which lead to higher water input and water use and a high ecosystem productivity, and lower intensity, widespread frontal storms during the winter, which favor the water storage into deeper soil layers but may still support ecosystem productivity and water use within that season (Anderson-Teixeira et al., 2011; Sponseller et al., 2012 ; McKenna and Sala; Scott and Biederman, 2019).

The study of the Earth's biogeochemistry and hydrology involves quantifying the flows of matter in and out of the atmosphere, and even when several techniques exist to study the biosphere-atmosphere exchange, the Eddy Covariance (EC) technique has become the most used method to measure water-energy-carbon fluxes (Baldocchi et al., 2001; Balcocchi, 2003, 2008). The EC method allows the direct measurement of mass and energy fluxes over several timescales (hours to years) over a relatively large area of land and has the potential of quantifying the whole ecosystem response to climate and

phenological variability (Baldocchi et al., 2001). When paired with ancillary measurements and/or characterization of the study site, the EC technique can be used to assess a wide range of questions such as the effects of disturbance, stand age, plant functional type, meteorological effects, or landscape controls (Badocchi, 2003). While the EC technique application has been typically restricted to periods when atmospheric conditions are steady and to locations with relatively flat terrain and vegetation that extends horizontally about 100 times the sampling height, this technique has also been used to assess landscapes with high heterogeneity, such as urban setting (Grimmond and Christen, 2012). In this dissertation, land surface-atmosphere fluxes are measured using the EC technique in order to assess the next goals:

Chapter 2:

1. Quantify and compare carbon fluxes over different urban land cover types of Phoenix, AZ, in relation to a location that provided reference meteorological conditions during the study period.
2. Relate the observed differences to measures of anthropogenic emissions, plant photosynthetic activity, and meteorological forcing in each urban landscape.
3. Determine the role of precipitation events and outdoor water use on modifying carbon fluxes across urban landscapes.

Chapter 3:

1. Quantify land-atmosphere interactions during the evolution of the NAM to elucidate if elevation-induced soil and microclimate conditions or groundwater access linked to the terrain position play a more significant role in the response of three ecosystem in northwestern México.

Chapter 4.

1. Determine the links between net ecosystem production and water availability in the winter and summer seasons in a mixed shrubland of the Chihuahuan Desert.
2. Analyze the effect seasonal variations of gross primary productivity and ecosystem respiration over the carbon balance in a mixed shrubland of the Chihuahuan Desert.
3. Determine the influence of summer season precipitation proportion on the annual net ecosystem production in a mixed shrubland of the Chihuahuan Desert.

Chapter Outline

This dissertation intends to advance the knowledge of how the different landscape characteristics affect or modulate the biosphere-atmosphere exchange in arid and semiarid areas, in particular the water, energy and carbon fluxes.

In Chapter 2, carbon fluxes in four different urban landscape in the Phoenix Metropolitan Area are compared and analyzed in relationship to anthropogenic and vegetation activity as well as meteorological forcing. The urban landscapes represent a mesic landscape (Local Climate Zone 9, LCZ 9), which represents a highly vegetated land cover, a parking lot (LCZ 8), which represents a highly urbanized land cover, and a xeric landscape (LCZ 5) and a suburban neighborhood (LCZ 6) which represent heterogeneous land covers. Measurements were done using an EC system attached to a mobile tower and diurnal, daily, and seasonal variations of carbon fluxes were related to anthropogenic and biogenic processes that lead to sources and sinks of CO_2 in urban environments. Vehicular influence was done by analyzing carbon fluxes separately for

weekdays and weekends and in relation to traffic counts for nearby streets to the deployments as well as to the areal fraction of pavement classified for each site. Vegetation activity was analyzed through the fraction of trees and grasses at each site as well as vegetation indices and by comparing carbon fluxes for sunny and cloudy days. Finally, to determine if the carbon fluxes were different between selected days (i.e., weekday versus weekend or sunny versus cloudy), statistical tests were performed, and a similar procedure was conducted to quantify the effect of wet versus dry conditions.

In Chapter 3, landscape controls on water, energy and carbon fluxes are evaluated in an elevation and groundwater access gradient are evaluated in different ecosystems in the area of the NAM in northwestern México. Gradients in terrain conditions in northwest México can help explore this dependence as different ecosystems experience rainfall during the NAM but can have variations in groundwater access as well as in soil and microclimatic conditions that depend on elevation. A field campaign was conducted during the summer of 2017, and water, energy and carbon fluxes as well as ancillary meteorological measurements were obtained in three different ecosystems, a subtropical scrubland representing a low elevation ecosystem with no access to groundwater, a riparian mesquite representing a low elevation ecosystem with intermittent access to groundwater, and an oak savanna representing a high elevation ecosystem with stable groundwater access. Datasets during the NAM season of 2017 were placed into a wider context using previous EC measurements, nearby rainfall data, and remotely-sensed products and differences in soil, vegetation, and meteorological variables, as well as latent and sensible heat fluxes and carbon budget components were characterized. To evaluate the effects of landscape controls, we calculated the Inherent Water Use

Efficiency, the Evaporative Index, and the evapotranspiration from groundwater index at each site, as well as a path analysis to explore the direct and indirect relations between environmental conditions and fluxes.

Chapter 4 investigates the seasonal dynamics in hydrological partitioning and its relation to primary productivity in a heavily instrumented small first-order watershed in a mixed shrubland of the Chihuahuan Desert. Here, we analyze the seasonal distributions of water balance components and carbon fluxes over a 10-year period. Carbon fluxes and water balance elements were measurements or estimated. To analyze the seasonality, we divided each year in two seasons that represent dry (January to June) and wet (July to December) periods, each with six months. Water balance components and carbon fluxes were compared across the dry and wet seasons and the relationship between water and carbon fluxes was assessed through correlations between annual, dry season, and wet season sums.

Finally, Chapter 5 recaps the general conclusions and future work from the chapters previously discussed. Chapter 2 to 4 correspond to three research papers published or submitted:

Chapter 2. Pérez-Ruiz, E.R., Vivoni, E.R., and Templeton, N.P., 2020. Urban land cover type determines the sensitivity of carbon dioxide fluxes to precipitation in Phoenix, Arizona. *PloS one*. 15(2). e0228537.

Chapter 3. Pérez-Ruiz, E.R., Vivoni, E.R., Yépez, E.A., Rodríguez, J.C., Gochis, D.J., Robles-Morua, A., Delgado-Balbuena, J., and Adams, D.K., 2021. Landscape controls on water-energy-carbon fluxes across different ecosystems during the North American monsoon. *Journal of Geophysical Research: Biogeosciences*. 126(5). e2020JG005809.

Chapter 4. Pérez-Ruiz, E.R., Vivoni, E.R., and Sala, O.E. Seasonal variation of water-carbon dynamics in a dryland ecosystem. (Submitted, *Ecosphere*).

CHAPTER 2

URBAN LAND COVER TYPE DETERMINES THE SENSITIVITY OF CARBON DIOXIDE FLUXES TO PRECIPITATION IN PHOENIX, ARIZONA

Introduction

Urbanization modifies land surface characteristics and impacts local energy, water, and carbon dioxide (CO_2) fluxes, particularly when large changes are made as compared to pre-existing conditions (Oke, 1988; Vitousek et al., 1997; Idso et al., 2002; Mills, 2007; Churkina, 2008; Velasco and Roth, 2010; Chow et al., 2014a,b; McHale et al., 2017). Cities are the most visible sign of global change and, despite their relatively small global areal fraction (2 to 5%), urban areas are responsible for >70% of the total CO_2 emissions from anthropogenic sources (Velasco and Roth, 2010; Crawford et al., 2011; Järvi et al.., 2012; Lui et al., 2012; Buckley et al., 2016; Helfter et al., 2016; Ueyama and Ando, 2016; Song et al., 2017). In arid and semiarid regions, the trend in urbanization is even more pronounced than in other climate settings, which is crucial since about 30% of the global population is currently residing in cities in arid and semiarid climates (White and Nackoney, 2003; Georgescu et al., 2012; Lazzarini et al., 2015). Furthermore, prior efforts have shown that urbanization in these regions significantly impacts CO_2 concentrations and emissions estimated for different land cover types (Idso et al., 2002; Velasco and Roth, 2010; Koerner and Klopatek, 2002, 2010).

CO_2 fluxes in urban areas are influenced by anthropogenic emissions, vegetation, and hydrometeorological factors such as precipitation and temperature. Most CO_2 fluxes in cities are controlled by fuel combustion from vehicles, industries and buildings, rather

than by biological processes (Pataki et al., 2006; Vogt et al., 2006; Kordowski and Kuttler, 2010; Velasco and Roth, 2010; Crawford et al., 2011; Ramamurty and Pardyjak, 2011; Hardiman et al., 2017; Sargent et al., 2018). As a result, urban areas are net sources of CO_2 to the atmosphere (Velasco et al., 2005,2014; Velasco and Roth, 2010; Bergeron and Strachan, 2011), though a high degree of spatiotemporal heterogeneity is present (Velasco and Roth, 2010; Christen et al., 2011; Crawford and Christen, 2014; Ramamurty and Pardyjak, 2015; Ueyama and Ando, 2016). Furthermore, the influence of point sources of CO_2 can play a disproportionate role as compared to natural ecosystems (Velasco and Roth, 2010; Hiller et al., 2011). Nevertheless, it is possible that urban vegetation can potentially have an important role in modulating CO_2 exchanges in cities by counteracting to some extent those positive fluxes through the photosynthetic activity of plants. This urban vegetation effect is modulated by the amount of available water, provided in arid and semiarid cities through irrigation (Chow et al., 2014a; Volo et al., 2014, 2015), and the availability of incoming solar radiation affected by cloud cover. The competing effects of anthropogenic emissions (sources) and plant-mediated CO_2 fixation (sinks) in arid cities are not well understood at present (Coutts et al., 2007; Bergeron and Strachan, 2011; Ramamurty and Pardyjak, 2011; McHale et al., 2017; Song et al., 2017; Ramamurty and Pardyjak, 2011; Velasco et al., 2013, 2016).

A number of approaches exist to estimate CO_2 exchanges in cities, including bottom-up methods using emission factors, indirect calculations through CO_2 concentrations (Velasco et al., 2013; Gately et al., 2013, 2015; Gurney et al., 2019), and CO_2 inverse modeling (Hutyra et al., 2014; Lauvaux et al., 2016). Indirect methods such as these are often associated with large uncertainties and a lack of spatial and temporal detail

(Velasco and Roth, 2010). As an alternative applied in this study, the eddy covariance (EC) method (Baldocchi et al., 2001) can be used to measure CO_2 fluxes (*FC*) in urban areas (Grimmond et al., 2002; Velasco and Roth, 2010; Bergeron and Strachan, 2011; Järvi et al.., 2012; Lui et al., 2012; Velasco et al., 2013; Ueyama and Ando, 2016; Song et al., 2017). However, urban EC observations have been generally limited, as compared to those efforts in natural ecosystems, with most studies undertaken in very dense urban settings or in open low-density areas of northern latitudes (Grimmond et al., 2004; Moriwaki and Kanda, 2004; Velasco and Roth, 2010; Kotthaus and Grimmond, 2012; Song and Wang, 2012; Ng et al., 2015; Schmutz et al., 2016; Roth et al., 2016). Furthermore, arid cities have been generally underrepresented in the use of the EC method (Song et al., 2017; Ramamurty and Pardyjak, 2011). This paucity of studies is related to the challenging nature of urban *FC* observations due to deployment logistics, security concerns, and the potential disruption of activities (Kotthaus and Grimmond, 2012; Grimmond, 2006). As the number of EC studies in urban areas grows, however, it will be possible to assemble inventories of CO_2 flux measurements that can be compared to bottom-up approaches.

Limitations in urban EC studies also imply that few efforts have been carried out to quantify the role of land cover type on *FC* measurements, for instance between urban parks and the high-density urban core. Relevant measurements represent a challenge due the spatial variability of urban land covers and the complex morphology of urban environments (Lui et al., 2012; Song et al., 2017; Lauvaux et al., 2016). Several studies have measured CO_2 exchanges in urban areas relative their surrounding environments. For example, Bergeron and Strachan (2011) compared agricultural, suburban, and urban

sites near Montreal, Canada. Ward et al. (2015) similarly studied three areas (woodland, suburban, and urban sites) in England, while Buckley et al. (2016) compared *FC* measurements in suburban and urban sites in Syracuse, USA. Ueyama and Ando (2016) is one of the few studies to perform a direct comparison of multiple urban patches in Japan. In Indianapolis, as part of the INFLUX experiment, an important effort to measure *FC* over several urban landscapes was also carried out (Davis et al., 2017; Richardson et al., 2017). However, arid cities are under-represented in terms of *FC* measurements with the EC method, though Song et al. (2017) analyzed conditions in Phoenix, USA.

In this study, we use a mobile EC tower to measure *FC* and meteorological conditions in three urban settings at Arizona State University (ASU) as described by Templeton et al. (2018) and similar to Soegaard and Møller-Jensen (2003). These short-term deployments are compared to a stationary (reference) EC tower in a suburban neighborhood and spanning the entire period (1 January to 30 September 2015). The three mobile sites represent different land cover types: a xeric landscaping, a parking lot, and a mesic landscaping. These sites are expected to vary in terms of their CO_2 exchanges due to variations in the amount of vegetation and anthropogenic emissions. Thus, the objectives of this study are to: (1) quantify and compare *FC* over different urban land cover types in relation to a location that provided reference meteorological conditions during the study period, (2) relate the observed differences to measures of anthropogenic emissions, plant photosynthetic activity, and meteorological forcing, and (3) determine the role of precipitation events and outdoor water use on modifying CO_2 exchanges across the sites.

Materials and Methods

Site descriptions

The study was carried out in four locations in the Phoenix Metropolitan Area (PMA) as described in Table 2.1 that were non overlapping and at most 42.8 km apart. The PMA has a population of 4.1 million (US Census Bureau, 2010) and is located in a hot, arid climate (Köppen classification BWh), with seasonal average temperatures of 14.1 ºC, 22.9 ºC, 33.9 ºC, and 24.8 °C, in the winter, spring, summer, and fall. A bimodal precipitation regime is present with winter frontal storms and summer thunderstorms during the North American monsoon (Adams and Conrie, 1997; Vivoni et al., 2008). Mean annual precipitation is 204 mm yr^{-1} based on 1981 to 2010 data, with winter (December to January) and summer (July to September) amounts of 68.3 mm and 67.8 mm, respectively. Spring and early summer (March through June) are typically dry, accounting for only 17% of the mean annual precipitation (Chow et al., 2014a; Templeton et al., 2018). The low annual precipitation leads to water limited conditions in natural ecosystems (Vivoni et al., 2008), requiring outdoor water use to support vegetation in urban areas (Chow et al., 2014a; Volo et al., 2014, 2015).

The three mobile deployments and the reference site represent different urban land covers in the PMA. Figure 2.1 presents an aerial image of each sampling location that depicts differences in urban characteristics. These urban land covers correspond to: (a) xeric landscaping (XL) site, classified as a Local Climate Zone (LCZ) 5 (Stewart and Oke, 2012) composed of drip-irrigated trees (palo verde, *Parkinsonia florida*) of 3-4 m of height, with gravel and bare soil cover, located within a setting that included a midrise

Table 2.1: General characteristics of the four study sites and sampling periods.

Site	Land Cover	Latitude	Longitude	Elevation (m)	Start Day and Time	End Day and Time	Total Days
XL	Xeric Landscaping	33.4198°	-111.9272°	354	1/20/2015 12:00	3/13/2015 8:30	53
PL	Pavement	33.4212°	-111.9387°	356	5/19/2015 15:00	6/30/2015 6:00	43
ML	Mesic Landscaping	33.3116°	-111.6806°	411	7/9/2015 13:00	9/18/2015 8:30	72
REF	Residential	33.4838°	-112.1426°	337	1/1/2015 0:00	10/13/2015 23:30	286

(three-story) building used for office space and a paved road; (b) a parking lot (PL) site, classified as a LCZ 8 (Stewart and Oke, 2012), characterized by pavement (asphalt) with minimal vegetation, near an intersection with high traffic and frequently contained vehicles, with a low number of 6 m palm trees and large low-rise (one- to three-story) buildings used for office space surrounded by impervious cover nearby; (c) a mesic landscaping (ML), classified as LCZ 9 (Stewart and Oke, 2012), consisting of a sprinkler-irrigated turf grass (approximately 2–3 days per week, 3 times per day, for 20 to 30 min each time) among sparsely built single-family homes (low-rise, one story) with sparse, undeveloped land cover nearby including sparse 6 m trees; and (d) a suburban residential area, classified as LCZ 6 (Stewart and Oke, 2012), consisting of medium-density single-family homes, streets, and open spaces, used as a reference site (REF). As compared to ML, the REF site has lower irrigation due to larger variations in landscaping with some yards having trees and grasses, but most containing gravel and bare soil. One of the sites (PL) is nearly devoid of vegetation, while one site (ML) has light traffic. The REF site is a stationary EC system in operation during the entire sampling period and spanning the seasonal changes in meteorological conditions to allow quantitative comparisons with the short-term deployments. All mobile deployments were within ASU (Tempe campus for XL and PL and Polytechnic campus for ML) and authorized through the ASU Facilities Department.

A land cover classification was performed for the three mobile deployments using color (0.30 m) orthoimagery from the U.S. Geological Survey (http://lta.cr.usgs.gov/high_res_ortho). A supervised classification based on RGB signatures was done using a maximum likelihood method and classifying the urban land

cover as (1) trees, (2) grass, (3) undeveloped (gravel or bare soil), (4) pavement (asphalt), and (5) buildings or concrete. Percentages of each land cover type within a unique EC footprint were derived from aggregations of 30-min interval daytime footprint estimates. The EC footprint was obtained using the analytical model of Kormann and Meixner (2001) for an area of 500 m by 500 m centered at each site and a horizontal pixel resolution of 5 m selected to be less than the measurement height (Van de Boer et al., 2013). Following Anderson and Vivoni (2016), the EC footprint (Schmid, 1994) was calculated for each 30 min interval of turbulent daytime conditions, averaged over each daytime period and aggregated to derive a unique footprint for each deployment. The proportion of land cover in the 80% cumulative source area around each deployment can be seen in Table 2.2. Chow et al. (2014a) determined the land cover at the REF site based on a 2.4 m resolution Quickbird image for a circular region of 1 km^2 around the location.

At the XL site, the 80% cumulative footprint is influenced mainly (Figure 2.1c) by the 3-4 m trees around the tower, with some contributions from a street to the east, a public transportation center to the north, and a minimum impact of a three-story building to the west. The PL footprint is influenced primarily by the parking surface and two nearby streets to the north and west, with limited influence from surrounding buildings. At the ML site, the irrigated turf grass around the tower is the main contributor and to a lesser extent there is an influence of sparse trees and one-story houses. The highest vegetation cover is present at ML (44.3%), while the lowest occurs at PL (6.6%). A large contrast is also present in the areal coverage of urban surfaces (buildings, concrete, and pavement), with the highest cover at PL (79.5%) and the lowest at ML (21.1%).

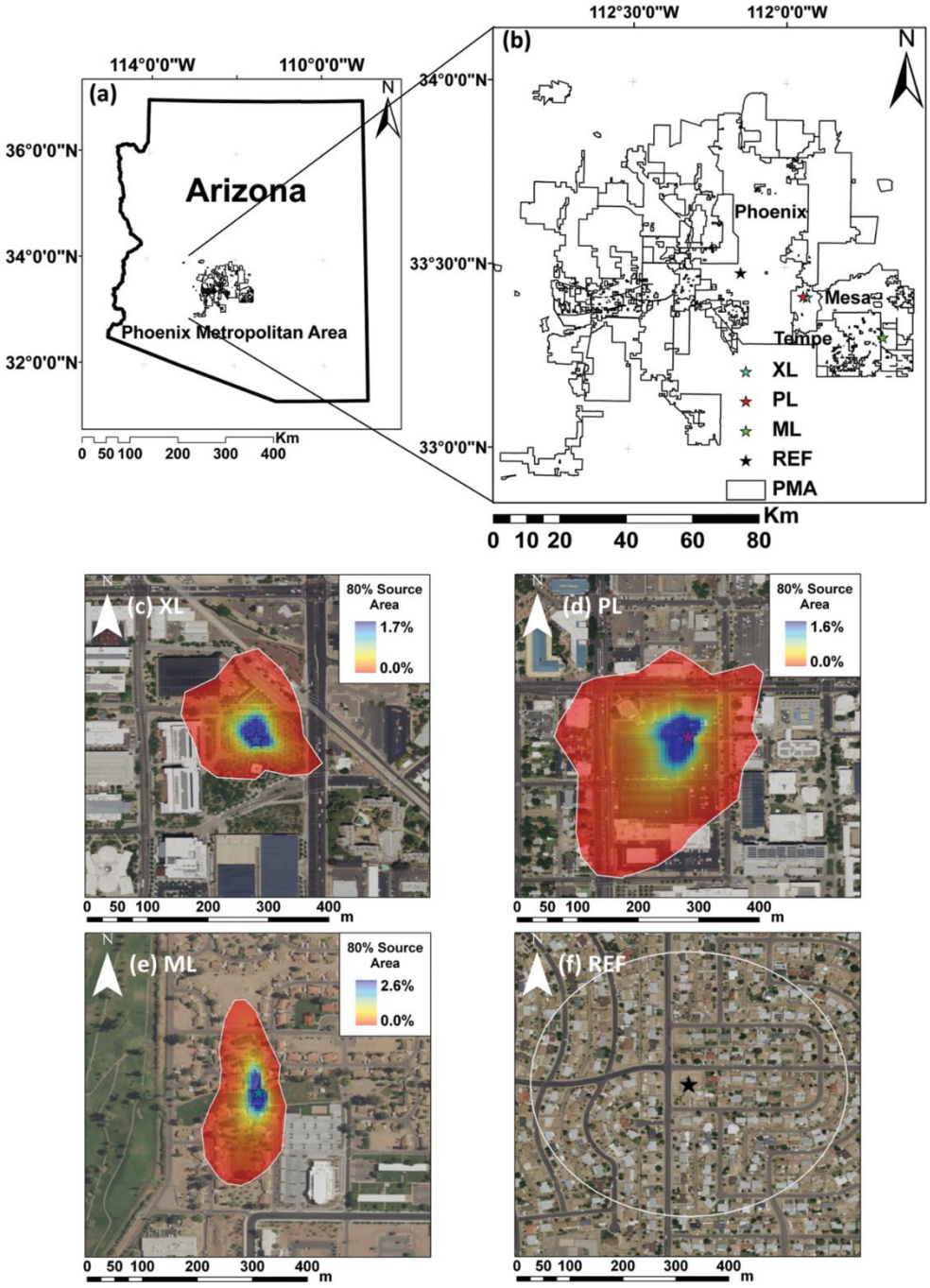

Figure 2.1: Location of the study sites. (a) Location of the Phoenix Metropolitan Area, and (b) the four study sites: (c) xeric landscaping (XL) site at ASU Tempe campus; (d) parking lot (PL) site near a high traffic intersection at ASU Tempe campus; (e) mesic landscaping (ML) site near residential housing at ASU Polytechnic campus; and (f) suburban (REF) site in Phoenix. Contour polygon and color gradient represent the 80% cumulative source area for each site. Aerial images of the sites correspond to National Agricultural Imagery Program (NAIP) from the U.S. Geological Survey (https://doi.org/10.5066/F7QN651G).

Table 2.2: Urban land cover percentages for each site, with REF reported by *Chow* et al. (2014a).

Urban Land Cover	80% Cumulative Source Area			
	XL	**PL**	**ML**	**REF**
Trees	38.2 %	5.9 %	16.2 %	4.6 %
Grass	0.4 %	0.7 %	28.1 %	10.0 %
Undeveloped	29.7 %	13.9 %	34.6 %	36.8 %
Pavement	8.3 %	57.4 %	12.8 %	22.0 %
Buildings or concrete	23.4 %	22.1 %	8.3 %	26.4 %

Eddy covariance measurements and data processing

The mobile EC platform consisted of a telescoping tower that extends to a maximum height of 15 m. High frequency measurements of *FC*, sensible heat (*H*), and latent heat *(λET*) fluxes were made using an infrared gas analyzer (LI-7500, Li-Cor Biosciences) to measure H_2O and CO_2 concentrations, and a three-dimensional sonic anemometer (CSAT3, Campbell Scientific) to measure wind velocities (Templeton et al., 2018). Sensors were aligned to the dominant wind direction for each deployment, which were determined as 21º at XL, 227º at PL, 230º at ML, and 259º at REF. EC measurements were carried out at a height of 7.0 (XL), 9.0 (PL), and 8.0 m (ML) to ensure that turbulent fluxes were observed above the urban roughness sublayer. In almost all the cases, the EC measurements were above the surrounding roughness elements within the footprint (Richardson et al., 2017). The average urban canopy layer height (z_h) was 3.5, 2.8, and 5 m for the XL, PL, and ML sites, respectively, leading to estimated blending heights ($1.5z_h$) from Grimmond et al. (2004) which were smaller than measurement heights. Thus, we assume that the mobile measurements sampled a blended, spatially-averaged signal considered as representative of the urban land cover within the small footprint (Feigenwinter et al., 2012). As a result, the application of Monin-Obukhov Similarity

Theory and the concept of stability are valid (Foken, 2006). The REF site had a taller height of 22.1 m, measuring turbulent fluxes from a broader and more heterogeneous residential area (Chow et al., 2014a).

Data was collected at 10 (PL, ML, and REF) and 20 Hz (XL) and processed at 30-minute intervals using EdiRe (Clement, 1999). EC processing included corrections for stability and density fluctuations (Webb et al., 1980; Foken, 2006), coordinate rotation (Wilczak and Oncley, 2001), removal of signal lags in gas concentrations due to the separation between the sensors (Massman, 2001), frequency response corrections (Moore, 1986), and estimates of sensible heat using the sonic temperature corrected with humidity following standard procedures (Paw et al.,2000). Measurements were also filtered to exclude periods when precipitation was > 0.2 mm per 30 min, when winds were from the opposite direction at which instruments were mounted, when fluxes were further than 3 standard deviations from the mean, when the friction velocity criterion of $u^* < 0.15$ m s^{-1} was met, and for absolute values of FC greater than 2 mg m^{-2} s^{-1}, according to the behavior of the 30-min values and to Schmid et al. (2000). Missing data due to data filtering and sensor malfunction accounted for 54.1%, 29.9%, 50.2% and 37.2% of the total half-hourly data obtained during the deployments at the XL, PL, ML, and REF sites, respectively. Most of the missing data corresponded to night-time measurements (80.5%, 70.2%, 59.6% and 74.3% at XL, PL, ML, and REF). Gap-filling procedures were not used to avoid the impacts that these methods might have on comparisons of daily values. Additional measurements at all sites included net radiation (R_n) using a four-component net radiometer (CNR4, Vaisala), air temperature (T_a), and

relative humidity (*RH*) using a HMP155A probe (Vaisala), and precipitation (*P*) using a tipping-bucket rain gauge (TE525MM, Texas Electronics).

Urban carbon dioxide budget and meteorological conditions

The urban CO_2 budget varies from natural ecosystems due to anthropogenic sources. Urban *FC* is composed of sources, sinks, and storage changes (Crawford et al., 2011; Feigenwinter et al., 2012; Grimmond and Christen, 2012) as:

$$FC = F_F + F_R - F_P + \Delta S_C \,, \tag{2.1}$$

where F_F is the CO_2 emitted from fuel combustion; F_R is the release of CO_2 due to respiration by animals, humans, and vegetation; F_P is the CO_2 assimilated by the photosynthesis of vegetation; and ΔS_C is the net changes of CO_2 storage, generally considered to be small or negligible during fully turbulent conditions (Bjorkegren et al., 2015). Consideration of the storage changes in the urban CO_2 budget is relatively rare (Crawford and Christen, 2014; Bjorkegren et al., 2015). Typically, *FC* is reported in grams (g) or milligrams (mg) of CO_2 per unit area per unit time, while carbon dioxide concentrations ($[CO_2]$) in the atmosphere are reported in parts per million (ppm). In practice, *FC* measurements in urban areas using the EC method are not able to identify the various origins of the CO_2 fluxes. Nevertheless, a $FC < 0$ indicates that plant uptake is larger than respiration and anthropogenic emissions ($F_P > F_F + F_R$, or a net carbon dioxide sink), while a positive *FC* suggests a net carbon dioxide source ($F_F + F_R > F_P$). Neutral flux conditions ($FC \cong 0$) occur when sources and sinks are balanced ($F_F + F_R = F_P$).

FC and the associated meteorological conditions for each sampling period at each site were analyzed at various time scales: (1) daily averages, (2) average diurnal cycles at 30-

min resolution, and (3) total amounts during the sampling period. From the large set of measurements, we focus on *P*, T_a, *RH*, and incoming solar radiation (R_s). For the EC systems, R_n is obtained from measurements of the net shortwave (R_s^{net}) and net longwave (R_l^{net}) radiation as:

$$R_n = R_s^{net} + R_l^{net} = (1 - a)R_s + R_l^{net} \,, \tag{2.2}$$

where *a* is the albedo, with all radiation fluxes measured in W m^{-2}. As described in Templeton et al. (2018), the surface energy balance for a simple plane facet in an urban area, under the assumptions of negligible anthropogenic heat, advection and energy storage, can be described as:

$$R_n - G = H + \lambda ET \,, \tag{2.3}$$

where *G* is the ground heat flux, *H* is the sensible heat flux, and λET is the latent heat flux, all in W m^{-2}. Evapotranspiration (*ET* in mm day^{-1}), obtained using the latent heat of vaporization (λ), is analyzed at daily and diurnal time scales. Furthermore, we estimated the evaporative fraction (*EF*) as a daily average and for the daytime period (at 30-min resolution) as:

$$EF = \frac{\lambda ET}{H + \lambda ET} \quad , \tag{2.4}$$

to provide insight into the relation between *FC* and the turbulent fluxes. Additional analyses were performed for subsets of days classified as ‘wet’ or ‘dry’ based on the occurrence of precipitation (P > 0.2 mm day^{-1}) on the day of an event and the two subsequent days.

Analyses of controlling factors with ancillary data

We related the *FC* measurements to anthropogenic and biogenic processes that lead to sources and sinks of CO_2 in urban environments. According to Koerner and Klopatek

(2002), around 80% of the total CO_2 contribution in the PMA is due to vehicular traffic. As such, we analyzed *FC* separately for weekdays (Monday to Friday) and weekends (Saturday and Sunday) and related these to vehicular traffic counts for nearby streets to the deployments as well as to the areal fraction of pavement classified for each site. Traffic counts (total of vehicles, 2-way hourly resolution data) were obtained through the Traffic Counts Database System of the Maricopa Association of Governments (http://mag.ms2soft.com/tcds/tsearch.asp?loc=Magandmod=). Since traffic counts data was limited, we obtained the available information for dates close to the sampling periods (3/18/2015 to 3/24/2015 for XL, 2/25/2015 and 2/26/2015 for PL, 2/18/2015 to 2/24/2018, and 3/4/2015, 3/5/2015, 3/24/2015 and 3/25/2015 for REF) and for streets near to the deployments. While biogenic factors in urban environments include both vegetation and soil activity, plants are the only known sink of CO_2 that can oppose anthropogenic emissions (Liu et al., 2012). Thus, we analyzed the effect of vegetation activity through the fraction of trees and grasses at each site as well as the Normalized Difference Vegetation Index (*NDVI*) obtained from the Moderate Resolution Imaging Spectroradiometer (MODIS) product MOD09GQ MODIS/Terra Surface Reflectance Daily L2G Global 250m SIN GRID (Vermote and Wolfe, 2015). Data obtained corresponded to the 250 m pixel at each site for each sampling period. The complete dataset included *NDVI* images from January 1 to October 13, 2015, with cloud-free scenes (190 out of 286). However, the coarse resolution of MODIS presents a scale discrepancy to the source areas around each tower. To compensate for this, *NDVI* from the higher resolution Landsat 8 OTI product was used to bias-correct the MODIS data through a linear regression over each site. A comparison of *FC* was also conducted

separately for sunny and cloudy days using a threshold of measured R_s (75% of the seasonal daily average). To determine if the *FC* observations were different between selected days (i.e., weekday versus weekend or sunny versus cloudy), a Mann-Whitney U Statistic rank sum test was performed, with significance determined for $p \leq 0.05$. A similar procedure was conducted to quantify the effect of wet versus dry conditions on the *FC*, [CO_2], and *EF* observations. Pearson correlation coefficients (CC) were also used to test the linear correlation ($-1 \leq CC \leq 1$) between measured variables, among different sites and with controlling factors such as *NDVI*, with significance determined for $p \leq 0.05$. For all statistical analyses, only daytime data were used to focus on time periods when the controlling factors affect the measured fluxes.

Results and discussion

Seasonal variations in meteorological and CO_2 conditions

Daily values of precipitation (total in mm), incoming solar radiation (average in W m^{-2}), air temperature (average in ºC) and relative humidity (average in %) are shown in Figure 2.2 for the three deployments and the REF site. Temporal variations in meteorological variables reflect the seasonal progression from winter to summer and the influence of individual precipitation events occurring across all seasons. To complement this comparison, Table 2.3 presents differences in *P* and T_a between the mobile deployments and reference site during simultaneous periods. Note that the sampling periods were generally drier and warmer than corresponding long-term (1981-2010) averages (Templeton et al., 2018). Overall, the XL site had similar meteorological conditions as the REF site during the same period with a small difference in R_s (average of -6.57 W m^{-2} lower at XL), due to the higher *P* during the winter-spring period.

Similarly, the PL site had lower values of R_s (-11.64 W m^{-2}), but higher T_a (+1.90 °C) and similar *RH*, as compared to the REF site at the daily scale. At the ML site, a lower R_s (-12.98 W m^{-2}) and T_a (-1.83 °C) were measured, with an increased amount of *RH* (+15.83 %) due to the frequent irrigation of the turf grass. Noted small differences in meteorological conditions are due to a number of factors: (1) small variations in the sensor types and deployment heights (Chow et al., 2014a; Templeton et al., 2018), (2) daily differences in precipitation and cloud cover at sites which were at most 42.8 km apart (Figure 2.1), and (3) the effects of land cover on surface properties, including albedo, soil temperature and soil moisture, that influence meteorological states through the surface energy balance, as discussed in Templeton et al. (2018).

Figure 2.3 presents the seasonal variation of daily values of *FC* (total in g CO_2 m^{-2} day^{-1}) and [CO_2] (average in ppm) for the three mobile deployments in comparison to the REF site. Daily averages of net radiation (R_n) are shown to distinguish seasonality. Clear differences are noted in the magnitude and behavior of *FC* and [CO_2] between the sites, as quantified in Table 2.3. XL, PL, and REF acted as net sources of carbon dioxide during the sampling period, while ML was a carbon dioxide sink. All mobile sites had higher [CO_2] than the REF site, while a larger (smaller) *FC* was noted at XL and PL (at ML) when compared to REF. Lower values of [CO_2] were measured at the REF site due to a much higher sampling height than the mobile deployments since [CO_2] decreases with altitude. As expected, [CO_2] decreases from winter to summer in response to seasonal variations in northern hemisphere vegetation activity (Keeling et al., 1996).

Table 2.3: Total *FC*, average [CO_2], precipitation and air temperature during each deployment and for the simultaneous period at the REF site (labeled as Ref.).

Site	*FC* (g CO_2 m^{-2})	Ref. *FC* (g CO_2 m^{-2})	[CO_2] (ppm)	Ref. [CO_2] (ppm)	*P* (Ref. *P*) (mm)	T_a (Ref. T_a) (°C)
XL	723.31	561.54	419.89	379.44	43.0 (27.7)	17.3 (17.8)
PL	862.40	406.13	408.05	358.95	15.2 (8.6)	32.9 (31.6)
ML	-166.30	769.26	380.24	353.49	5.4 (13.7)	33.1 (33.5)
REF	3021.56	3021.56	364.84	364.84	99.6 (99.6)	26.5 (26.5)

Except for the early part of the year, the REF site exhibits a fairly constant *FC* during the period (average of 10.56 g CO_2 m^{-2} day^{-1}) and a narrow range of fluctuations (standard deviation of 4.82 g CO_2 m^{-2} day^{-1}). This is within the ranges of values (in g CO_2 m^{-2} day^{-1}) for other open low-rise sites, for instance, in Melbourne, Australia from 8.49 to 33.4 (Coutts et al., 2007) and in Syracuse, USA with 11.23 (Buckley et al., 2016). In contrast, the XL site had wide variations in daily *FC* (std. of 11.39 g CO_2 m^{-2} day^{-1}) with magnitudes (ave. of 13.64 g CO_2 m^{-2} day^{-1}) that were generally higher than at REF as well as higher [CO_2] (+44.25 ppm). This value is similar to an open mid-rise site measured in Sakai, Japan with 12.8 (Ueyama and Ando, 2016), but lower than year-round values reported in Tokyo, Japan (Moriwaki and Kanda, 2004), México City (Velasco et al., 2005), and Essen, Germany (Kordowski and Kuttler, 2010), at 43, 35.4 and 35.4 g CO_2 m^{-2} day^{-1}. Daily fluctuations at XL correspond to changes in vehicular traffic and plant phenology.

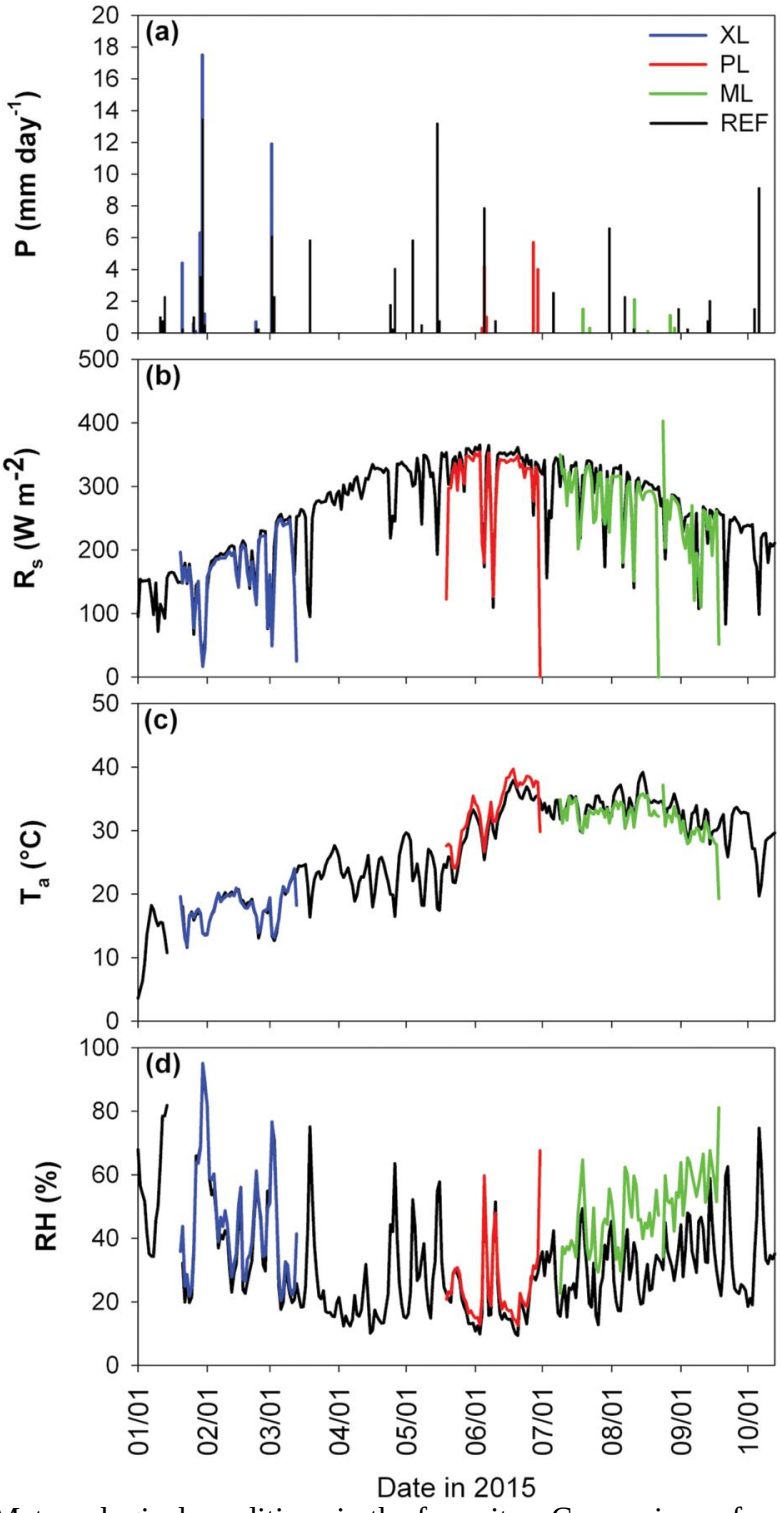

Figure 2.2: Meteorological conditions in the four sites. Comparison of meteorological measurements during entire study period (1 January to 30 September, 2015) including: (a) precipitation, (b) incoming solar radiation, (c) air temperature, and (d) relative humidity, shown as daily averages (R_s, T_a, and RH) or totals (P).

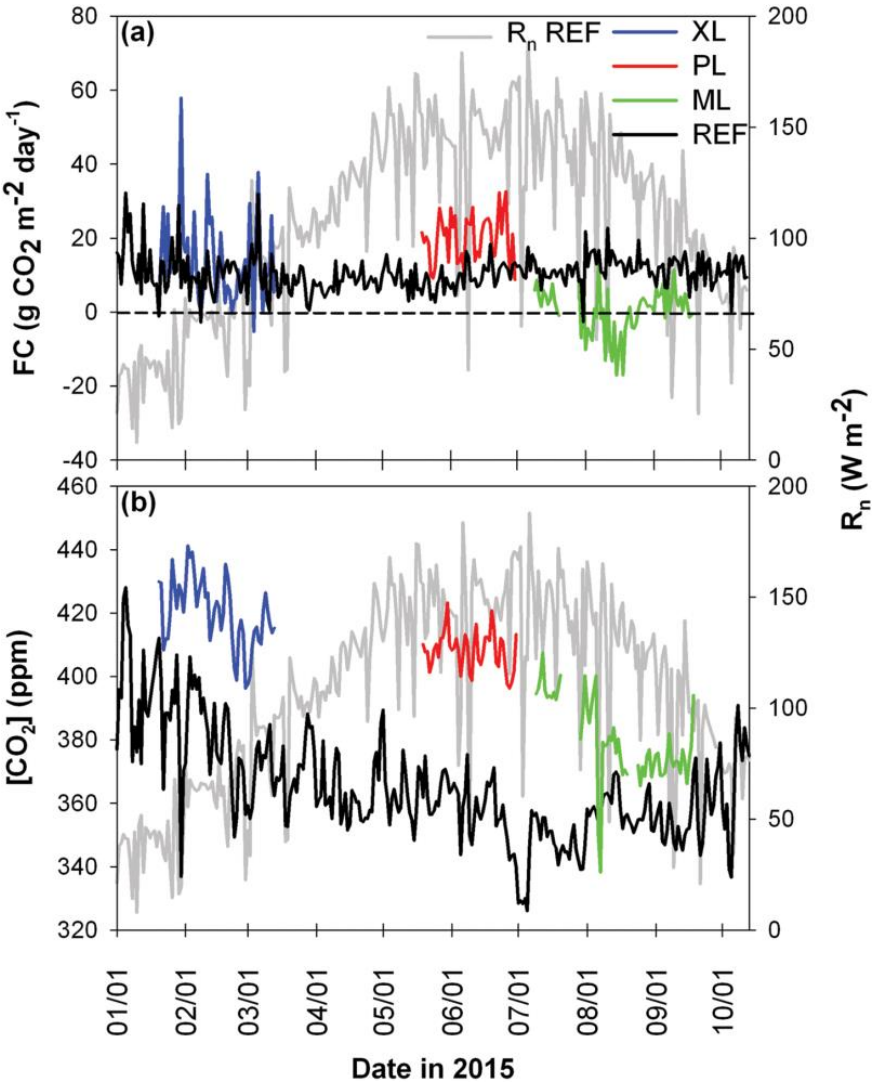

Figure 2.3: Daily values of *FC* for each site. Daily total values of *FC* (a) and average values of CO_2 concentration (b) for the XL, PL, ML, and REF sites over the study period, with daily average values of net radiation (R_n) at REF shown as a reference.

The PL site had consistently higher *FC* values as compared to the REF site (ave. 20.05 g CO_2 m^{-2} day^{-1}), with larger daily variations (std. 6.39 g CO_2 m^{-2} day^{-1}) and higher $[CO_2]$ (+49.38 ppm). The only previous study with a large low-rise structure was found in Houston, USA (Park and Schade, 2016), which reported a higher daily value (29.38 g CO_2 m^{-2} day^{-1}) during the summer, however, other highly urbanized sites including compact low-rise (Velasco et al., 2013, 2016; Buckley et al., 2016; Roth et al., 2016),

compact mid-rise (Soegaard and Møller-Jensen, 2003; Moriwaki and Kanda, 2004; Kordowski and Kuttler, 2010; Pawlak et al., 2011; Liu et al., 2012; Lietzke and Vogt, 2013; Lietzke et al., 2015; Schmutz et al., 2016; Stagakis et al., 2019) and compact high-rise (Song and Wang, 2012), reported values between 18.7 and 71.7 g CO_2 m^{-2} day^{-1} during the summer. The Pearson correlation coefficient (CC) of *FC* between XL and PL and REF was significant (CC = 0.31 and 0.37, respectively), whereas ML had a much lower, insignificant correlation (CC = -0.15), suggesting a stronger similarity in the factors affecting *FC* at these two sites (see Table 2.4 for a comparison of CC for other variables between the mobile deployments and REF site). A distinct behavior is noted at the ML site, where a more negative *FC* (ave. -2.77 g CO_2 m^{-2} day^{-1}) is observed as compared to the REF site, with similar daily variations (std. 7.65 g CO_2 m^{-2} day^{-1}), while a slightly higher [CO_2] (+25.91 ppm) is due to the lower sampling heights. Gradual variations during the summer could correspond to vegetation uptake, with a minimum value of ≈ -17 g CO_2 m^{-2} day^{-1} in August and positive values at the end of the sampling period. Sparsely built sites in other cities had also daily values close to zero showing that vegetation can neutralize CO_2 emissions for a particular season, for instance, during the summer in Copenhagen, Denmark (Soegaard and Møller-Jensen, 2003), Saint Paul, USA (Peters and McFadden, 2012), and Montreal, Canada (Bergeron and Strachan, 2011). Other highly vegetated urban sites showed CO_2 uptake values during the summer, for example in Baltimore, USA (Crawford and Christen, 2014) and in Nagoya, Japan (Awal et al., 2010).

Table 2.4. Pearson correlation coefficient (CC) of daily values of precipitation, air temperature, net radiation, latent heat flux, evaporative fraction, carbon dioxide flux, and carbon dioxide concentration between mobile locations and REF site for simultaneous periods. Bolded numbers indicate significant correlations at $p \leq 0.05$.

Site	P	T_a	R_n	λET	EF	FC	$[CO_2]$
XL	**0.95**	**0.95**	**0.88**	**0.62**	**0.84**	**0.31**	**0.69**
PL	**0.48**	**0.96**	**0.84**	**0.48**	**0.38**	**0.37**	**0.69**
ML	-0.02	**0.76**	**0.68**	**0.34**	0.14	-0.15	-0.08

Diurnal variations in surface energy, water and CO_2 conditions

Diurnal variations of carbon dioxide flux and latent heat flux are compared in Figure 2.4, where symbols indicate average values at 30-min resolution and error bars capture ±1 standard deviation during each deployment period (i.e., for differing seasons). For comparison, thin lines show corresponding values at the REF site for the same periods as the deployments at XL, PL, and ML. Clear variations are noted in *FC* and *λET* among the sites. For instance, latent heat flux, which can be a proxy for irrigated vegetation activity due to its dependence on well-watered plant transpiration (Williams and Torn, 2015), varies considerably (Templeton et al., 2018), with average daily peaks of 67.82 W m^{-2} (XL), 59.54 W m^{-2} (PL), 263.96 W m^{-2} (ML), and 92.48 W m^{-2} (REF). The largest diurnal peaks of *λET* correspond to ML (Figure 2.4c) that is composed of the highest fraction of irrigated vegetation (44.3%) and exhibits the most negative values of *FC* near mid-day (-0.32 mg CO_2 m^{-2} s^{-1}). The diurnal behavior of *FC* and *λET* at ML is similar to observations in natural ecosystems during well-watered conditions or neighborhoods with abundant vegetation (Scott et al., 2004; Pataki et al., 2006; Awal et al., 2010; Perez-Ruiz et al., 2010; Bergeron and Strachan, 2011; Crawford et al., 2011; Peters and McFadden, 2012; Ward et al., 2015; Buckley et al., 2016; Ueyama and Ando, 2016; Velasco et al., 2016). Furthermore, the difference in time between the diurnal minimum in *FC* and the maximum in *λET* is short, about 0.5 hours on average, showing a coupling between *FC*

and λET that is typical of natural ecosystems where maximum photosynthesis occurs near mid-day.

In contrast, the PL site (Figure 2.4b) has a reduced amount of λET with the least variation during the day due to its low fraction of vegetation (6.6%), resulting in a positive *FC* during the day, with a peak of +0.48 mg CO_2 m^{-2} s^{-1} at 5:00 p.m. coinciding with rush hour traffic in the nearby street. This leads to a decoupling of the peaks in *FC* and λET, which are separated by 4 hours at PL. Peaks of *FC* during rush hours are typical of highly urbanized areas, with reported values between 0.35 to 1.67 mg CO_2 m^{-2} s^{-1} in compact low-rise and mid-rise areas during the summer (Pawlak et al., 2011; Liu et al., 2012; Buckley et al., 2016; Helfter et al., 2016; Ueyama and Ando, 2016; Järvi et al., 2019) and about 0.62 mg CO_2 m^{-2} s^{-1} in a compact high-rise during the summer (Song and Wang, 2012). Interestingly, the diurnal cycles at XL and REF (Figures 2.4a and 2.4d) exhibit behaviors that are a mixture of the effects of vegetation and traffic activity. Positive peaks in *FC* occur around rush hour times of 8:00 a.m. and 6:00 p.m. (0.35 and 0.26 mg CO_2 m^{-2} s^{-1} at XL; 0.16 and 0.21 mg CO_2 m^{-2} s^{-1} at REF, respectively), while a mid-day minimum in *FC* is noticeable (0.05 and 0.02 mg CO_2 m^{-2} s^{-1} at XL and REF, respectively). The decreases in *FC* coincide with vegetation activity due to the small differences in time with λET (±1.5 hours), but are insufficient to counteract CO_2 emissions, such that *FC* remains positive at XL and REF on average during the course of a day. This behavior has been reported in several open low- and mid-rise urban landscapes, with summer values fluctuating from 0.13 to 1.32 mg CO_2 m^{-2} s^{-1} during rush hours and mid-day values from ~0 to 0.44 mg CO_2 m^{-2} s^{-1} (Grimmond et al., 2004; Moriwaki and Kanda, 2004; Velasco et al., 2005; Coutts et al., 2007; Kordowski and

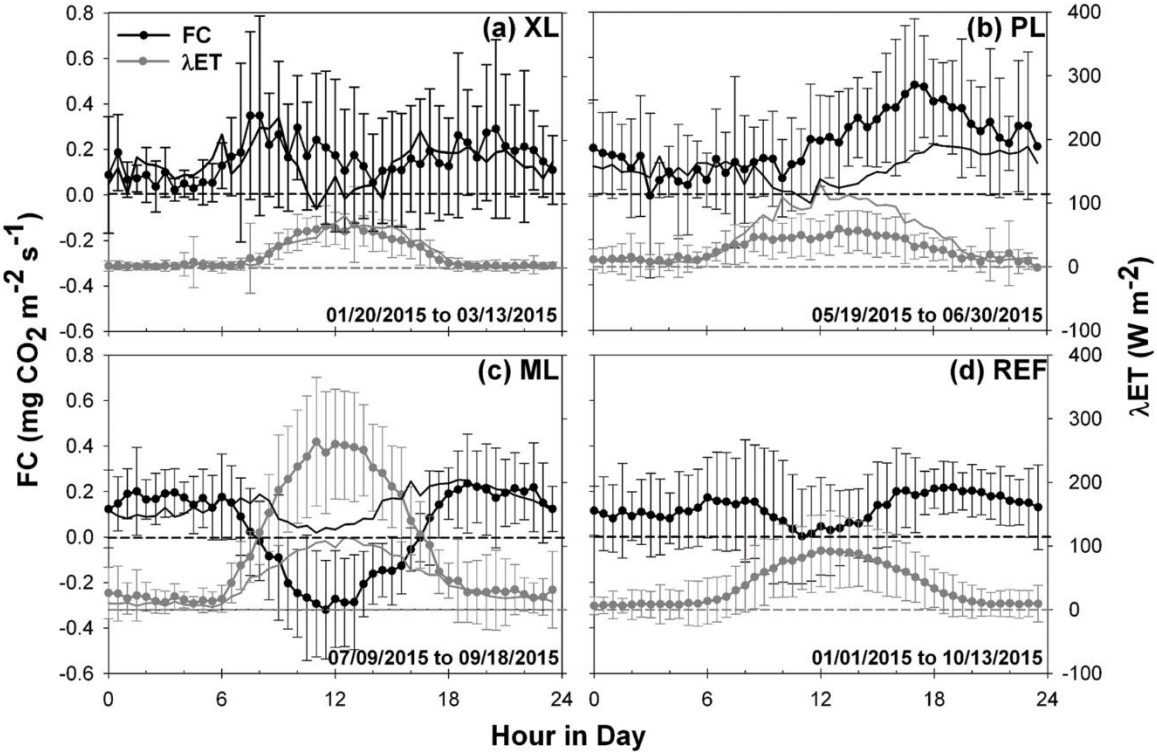

Figure 2.4: Diurnal averages of *FC* and *λET* at the four sites. Average diurnal cycle of carbon dioxide flux and latent heat flux for (a) XL, (b) PL, (c) ML, and (d) REF sites. Error bars represent one standard deviation over the indicated periods. Thin lines are average diurnal cycles at the REF site during the same period as the mobile deployment for *FC* (black) and *λET* (gray). Horizontal lines indicate zero values. Different sampling periods are specified in each plot.

Kuttler, 2010; Buckley et al., 2016; Ueyama and Ando, 2016; Weissert et al., 2016; Song et al., 2017; Järvi et al., 2019).

To complement this analysis, Figure 2.5 presents the diurnal cycles of CO_2 concentration and daytime evaporative fraction during each deployment period. Given the stronger variation in [CO_2] from winter to summer relative to *FC* (Figure 2.3), it is useful to directly compare the mobile deployments to the simultaneous behavior at the REF site (thin lines). Relatively small variations in [CO_2] occur throughout the day, with standard deviations of 9.45 ppm (XL), 17.11 ppm (PL), 8.46 ppm (ML), and 8.15 ppm (REF). Higher [CO_2] typically corresponds to morning traffic periods from 6:00 to 8:00

a.m. and in the evening from 6:00 to 10:00 p.m. when the diurnal accumulation of CO_2 and ceasing of plant uptake play a role as well as changes in the urban boundary layer height (Crawford et al., 2016). Relative to the REF site, PL has the highest [CO_2] and exhibits the strongest diurnal variations, in part due to its high fraction of urban surfaces dedicated to transportation (79.5%, Figure 2.1d) including the parking lot and nearby streets, particularly during the afternoon and night due to the nature of the surrounding businesses. During mid-day, pavements and buildings at PL have the lowest *EF* (0.18), an indication that surface energy fluxes are dominated by conduction from urban materials. In contrast, irrigated turf grass and trees at the ML site support a much higher mid-day *EF* (0.61), whose daytime variations match well with the observed decrease in [CO_2] in response to plant uptake. Notably, the higher overall magnitude of [CO_2] at ML relative to REF (Table 2.3) is likely due to differences in sampling height (8 m versus 22.1 m) as the decrease in [CO_2] with altitude is well known (Vogt et al., 2003, 2006). This is supported by the higher daytime *EF* at ML during a simultaneous period comparison with REF (thin line) which is consistent with more negative *FC* at the lower sampling height of ML (Figure 2.4c). In between these end-member cases, XL and REF exhibit diurnal behaviors with respect to [CO_2] and *EF* that are mixtures of plant uptake and vehicular emissions. Thus, to isolate the effects of these factors requires a more detailed view of site conditions, as described next. Additionally, [CO_2] dynamics are affected by diurnal changes in boundary layer conditions such as vertical mixing and advection (Lietzke and Vogt, 2013; Crawford et al., 2016), however, those factors are not analyzed here.

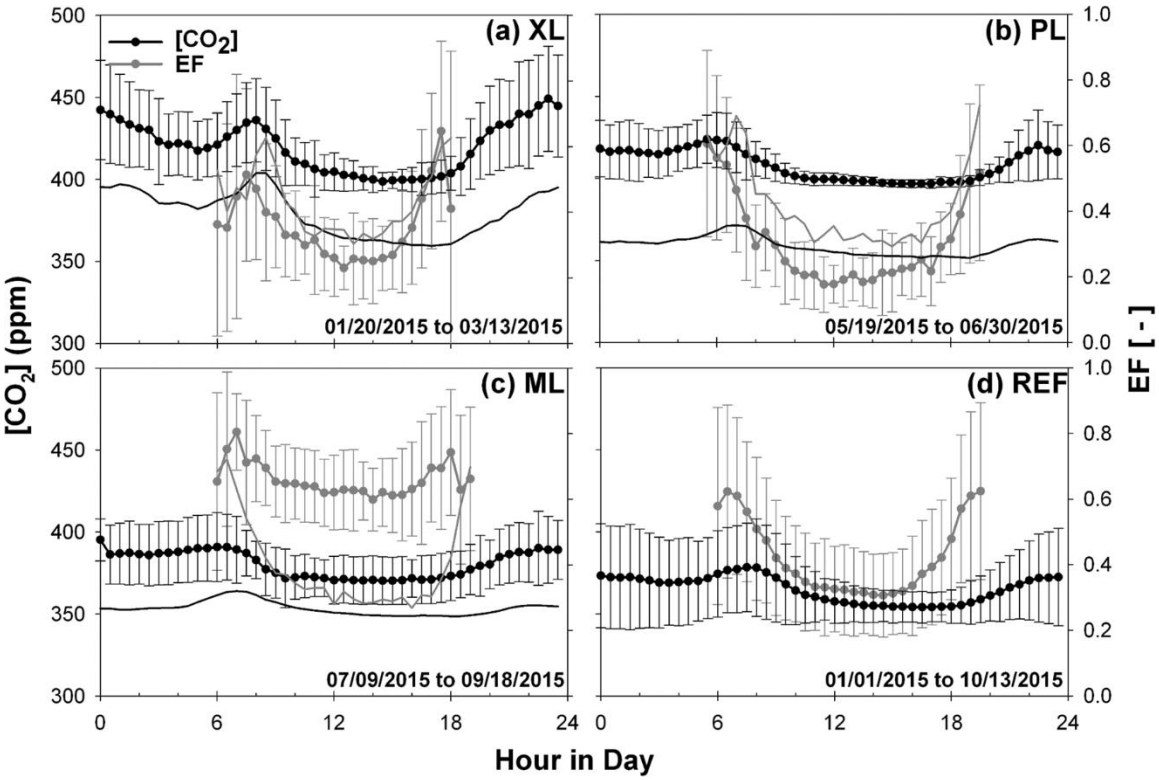

Figure 2.5: Diurnal averages of [CO_2] and *EF* for the four sites. Average diurnal cycle of CO_2 concentration and evaporative fraction for the (a) XL, (b) PL, (c) ML, and (d) REF sites. Error bars represent one standard deviation over the indicated periods. Thin lines are average diurnal cycles at the REF site during the same period as the mobile deployment for [CO_2] (black) and *EF* (gray). Different sampling periods are specified in each plot.

Controlling factors of CO_2 conditions

The effect of vehicular traffic is assessed in Figure 2.6 through comparisons of the average diurnal cycle of *FC* and [CO_2] for weekday and weekend days at each site. This is an approach that has been used in several studies to assess the impacts of traffic on *FC* (Velasco et al., 2005, 2013, 2016; Coutts et al., 2007; Bergeron and Strachan, 2011; Hiller et al., 2011; Pawlak et al., 2011; Hirano et al., 2015; Buckley et al., 2016; Weissert et al., 2016; Song et al., 2017; Stagakis et al., 2019). For reference, local traffic counts (number of vehicles per hour) are provided as diurnal cycles for available time periods. Differences in *FC* between weekday and weekend periods are noted for rush hour periods

(8:00 a.m. and 6:00 p.m.) at the XL, PL, and REF sites, coinciding with higher traffic counts. Similarly, [CO_2] exhibits higher values at these sites for weekdays when a higher traffic volume is expected, but typically only in the morning. Larger *FC* and [CO_2] differences at PL (ave. of 0.18 mg CO_2 m^{-2} s^{-1} and 3.57 ppm) between weekday and weekend days suggest that the CO_2 budget in the parking lot is controlled primarily by vehicular emissions in nearby streets. In addition, a progressive increase in *FC* is noted at PL during the daytime hours for all days, closely matching the rise in traffic. In contrast, all other sites are characterized by a mid-day decrease in *FC* and [CO_2], despite rising traffic counts at XL and REF, which is attributed to vegetation uptake counteracting the vehicular emissions for *FC* and an increase of the urban boundary layer height during the day for [CO_2] (Lietzke et al., 2015). Smaller differences in *FC* and [CO_2] at XL and REF (ave. of 0.03 and 0.01 mg CO_2 m^{-2} s^{-1} and 5.88 and 2.69 ppm, respectively) between weekday and weekend days, as well as the mid-day response to plant activity, suggest that these sites are influenced by both traffic and vegetation factors for the sampled season at XL and over the entire period for REF. At ML, however, the amount of vegetation activity overwhelms the possible influence of traffic on daytime *FC* and [CO_2]. Negligible differences (ave. of 0.01 mg CO_2 m^{-2} s^{-1} and -2.88 ppm) are noted between weekday and weekend days, suggesting the CO_2 budget in the well-irrigated mesic landscaping is controlled by photosynthetic uptake of CO_2 by turf grass and trees. A decrease in *FC* during weekends has also been found for open low-rise areas (Coutts et al., 2007; Bergeron and Strachan, 2011; Buckley et al., 2016; Weissert et al., 2016; Song et al., 2017), open and compact mid-rise sites (Velasco et al., 2005, 2016; Pawlak et al., 2011; Hirano et al., 2015; Stagakis et al., 2019), compact low-rise locations (Velasco et

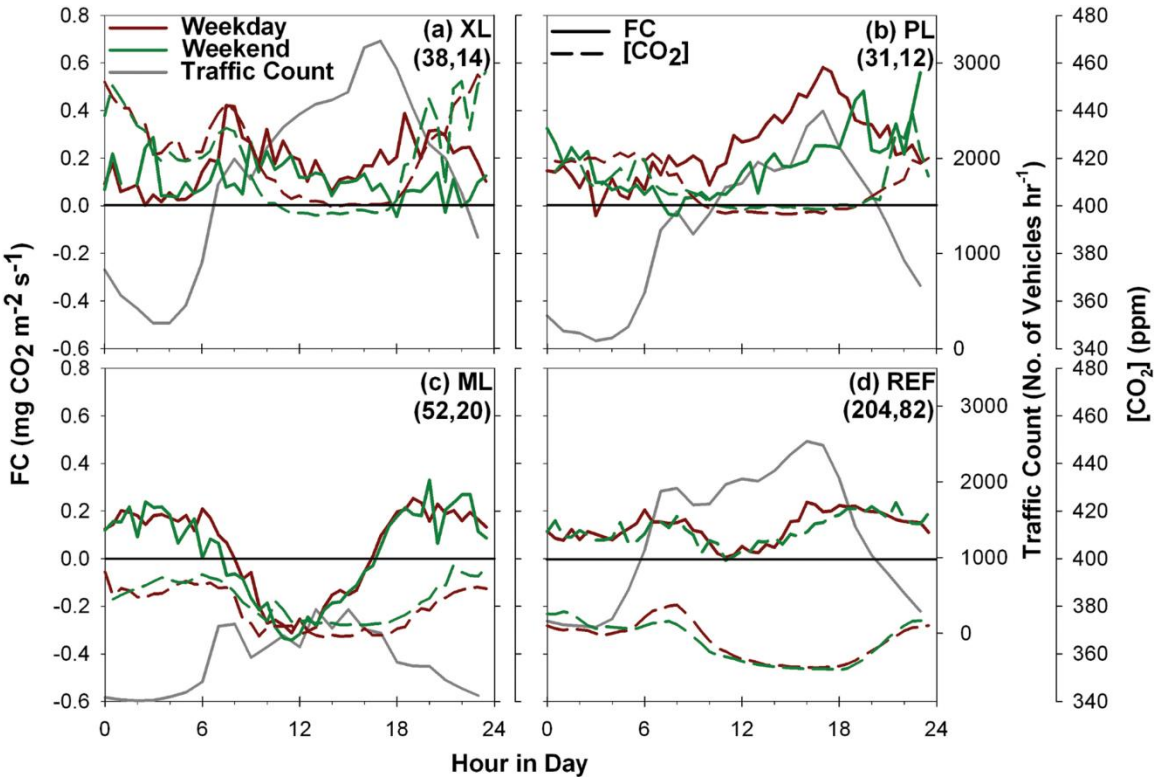

Figure 2.6: Diurnal averages of *FC* for weekday and weekend days. Comparison of the average diurnal cycles of carbon dioxide flux for weekday and weekend days for the (a) XL, (b) PL, (c) ML, and (d) REF sites, including traffic counts from nearby streets. Parentheses indicate the number of days in each category of weekday and weekend for each site, respectively. Different sampling periods are specified in each plot.

al., 2013, 2014; Buckley et al., 2016) and some sparsely built areas (Bergeron and Strachan, 2011). In contrast, this effect has not been noted in highly-vegetated urban areas (Hiller et al., 2011).

To isolate the vegetation controls, Figure 2.7 compares the average diurnal cycle of *FC* and [CO_2] for sunny and cloudy days during both weekday and weekend days with the incoming solar radiation for each category shown as a reference. This analysis allows inspecting the effect of plants on the CO_2 budget as sunny (cloudy) days promote (diminish) photosynthetic activity, whereas the value of R_s should not impact other controlling factors such as traffic. Prior work has compared *FC* with radiation data or plant phenology to analyze the role of vegetation on urban carbon dioxide fluxes

(Bergeron and Strachan, 2011; Crawford et al., 2011; Ward et al., 2015; Buckley et al., 2016; Ueyama and Ando, 2016). Since less than 20% of the days in a year are cloudy in the PMA (Schmidli, 1996), we use the effects of clouds on radiation to discern the role of photosynthesis. During the study period, the percentage of cloudy days were 15.4%, 7.0%, 8.3% and 10.8% of the sampling durations at XL, PL, ML, and REF, respectively. In addition, CC values between *NDVI* and CO_2 conditions are shown in Table 2.5 as a means to determine if significant relationships exist with vegetation development. Sunny days generally lead to lower *FC*, but not necessarily to lower [CO_2], in particular during mid-day, with average differences of -0.08 (XL), 0.0 (PL), -0.07 (ML), and -0.02 mg CO_2 m^{-2} s^{-1} (REF); and -3.61 (XL), 3.16 (PL), 9.98 (ML), and 3.89 ppm (REF), respectively. *FC* response is consistent with the vegetation fractions at XL (38.6%), PL (6.6%), ML (44.3%), and REF (14.6%). In addition, cloudy days exhibit higher *FC* during rush hour periods, suggesting that low vegetation activity in these few days in the PMA (note the low number of cloudy days) cannot counteract vehicle emissions, except at ML, where a significant change is not shown. Statistically significant relations with daily *NDVI* are only noted with [CO_2] at the REF site, suggesting that plant development has a minimal impact on *FC* or [CO_2] over the progression of each period. While there was plant development and phenological features observed during the study periods, these do not significantly impact the CO_2 budget during the deployments of XL, PL and REF but have an impact at ML. Furthermore, despite the mid-day decrease, vegetation activity did not completely counteract *FC* in XL, PL and REF, as these locations acted as net sources of carbon dioxide, however, vegetation activity in ML was enough to counteract this effect. These results are consistent with those reported in other cities, where highly-urbanized

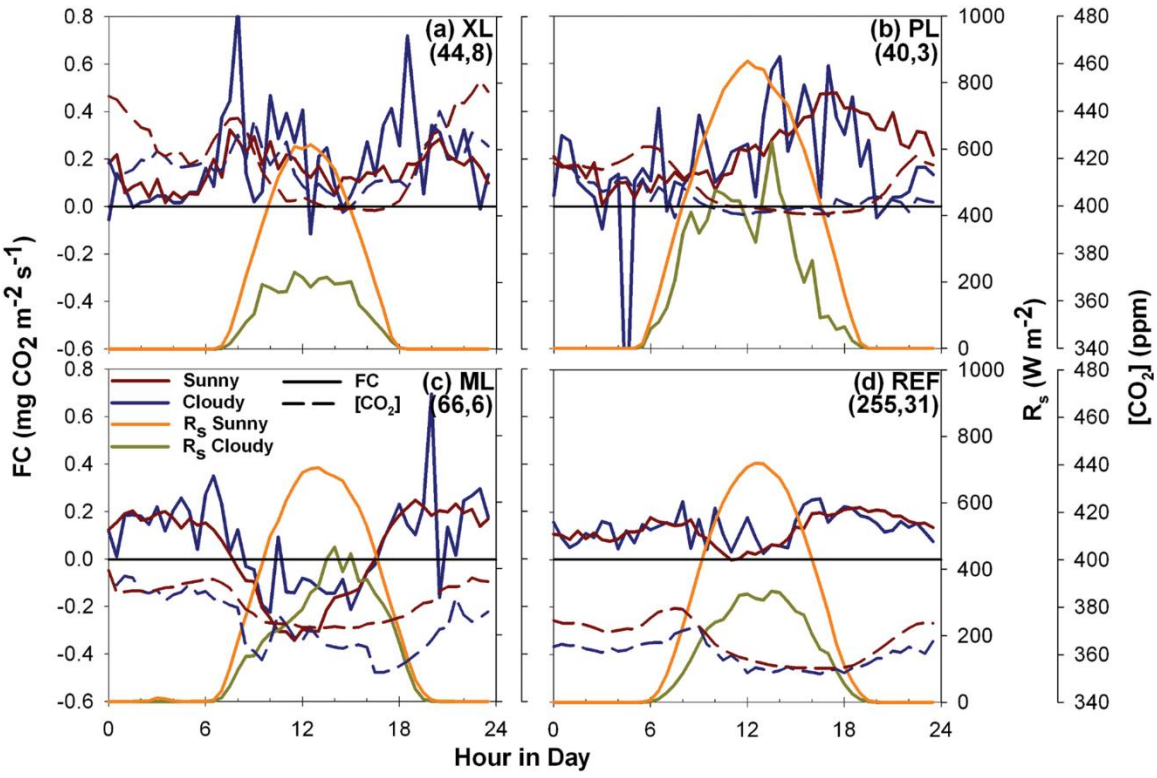

Figure 2.7: Diurnal averages of *FC* for sunny and cloudy days. Comparison of the average diurnal cycles of carbon dioxide flux for sunny and cloudy days for the (a) XL, (b) PL, (c) ML, and (d) REF sites, including average diurnal cycles of incoming solar radiation. Parentheses indicate the number of days in each category of sunny and cloudy for each site, respectively. Different sampling periods are specified in each plot.

areas are insensitive to changes in radiation, but highly-vegetated landscapes show differences between days with high or low radiation (Bergeron and Strachan, 2011; Crawford et al., 2011; Ward et al., 2015; Ueyama and Ando, 2016).

To summarize the controls on CO_2 conditions, Figure 2.8 presents the average *FC* and [CO_2] over each deployment period (and standard deviations as error bars) for weekday and weekend days (traffic effect), and for sunny and cloudy days (vegetation effect), including an indication of statistically significant differences ($p \leq 0.05$). As noted earlier, the XL and REF sites exhibit controls on *FC* that reflect a mixture of the effects

Table 2.5: Pearson correlation coefficient (CC) of daily values of Normalized Difference Vegetation Index with net radiation, latent heat flux, evaporative fraction, carbon dioxide flux and carbon dioxide concentration at all sites for simultaneous periods. Bolded numbers indicate significant correlations at $p \leq 0.05$.

Site	R_n	λET	EF	FC	$[CO_2]$
XL	0.00	0.13	0.24	-0.03	-0.17
PL	-0.08	0.03	-0.08	-0.25	-0.05
ML	0.07	0.39	0.09	0.04	-0.08
REF	**-0.21**	**-0.25**	**-0.23**	**-0.17**	**0.24**

of plant uptake and vehicular emissions, while a significant traffic effect is not present on $[CO_2]$ at the REF site. In contrast, the PL site is dominated by traffic effects with no statistically significant impact of vegetation activity on *FC*, though cloudy conditions impact $[CO_2]$ likely due to the effects of rainfall washout (Hemond and Fechner, 2015). Finally, the *FC* at the ML site is determined by plant uptake effects with no significant impact of traffic, whereas both controlling factors play a role on $[CO_2]$. The lower $[CO_2]$ for cloudy days could result from washout and local modifications by storm events (Hemond and Fechner, 2015). These results are consistent with the distribution of urban land cover types at each site, in particular the fraction of transportation surfaces and irrigated plants.

Sensitivity to precipitation and urban irrigation

The sensitivity of daily *FC*, $[CO_2]$, and *EF* to precipitation occurrence is assessed in Figure 2.9 through comparisons between wet and dry days at each study site. Wet days include those days with $P > 0.2$ mm day^{-1} and the two subsequent days after the

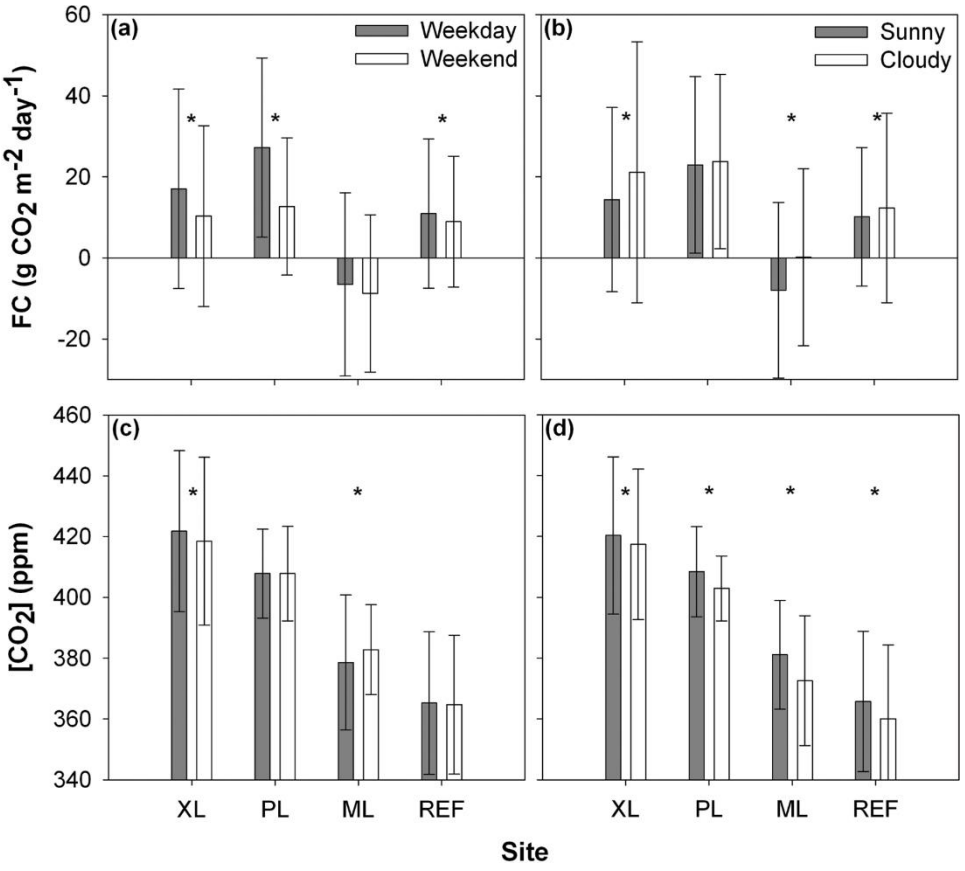

Figure 2.8: Average comparison between weekdays and weekends and sunny and cloudy days. Average values (bars) and standard deviations (error bars) of CO_2 flux and concentrations for (a, c) weekday and weekend, and (b, d) sunny and cloudy days for the XL, PL, ML, and REF sites. Stars indicate significant differences within each site ($p \leq 0.05$).

precipitation event to account for moist soil conditions. Significance tests ($p \leq 0.05$) are conducted between wet and dry days (labeled with *) within each deployment as well as between each mobile site and REF for simultaneous periods (labeled with +). While storm events are infrequent (note the lower *n* for wet days), these lead to significantly higher *EF* at the XL and PL sites with relatively lower amounts of vegetation, but no effect at the irrigated turf grass of the ML site. As discussed in Templeton et al. (2018), this is likely due to the mesic or well-watered conditions at ML which maintain high *EF* that is insensitive to additional water input from storm events. Both wet and dry days

have statistically significant differences in *EF* between each deployment and the REF site. CO_2 concentrations vary significantly between wet and dry days at XL and PL, but not at the ML site, likely due to the negligible influence of precipitation on turf grass conditions. As expected, there are significant differences in [CO_2] between each deployment and the REF site due to the effect of different sensor heights. Similarly, daily *FC* varies significantly between the mobile and REF sites for both dry and wet days, attributed to differences in CO_2 emissions by vehicles and uptake by vegetation. However, the effect of precipitation occurrence was just evident at the PL site which had the lowest vegetation fraction. At the XL and ML sites, where a sufficient level of irrigated vegetation is present, *FC* does not significantly change in response to the additional water provided by storm events, though small increases in *FC* are present for wet days. The lower sensitivity of *FC* to rainfall at both the ML and XL sites suggests that plant photosynthesis occurs under well-watered conditions at these locations, whereas the use of *EF* as a diagnostic tool of this effect (Templeton et al., 2018) identifies only the ML site as functioning as a mesic site.

To explore this further, Figure 2.10 describes the response of *FC* to precipitation input for the sequence of days after rainfall at each study site. In this analysis, all periods after every storm are analyzed by inspecting the daily *FC* to obtain an average value for all events, up to a maximum of 8 days after the event. Standard deviations across events for each day after a rainfall day are shown as error bars (± 1 std). Linear regressions ($y = mx + b$) of the averaged *FC* with days after a rainfall event are conducted to test the sensitivity of CO_2 fluxes to the storm event. We tested whether the slope of the linear regression (m) was significantly different from zero at $p \leq 0.05$. Daily *FC* variations are

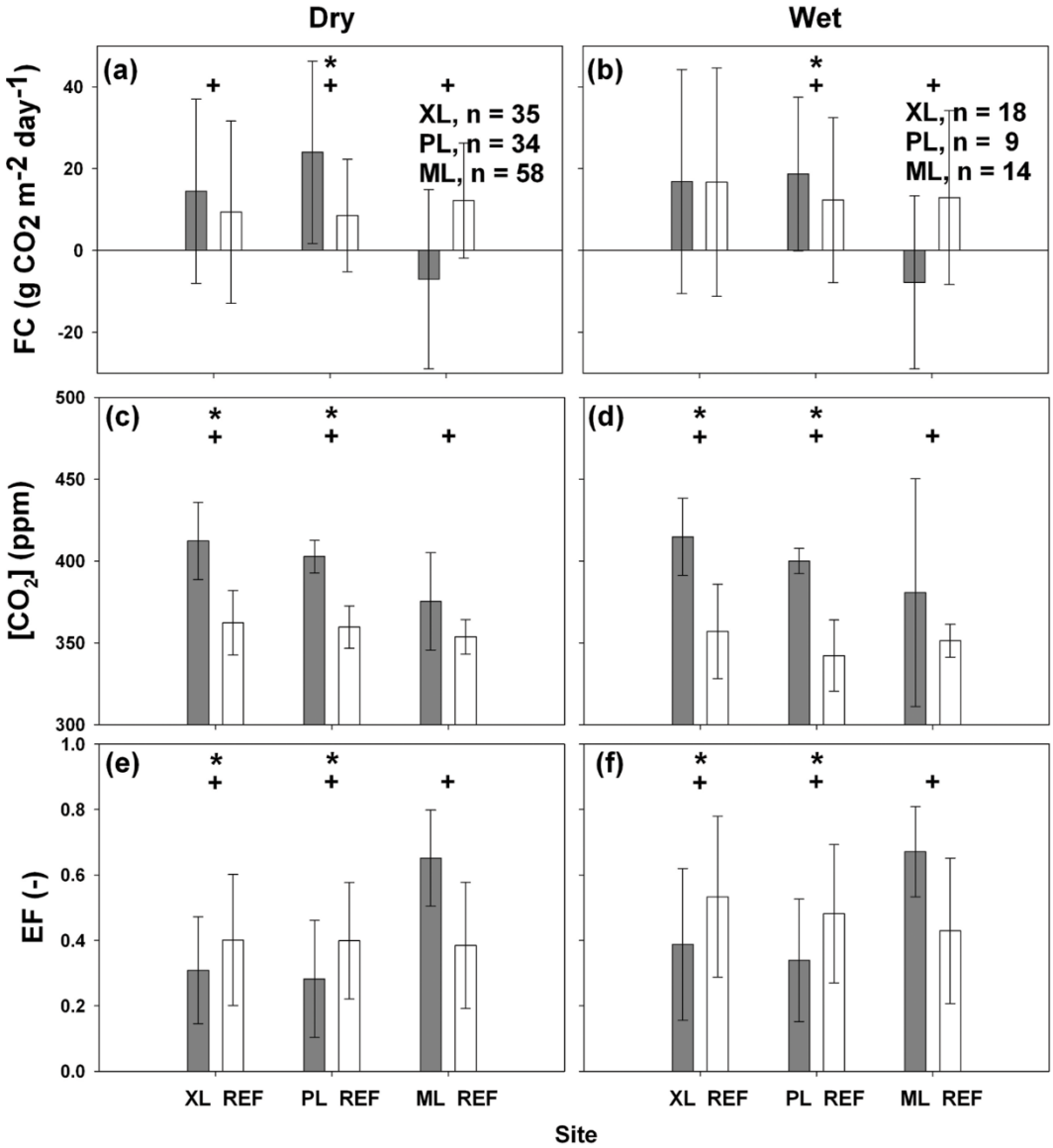

Figure 2.9: Daily averages of *FC*, [CO_2] and *EF* for dry and wet days. Comparisons of averaged daily (a, b) *FC*, (c, d) [CO_2], and (e, f) *EF* for dry (left) and wet (right) days during simultaneous periods. *n* is the number of days and error bars represent ±1 daily standard deviations. Statistical significance ($p \leq 0.05$) is tested between dry and wet days in the same site (shown with *) and between the mobile deployment and REF site (shown with +).

sensitive to storm events only at the XL site (*m* = -1.59, Figure 2.10a), whereas the PL, ML, and REF sites have daily *FC* that is insensitive to precipitation (*m* of -0.06, 0.17, and -0.4 that are not significantly different from zero). This is consistent with the average *FC* differences between wet and dry days (Figure 2.9), but yields additional information on

the rate of *FC* changes with time after a rainfall event, including insight on the transition from wet to dry days. Notably, the xeric landscaping with irrigated trees at XL had progressively more CO_2 uptake (lower *FC*) as time progressed after rainfall events during the winter-spring. A similar behavior occurs at the REF site during the same period as XL (Figure 2.10b, m = -1.43, significantly different from zero), indicating that the CO_2 uptake occurred across different urban landscapes and was likely tied to seasonal (winter-spring) conditions promoting a photosynthetic response of xeric trees. For instance, we visually noted that palo verde flowered after these winter-spring rainfall events. In contrast, the parking lot at PL exhibited a very small increase in CO_2 emissions (higher *FC*) after rainfall events during the early summer that was also noted at REF (Figure 2.10b), but not at a significant level (m = 0.33). This suggests that additional water from precipitation during a period of high temperatures in May and June promotes CO_2 efflux, mainly by increasing soil respiration in bare soil areas, in a similar fashion as noted in natural ecosystems of the region (Scott et al., 2004; Perez-Ruiz et al., 2010; Verduzco et al., 2015, 2018). During other times of the year, the site with ample outdoor water use (ML) does not respond to precipitation (*FC* remains the same), suggesting that a decoupling occurs between CO_2 fluxes and storm inputs as commonly found in mesic regions.

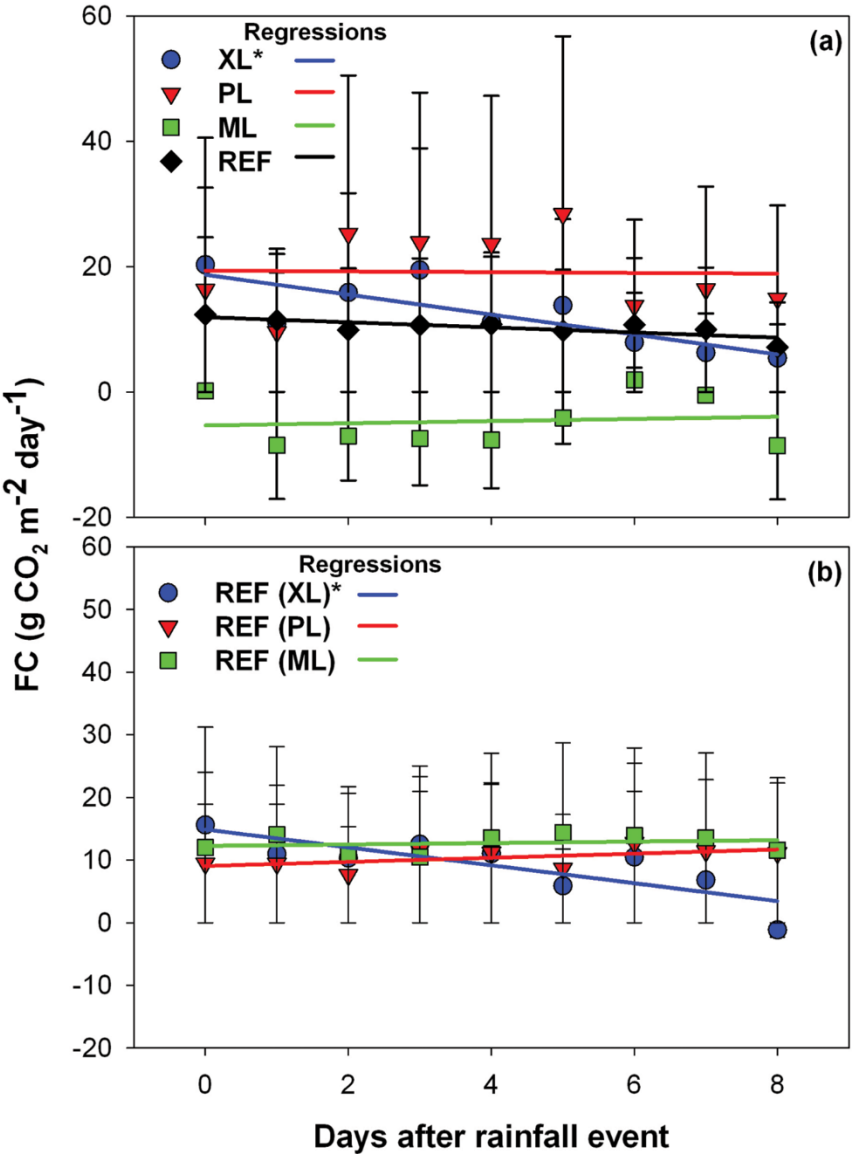

Figure 2.10: Response of daily *FC* to precipitation pulses. Daily *FC* as a function of days after a rainfall event for (a) all sites during their respective deployment periods, and (b) for the REF site during periods equal to temporal deployments at XL, PL, and ML. Symbols indicate averages and error bars depict ±1 standard deviation across all events. The linear regression slope is significantly different from zero at $p \leq 0.05$ for the regressions labeled with an asterisk (*).

Conclusions

While bottom-up approaches have been used to estimate CO_2 exchanges in arid and semiarid cities, few studies have carried out direct observations in different urban patch types. Indeed, a comparison of these approaches is warranted as the number of direct

observations grows. At present, there are only a small number of studies discussing the controlling factors on *FC* and [CO_2], such as vehicular emissions and plant photosynthetic activity, and their link to the proportion of these urban land covers within a site (for instance, Christen et al., 2011; Volo et al., 2014; Buckley et al., 2016; Crawford et al., 2016; Ueyama and Ando, 2016¸ Järvi et al., 2019), though the temporal variation in vegetation and anthropogenic activity has typically not been taken into account to date. In this study, we conducted turbulent flux measurements using the EC technique to obtain a detailed view of CO_2 fluxes and relate these to local meteorological conditions and urban characteristics for three short-term deployments and a stationary reference site in Phoenix, Arizona, USA. Comparisons to the suburban reference site were conducted during simultaneous periods for different seasons such that measured differences could be attributed to local variations in urban conditions. Results from the comparisons across the sites, seasons, and urban land cover types indicated the following:

(1) Despite the small differences noted in meteorological conditions, the magnitude and behavior of *FC* and [CO_2] varied considerably among the sites, in manners consistent with the urban land cover type. XL, PL, and REF acted as net sources of carbon dioxide, though plant activity was able to counteract anthropogenic emissions during mid-day periods. At ML, the well-watered turf grass was a net sink of CO_2 during the summer season.

(2) Diurnal variations in *FC* and [CO_2] exhibited a strong correspondence to rush hour timing and vehicular counts for sites with large fractions of transportation surfaces, depending on local traffic behavior. Statistically significant differences were noted in *FC* between weekday and weekend days for all sites, except where vegetation activity served

as a carbon dioxide sink. Vehicular emissions led to a temporal decoupling of CO_2 and water vapor fluxes during the day.

(3) Where urban irrigation supports a plant community, mid-day values in *FC* and [CO_2] showed decreases consistent with the increase in measured latent heat flux. Statistically significant differences were noted in *FC* and [CO_2] between sunny and cloudy days for most sites, except where the vegetation cover was low. A close correspondence was noted in the daily peak timing of CO_2 and *ET* fluxes where outdoor water use supports plant photosynthesis.

(4) The sensitivity of *FC* and [CO_2] to precipitation events varied considerably among the sites in accordance with the proportion of irrigated vegetation. Where outdoor water use is abundant and frequent, CO_2 conditions are insensitive to the occurrence of precipitation (wet versus dry days) or the time since the last rainfall event. This decoupling between CO_2 fluxes and storm inputs suggests that irrigated landscapes in arid urban areas behave as mesic systems.

Based on these comparisons, key differences in the CO_2 conditions can be attributed to the vegetation fraction and built surfaces in urban patches. Two of the sampled sites can be considered as end members that are dominated either by the effects of traffic and other anthropogenic emissions (PL) or by the carbon dioxide uptake from photosynthetic activities of turf grass and trees (ML). The other two sites (XL and REF) are characterized by combinations of these land cover types and thus exhibit intermediate or mixed behavior with respect to CO_2 conditions. As noted by Templeton et al. (2018), it would be desirable to conduct cross-site comparisons of this type over at a full year or

longer to assess net effects of vehicular traffic and vegetation activity on CO_2 fluxes. Such a study could also quantify the seasonal variations in these factors responding to plant phenology and temporal changes in anthropogenic activities. For instance, the role played by seasonality and its interaction with irrigation is considered important in determining if plant activity can fully counteract anthropogenic CO_2 emissions during an annual period. For the periods studied here, vegetation could not counteract CO_2 emissions, leading to a net carbon dioxide source at all sites, including the mesic landscaping. Nevertheless, this cross-site comparison suggests a fruitful avenue for scaling up CO_2 conditions to larger areas by using the fraction occupied by urban vegetation and built surfaces. Following this strategy could lead to considerable improvements in bottom-up estimates of CO_2 fluxes and concentrations to better capture the anticipated spatiotemporal variability in desert cities.

CHAPTER 3

LANDSCAPE CONTROLS ON WATER-ENERGY-CARBON FLUXES ACROSS DIFFERENT ECOSYSTEMS DURING THE NORTH AMERICAN MONSOON

Introduction

The North American monsoon (NAM) is characterized by increased rainfall from July to September over southwestern United States and northwestern México (e.g., Douglas et al., 1993; Adams and Comrie, 1997), leading to changes in ecosystem conditions and land-atmosphere interactions (Vivoni et al., 2007, 2008; Méndez-Barroso and Vivoni, 2010; Pérez-Ruiz et al., 2010; Forzieri et al., 2011). Water-limited ecosystems typically respond to the onset and demise of the NAM through changes in pulses of microbial activity, leaf and canopy development, and plant photosynthesis (e.g., Scott et al., 2010; Lizárraga-Celaya et al., 2010; Méndez-Barroso et al., 2014; Biederman et al., 2018; Verduzco et al., 2018). As a result, a strong connection is presumed between the temporal distribution of rainfall during the NAM and the ecosystem processes influencing the exchange of water, energy, and carbon with the overlying atmosphere. However, it is relatively unknown how variations in access to groundwater and microclimatic and soil conditions related to elevation might modulate these ecosystem responses.

Water-limited ecosystems have been identified as playing an important role in the carbon cycle due to their strong inter-annual variability in productivity (e.g., Poulter et al., 2014; Ahlström et al., 2015). While the NAM exhibits rainfall variability from intra-seasonal to inter-annual time scales (e.g., Higgins et al., 1999; Cavazos et al., 2002), its

effect on land-atmosphere interactions, in particular carbon dioxide (CO_2) fluxes, has yet to be compared to perennial surface and subsurface water sources across different ecosystems. Widespread vegetation greening due to the synchronized availability of rainfall and solar radiation is thought to be a controlling factor on water-energy-carbon fluxes (e.g., Vivoni et al., 2010; Forzieri et al., 2011, 2014; Méndez-Barroso et al., 2014). However, landscape controls, such as elevation effects on microclimate conditions and a consistent access to groundwater, can also play a fundamental role in differentiating the individual responses of ecosystems. Two plant greening or phenological strategies linked to intensive and extensive water use (Rodríguez-Iturbe et al., 2001; Lagergren et al., 2008; Wang et al., 2011; Barron-Gafford et al., 2013; Jia et al., 2014; Scott et al., 2014; Wang et al., 2016, Zhao et al., 2016; Rodríguez-Robles et al., 2017) have been noted in the region through inspection of the ecosystem phenological response during the summer season. Intensive water users such as drought-deciduous species exhibit a rapid, but short period of greening after the onset of the NAM, while extensive water use strategies in primarily evergreen species favor a prolonged period of moderate greenness continuing after the NAM.

The groundwater dependence of mountain and riparian ecosystems in the NAM region is relatively unexplored, though this has been reported in other seasonally dry areas (e.g., Baldocchi et al., 2004; Paco et al., 2009). The works of Potts et al. (2008), Barron-Gafford et al. (2013), and Scott et al. (2014), for instance, identified differences between mesquite savannas growing in riparian areas versus those in upland locations and concluded that groundwater access impacted how water-energy-carbon fluxes were dependent on rainfall. Similarly, Brunel (2009) showed that riparian mesquite trees can

access either soil water or groundwater depending on available rainfall and the depth to the alluvial water table. Yet, the contributions of microclimate conditions, such as air temperature, vapor pressure deficit and soil water, and the site access to groundwater, have not be elucidated. While these effects can be hard to isolate, observational studies can provide valuable insights if site differences exist across multiple landscape controls (Hui et al., 2003; Barron-Gafford et al., 2013; Shao et al., 2016; Rojas-Robles et al., 2020).

One of the challenges to assessing the dependence of water-energy-carbon fluxes to landscape controls is the difficulty of obtaining simultaneous observations in ecosystems that are generally in inaccessible areas due to rugged terrain. The eddy covariance (EC) technique (Baldocchi et al., 2001) is often used to measure fluxes at the ecosystem level, expressed in terms of the net ecosystem exchange (*NEE*), latent heat flux (λET), and sensible heat flux (*H*). A large number of independent studies have been conducted in ecosystems under the influence of the NAM, for instance in grasslands (Kurc and Small, 2007; Bowling et al., 2010; Barron-Gafford et al., 2013; Hinojo-Hinojo et al., 2016, 2019), woody savannas (Scott et al., 2009; Potts et al., 2010), riparian ecosystems (Scott et al., 2004, 2008, 2014; Williams et al., 2006; Yépez et al., 2007), shrublands (Kurc and Small, 2007; Potts et al., 2008; Vivoni et al., 2021), subtropical scrublands (Méndez-Barroso et al., 2014; Verduzco et al., 2018), semiarid woodlands (Pérez-Ruiz et al., 2010; Verduzco et al., 2015), and forests (Méndez-Barroso et al., 2014; Knowles et al., 2020). However, few studies have coordinated sampling across different ecosystems under a similar seasonal rainfall regime, but under variations in elevation and groundwater

access, to identify how landscape controls might differentially impact water-energy-carbon fluxes.

Here, we conduct a field campaign in the summer of 2017 in three ecosystems in México that offered the opportunity to determine the relative roles of groundwater access and elevation-induced differences in soil and microclimate conditions. Sites were a subtropical scrubland depending on shallow soil water, a riparian mesquite with intermediate access to groundwater, and an oak savanna with stable subsurface water in a mountain setting. Unfortunately, a high elevation site depending only on shallow soil water was not sampled. Differences in vegetation phenology (e.g., greening onset and duration, peak green-up, time-integrated green-up amount), as observed from remote sensing (Méndez-Barroso et al., 2009; Forzieri et al., 2011) for these ecosystems, suggest that a link might exist with landscape controls. While Méndez-Barroso et al. (2014) identified differences in vegetation phenology and seasonal evapotranspiration rates at two of the sites, the study was not able to distinguish sources of water nor link the plant water uptake to carbon fluxes. We deployed sensors at the subtropical scrubland and oak savanna sites that form part of the MexFlux network (Vargas et al., 2013; Delgado-Balbuena et al., 2019), but which had been discontinued, and expanded observations to a third site in a riparian mesquite woodland to allow comparisons of the landscape controls described above. The new site offered the opportunity to identify how access to groundwater at a low elevation influenced the water-energy-carbon fluxes. However, logistical restrictions of the rural sites in México constrained the field campaign to a single summer season. Nevertheless, we sampled a key period in the year which has a

large contribution to annual rainfall (Douglas et al., 1993) and a preponderant role in annual carbon fluxes (Verduzco et al., 2015, 2018).

Our aim is to quantify land-atmosphere interactions during the evolution of the NAM to elucidate if (1) soil and microclimate conditions induced by variations in elevation or (2) groundwater access linked to the terrain position play a more significant role in the ecosystem response. The sampled gradient has the potential for a similar rainfall due to the close proximity of the sites (Mascaro et al., 2014). However, site variations in elevation, access to groundwater, and vegetation phenology provide a means to isolate the individual effects on the water-energy-carbon fluxes. We emphasize the CO_2 exchanges since these have not been characterized at these sites and can provide evidence on the water use strategies that have been previously inferred only from vegetation phenology and evapotranspiration (Forzieri et al., 2011; Méndez-Barroso et al., 2014). To guide our study, we posed the following questions: "What are the relative roles of soil and microclimatic conditions and access to groundwater on water-energy-carbon fluxes?" and "How are differences in these controls linked to intensive and extensive water use strategies?". In this analysis, we differentiate between near surface conditions, specifically air temperature, vapor pressure deficit and shallow soil moisture, and deeper subsurface water sources. We hypothesize that water-energy-carbon fluxes will vary significantly in the presence of stable groundwater that can provide a buffer to the high temporal variability of seasonal rainfall.

Methods

Study Area Description

The three EC sites were deployed in a rural, sparsely populated region in Sonora, México, arranged in a triangular pattern at ~25-km distances (Figure 3.1). The sites are: (1) a subtropical scrubland (SS) located on top of an alluvial fan (29.741 °N, 110.537 °W) at an elevation of 622 m with thorny, deciduous trees (4 m height), shrubs, cacti, and low grass cover and coarse, rocky soils; (2) a riparian mesquite (RM) located in a valley bottom near an ephemeral channel (29.944 °N, 110.613 °W) at an elevation of 681 m with tall mesquite trees (8 m height) and moderate grass cover on a coarse soil matrix; and (3) an oak savanna (OS) located in a mountain saddle (29.958 °N, 110.461 °W) at an elevation of 1314 m with oak trees (5.5 m height) interspersed with grasses and succulents upon coarse, rocky soils with an abundant organic matter horizon (Méndez-Barroso et al., 2014; Ko et al., 2019). The velvet mesquite (*Prosopis velutina*) and oak (*Quercus chihuahuensis, Quercus oblongifolia*) trees at RM and OS, respectively, are known to have deep roots, extending beyond 2 m in depth (Cable, 1977; Shenk and Jackson, 2002; Baldocchi et al., 2004), while the understory grasses have shallow roots. At SS, grasses, shrubs, cacti, and shallow rooted trees have limited access to water below the upper soil profile (Tarín et al., 2020). Note that SS and OS are documented as part of the MexFlux network but had been discontinued prior to this effort (Vargas et al., 2013; Delgado-Balbuena et al., 2019), while RM represents a new site with riparian characteristics not captured in MexFlux. Site conditions and their representativeness in the broader domain are shown in Figure 3.2. In all cases, the two-dimensional footprint for the 80% source area (Kjlun et al., 2015) was within 150 m of the site in an area with homogenous vegetation for each ecosystem.

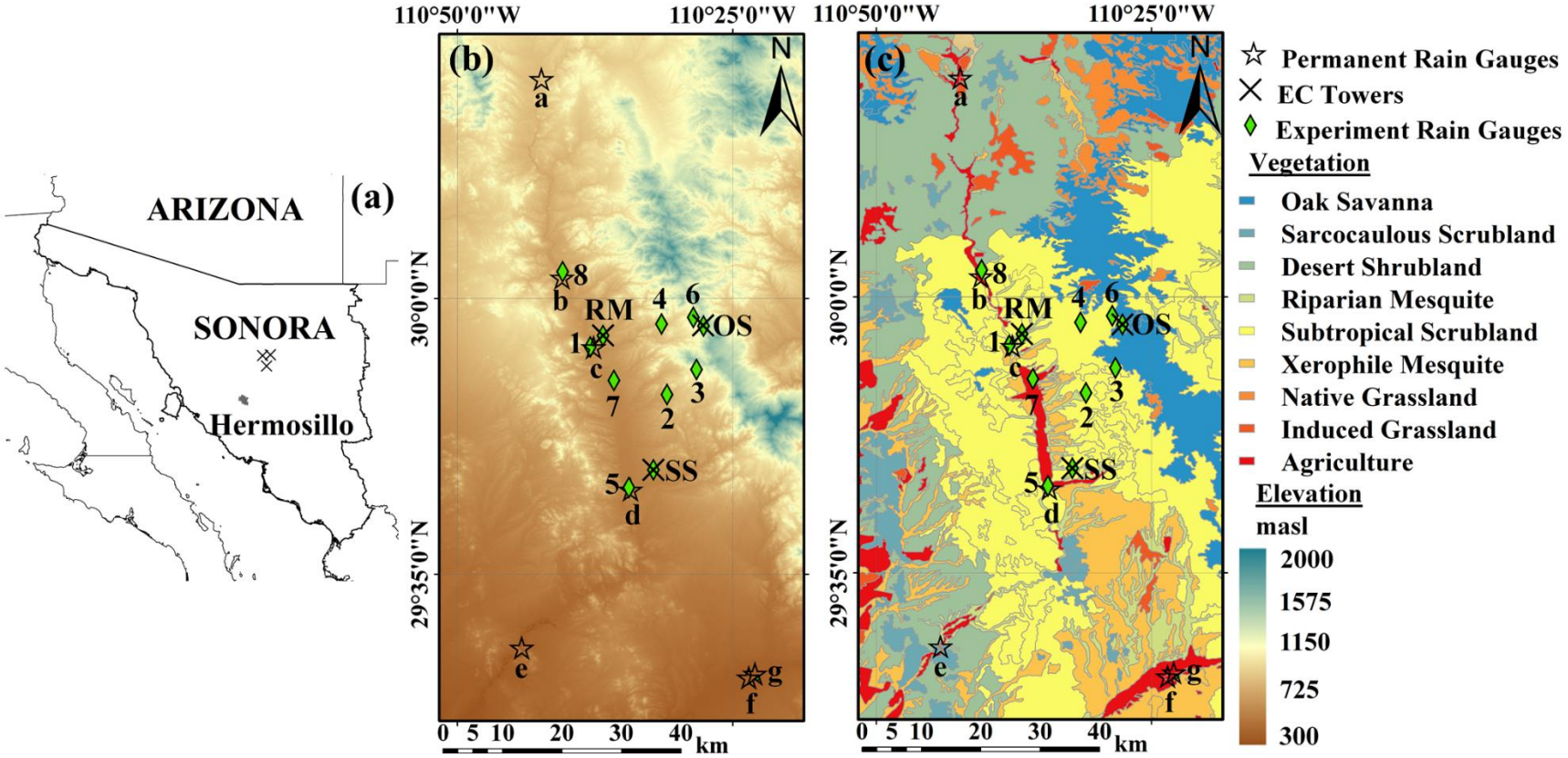

Figure 3.1: Location of the study sites in: (a) the state of Sonora, México and in relation to (b) elevation, and (c) vegetation type. Numbers and letters represent the ID of each rain gauge site. Elevation from the Continuo de Elevación Mexicano 3.0 and the vegetation type from the Conjunto de Datos Vectoriales de Uso de Suelo y Vegetación of INEGI (2016).

Climate in the area is classified as steppe or semiarid (BhS) according to Köppen-Geiger (Peel et al., 2007), characterized by hot, arid conditions; winter temperatures above 0 °C; and warm season rainfall (*R*). According to seven permanent rain gauges in the region (Table 1), the mean annual rainfall is 469 mm per year, with more than 65% occurring during the NAM (July, August and September). Daily visual measurements of rainfall are made at permanent rain gauges by the Comisión Nacional de Agua (CONAGUA) in small towns at low elevations. To complement these observations, a network of 11 continuous, tipping-bucket rain gauges (TE525, Texas Electronic, Dallas, TX) were deployed during the field campaign at elevations ranging from 558 to 1462 m (Table 3.1). Three of these rain gauges are co-located with the EC sites, while the remainder allow for characterizing the spatial variability of rainfall in the region.

Eddy Covariance Measurements and Data Processing

High frequency measurements of water, energy, and carbon fluxes were obtained with the EC method (Baldocchi, 2003). EC systems consisted of an infrared gas analyzer (IRGA) to measure H_2O and CO_2 concentrations and a sonic anemometer to measure wind components. The IRGA consisted of a LI-7500 for SS and RM, and a LI-7500RS (both from Li-COR Biosciences, Lincoln, Nebraska) for OS. The sonic anemometers were a CSAT-3 (Campbell Scientific, Logan, Utah) for SS and RM, and a Windmaster Pro (Gill Instruments, Hampshire, UK) at OS. EC systems were installed at 9, 12, and 9 meters above the ground surface at the SS, RM, and OS sites, respectively. Fluxes were calculated at 30-minute intervals with the software EddyPro® 6.2.0.

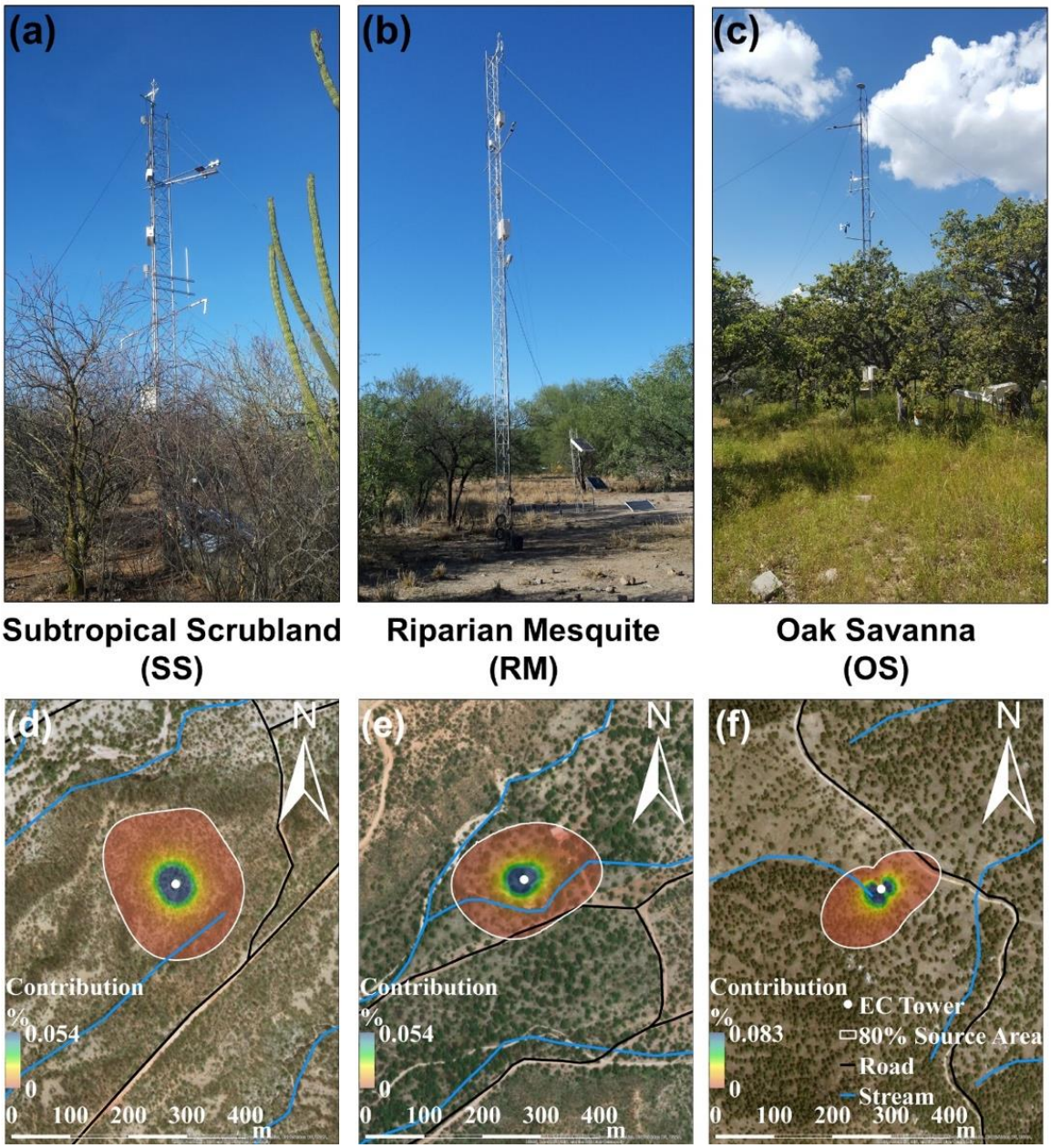

Figure 3.2: Photographs showing the EC sites and the ecosystems at the three sites: (a) Subtropical Scrubland, (b) Riparian Mesquite, and (c) Oak Savanna. (d), (e), and (f) show the 80% footprint source area (colors are percent contribution of each 1-m pixel) of the area around each EC site.

Table 3.1: Characteristics of the campaign and permanent rain gauge sites. Summer *R* determined from 06/15/2017 to 09/28/2017 at all sites. Italics represent the three EC sites.

Campaign Rain Gauges							
ID	**Rain Gauge Site**	**Longitude (dd)**	**Latitude (dd)**	**Elevation (m)**	**Start Period**	**End Period**	**Summer *R* (mm)**
1	Opodepe	-110.631	29.927	639	5/15/17	11/17/17	294.9
2	El Saucito	-110.516	29.855	812	5/15/17	11/18/17	334.5
3	El Tule	-110.471	29.893	1118	5/15/17	11/18/17	542.0
4	La Ramada	-110.524	29.962	852	5/15/17	11/17/17	322.8
5	Rayon	-110.573	29.714	558	5/15/17	11/17/17	244.6
6	Sierra Los Locos	-110.476	29.972	1268	5/15/17	11/8/17	277.4
7	Santa Margarita	-110.596	29.876	622	6/15/17	9/28/17	560.6
8	Meresichic	-110.673	30.040	721	6/15/17	9/28/17	250.4
SS	*Subtropical Scrubland*	-110.537	29.741	622	6/11/17	10/7/17	275.4
RM	*Riparian Mesquite*	-110.613	29.944	681	5/29/17	10/9/17	260.1
OS	*Oak Savanna*	-110.461	29.958	1462	5/24/17	10/8/17	254.2
Permanent Rain Gauges							
ID	**Rain Gauge Site**	**Longitude (dd)**	**Latitude (dd)**	**Elevation (m)**	**Period**		**Summer *R* (mm)**
a	Cucurpe	-110.706	30.331	853	1967-2011		315.4
b	El Cajon	-110.736	29.472	390	1974-2011		290.5
c	Meresichic	-110.675	30.031	712	1980-2011		345.4
d	Opodepe	-110.627	29.926	663	1944-1983		314.8
e	Rayon	-110.571	29.711	560	1974-2011		334.9
f	Ures SMN	-110.383	29.433	397	1921-1977		323.8
g	Ures	-110.392	29.427	385	1978-2011		276.1

An initial quality check was performed consisting of a spike detection and a removal procedure using a maximum of three consecutive outliers (Vickers and Mahrt, 1997) and outliers greater than 3 standard deviations (std) for gas concentrations and 5 std for wind components (Schmid et al., 2000), and an amplitude resolution with a range of variation above 7 std (Vickers and Mahrt, 1997). We set initial absolute limits for zonal velocity (-30 to 30 m s^{-1}), meridional velocity (-5 to 5 m s^{-1}), sonic temperature (-20 to 50 °C), CO_2 concentration (200 to 600 µmol mol^{-1}), and H_2O concentration (0 to 40 mmol mol^{-1}).

Flux processing included detrending by block averaging and time lag compensation by covariance maximization (Moncrieff et al., 1997; Massman, 2001), axis rotation by double rotation (Wilczak et al., 2001), low-frequency correction using the analytical correction of high-pass filtering effects (Moncrieff et al., 2004), corrections for stability and density fluctuations (Webb et al., 1980; Foken et al., 2006), and estimates of sensible heat were obtained from the sonic temperature (Paw U et al., 2000). An angle of attack correction (Nakai and Shimoyama, 2012) was applied at the OS site. Average half-hour corrected fluxes were also filtered to exclude periods with rainfall (R > 0.2 mm per 30-min) and when winds were ±10˚ from the opposite direction of the mounted instruments. Range limits were set for net ecosystem exchange (NEE ± 1.3 mg CO_2 m^{-2} s^1), latent heat flux (λET from -50 W m^{-2} to 450 W m^{-2}), and sensible heat flux (H from 200 W m^{-2} to 800 W m^{-2}), following the procedures of Schmid et al. (2000). Finally, fluxes were filtered using a friction velocity criterion of u^* < 0.10, 0.14, and 0.24 m s^{-1} for SS, RM, and OS, to exclude spurious data under stable atmospheric conditions. The u^* thresholds were estimated using the Moving Point Test (Papale et al., 2006). Gap filling of the flux data was applied using the methods of Reichstein et al. (2005) through the tool REddyProc (Wutzler et al., 2018). During the sampling period, there were about 29% (SS), 49% (RM), and 45% (OS) of missing data due to sensor failures, quality control, and other maintenance issues. Generally, gaps were evenly distributed throughout the study period, except at RM where a 23-day gap was present from mid-July to mid-August due to major physical damage at the site.

To complement the *NEE* measurements, we estimated ecosystem respiration (R_{eco}) and gross primary productivity (*GPP*) using a flux partitioning tool in REddyProc. *GPP*

and R_{eco} allow distinguishing the temporal behavior on ecosystem carbon uptake and release, respectively. This procedure was based on the night-time sensitivity of *NEE* to air temperature (T_{air}) using the exponential regression model of Lloyd and Taylor (1994) as:

$$R_{eco}(T_{air}) = R_{ref} e^{E_0\left(\frac{1}{T_{ref}-T_0}-\frac{1}{T_{air}-T_0}\right)}, \quad (3.1)$$

where R_{ref} is the reference respiration at T_{ref} (10 °C), T_o equals -46.02 °C, and E_o is an activation energy parameter (207.30, 250.53, and 165.81 °K for SS, RM, and OS, respectively). In addition, we compared estimates of λET, H, and *NEE* at SS and OS to other available summer periods to quantify the representativeness of the conditions during the 2017 NAM season. At SS, summer datasets were averaged from 2008 to 2012, while OS was captured by averaged summer data from 2008 to 2014. As part of the quality control, we inspected the energy balance closure ($\varepsilon = \sum(H + \lambda ET) / \sum(R_n - G)$) for periods of simultaneously available fluxes (Table 3.2), finding that 65 to 90% of the available energy ($R_n - G$) was measured as turbulent fluxes ($H + \lambda ET$). A lack of G measurements at OS throughout the study period (assumed $G = 0$) impacted the energy balance closure at this site. Overall, these results are within the range of other EC studies (34 to 169%) across different ecosystems (Wilson et al., 2002). Similarly, a regression of the form $H + \lambda ET = m(R_n - G) + b$ was performed, finding values of m and b that were generally within those reported (m from 0.55 to 0.99, b from -32.9 to 36.9) by Wilson et al. (2002).

Table 3.2: Energy balance closure using two techniques: (1) linear fit ($H + \lambda ET = m(R_n - G) + b$) with slope ($m$), intercept ($b$), and coefficient of determination (R^2), and (2) ε or the ratio of the sum of ($H + \lambda ET$) to the sum of ($R_n - G$). Note that OS had no G measurements (assumed zero).

Site	ε	Slope (m)	Intercept (b)	R^2
Subtropical Scrubland	0.92	0.64	53.97	0.84
Riparian Mesquite	0.87	0.72	27.60	0.86
Oak Savanna	0.65	0.52	25.43	0.83

Ancillary and Remotely-Sensed Datasets

Additional ancillary meteorological and soil measurements were obtained for each site, including: (1) air temperature (T_{air}) and relative humidity (RH) using a HMP45C sensor at SS, and a HMP155A sensor (both from Vaisala, Helsinki, Finland) at RM and OS; (2) net radiation (R_n) with a CNR2 sensor at SS and RM, and a CNR4 sensor (both from Kipp & Zonen, Delft, The Netherlands) at OS; and (3) soil water content using CS616 sensors (Campbell Scientific, Logan, Utah) at 5, 15 and 30 cm depths at RM and a set of HydraProbes (Stevens, Portland, Oregon) at 5 and 15 cm depths at SS and at 15 cm depth at OS, respectively. Due to the use of the CNR2 sensor, incoming solar radiation (R_s) was not measured at SS and RM. Nevertheless, a comparison of R_s from previous observations at SS and OS showed no statistically significant difference in energy input across the elevation gradient. Ground heat flux (G) was only available at SS and RM using a HFP01-L sensor with corrections made with soil thermometers (both from Campbell Scientific, Logan, Utah) at 2 and 4 cm. No measurements of G were obtained at OS. Volumetric soil water content values were converted to a relative water content (s) dividing by the maximum value at each site. Vapor pressure deficit (VPD) was calculated using T_{air} and RH.

In addition, we used remotely-sensed data on the Normalized Difference Vegetation Index (*NDVI*) derived from the Moderate Resolution Imaging Spectroradiometer (MODIS) surface reflectance composites (MOD09A1; ORNL DAAC, 2018) at 500-m pixel and 8-day resolution. *NDVI* observations, over the period of January of 2001 to December of 2018 were used for three purposes: (1) to estimate the temporal variation of vegetation greenness for the 500-m pixel containing each EC site during the field campaign, (2) to obtain the ecosystem-average conditions during the summer of 2017 for pixels corresponding to the same vegetation type as in the EC sites (INEGI, 2016), and (3) to estimate the long-term (2001-2018) conditions of vegetation greenness at the EC sites. For these purposes, *NDVI* was found to be suitable and we found no significant differences when inspecting the Enhanced Vegetation Index (*EVI*) in the region (Méndez-Barroso et al., 2009). In a similar fashion, we used rain gauges for two purposes: (1) to obtain the long-term monthly *R* at seven permanent locations, and (2) to calculate daily and monthly *R* for the summer of 2017 at eleven locations, including the EC sites.

Data Analysis

The study period was divided into four NAM stages for summer 2017: (I) pre-monsoon corresponding to the dry season when the vegetation was dormant, (II) early monsoon when the onset of rainfall promoted soil biological activity and canopy development, (III) late monsoon considered to be the maximum plant activity, and (IV) post-monsoon when leaf senescence began and ecosystems returned to dormancy. Note that labels I through IV are used to refer to these stages. Dates of the NAM stages began from Day of Year (DOY) 162, 149, and 144 for SS, RM, and OS, and extend as: (I) up to July 1 (DOY 182), (II) from July 2 to 19 (DOY 183 to 200), (III) from July 20 to August

28 (DOY 201 to 240), and (IV) after August 29 (DOY 241). The stages were selected to capture rainfall onset and the different responses of ecosystems during the NAM. The large gap at RM corresponded to stage III. For each stage, we conducted analyses of the daily variations of water-energy-carbon fluxes. Seasonal averages of daily meteorological variables (T_{air}, *VPD*, and *RH*), energy fluxes (*H* and λET), and carbon fluxes (*NEE*, R_{eco}, and *GPP*) were compared using the Kruskal-Wallis One Way Analysis of Variance on Ranks (ANOVA). Statistical analyses of the fluxes included daily values obtained from gap-filled data, whereas we excluded days with missing data from analyses of meteorological variables. If statistical significance was found ($p < 0.001$), the All Pairwise Multiple Comparison Procedures (Dunn's Method) was applied to find differences between the sites.

To evaluate the effects of landscape controls, we calculated the Inherent Water Use Efficiency (*IWUE*), the evaporative index (*EI*), and the evapotranspiration from groundwater (ET_{gw}) index at each site. *IWUE* is obtained at the ecosystem level as *IWUE* = (*GPP***VPD*) / *ET*, and considers carbon assimilation per unit of ecosystem water use, while accounting for the atmospheric water demand (Beer et al., 2009). *EI* or *ET*/*R* is the fraction of rainfall consumed by *ET* (Budyko, 1974). Water-limited ecosystems often exhibit a high *EI*, which can exceed unity if other water sources such as groundwater are used (Williams et al., 2012). ET_{gw} is the component of *ET* from groundwater obtained from a water budget approach that assumes an effective soil depth. Westenburg et al. (2006) showed that $ET_{gw} = ET - R + \underline{Z_r}\Delta S$, where $\underline{Z_r}\Delta S$ is the change in soil water storage (D*S*) over the soil depth (Z_r), assumed here as 40 cm at all sites due to the soil water measurement depths (Schreiner-McGraw and Vivoni, 2018), when there is negligible

runoff (Q) and deep percolation (P). While runoff measurements are not available at the sites, arid and semiarid ecosystems in the region generally have low Q relative to R and ET due to coarse and rocky soils as classified by INEGI (2016) (e.g., Yermosol at SS, Fluvisol at RM, and Lithosol at OS; all of coarse nature with sandy loam textures, Méndez-Barroso et al. (2014)). For instance, Vivoni et al. (2021) document long-term average Q/R values ranging from 3 to 7% in a mixed shrubland and a mesquite savanna. Thus, total evapotranspiration can be decomposed into contributions from groundwater (ET_{gw}) and soil water ($ET_s = R - \underline{Z_r}\mathrm{D}S$), or simply $ET = ET_{gw} + ET_s$. We derived uncertainty estimates following the approach of Scott (2010) for rain gauge underestimation ($R_c = 1.05R$), the approach of Twine et al. (2000) for deriving an energy closure-forced evapotranspiration term ($ET_f = ET/\varepsilon$), and the effect of a larger soil depth ($2Z_r$ or 80 cm) on ET_{gw}. It is recognized that the use of ET_f is conditioned on energy balance closure errors (Table 2), but is considered appropriate here for bounding the range of values of ET_{gw}.

We performed a path analysis (PA) to explore the direct and indirect relations between environmental conditions and fluxes. PA is useful when previous correlative information is known between multiple variables (e.g., Huxman et al., 2003; Monson et al., 2005; Li et al., 2017). The standardized path coefficient (β) was used to quantify the effect size of one variable on another (Shao et al., 2016). Our tests were developed to explore the effect of soil and meteorological variables on the daily values of ET, NEE, R_{eco}, and GPP based on prior studies using this methodology (Hui et al., 2003; Huxman et al., 2003; Saito et al., 2009; Wang et al., 2016). The approach included the direct

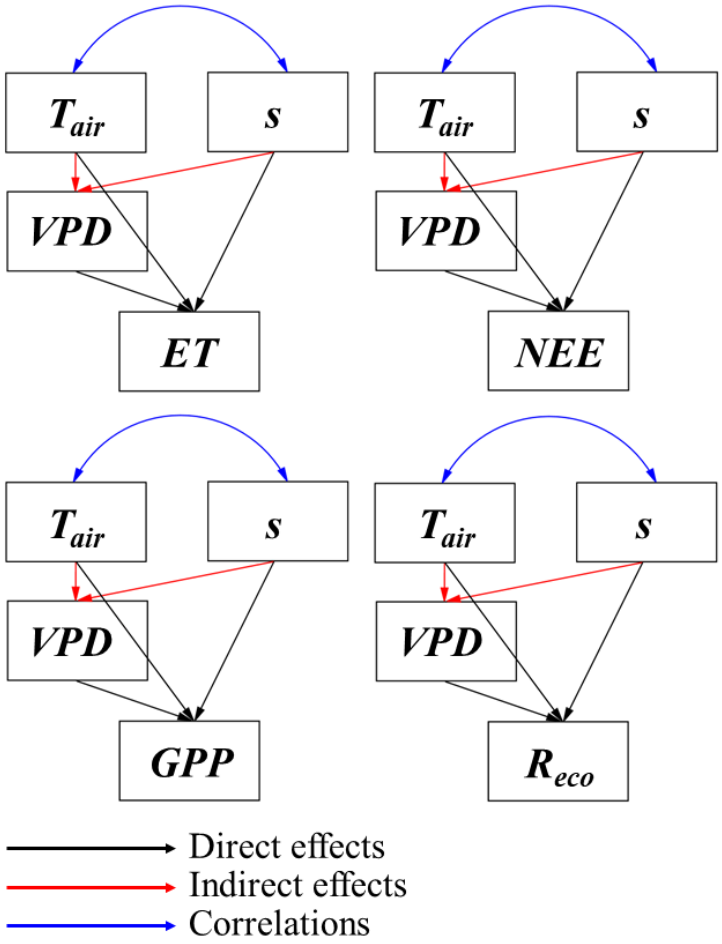

Figure 3.3: Path analysis scheme used to explore relations between environmental conditions (T_{air}, *VPD*, and *s*) and *ET* and carbon fluxes (*NEE*, *GPP*, and R_{eco}).

effects of T_{air}, *VPD*, and *s* on the fluxes, the indirect effects of T_{air} and *s* on *VPD*, and the correlations between T_{air} and *s*, as shown in Figure 3.3. Despite significant correlations, we excluded testing the direct effects of a soil or meteorological variable on another (e.g., *s* direct effect on T_{air}) to focus on how the soil and microclimatic conditions at each site influenced the fluxes. An ANOVA was performed to test the statistical significance of the regressions in the PA. All statistical analyses were performed using SPSS Statistics 26.

Results

Rainfall and Vegetation Seasonality

As a first step, we analyzed the seasonal variation of rainfall and vegetation greenness during 2017 in relation to the long-term behavior from CONAGUA and MODIS data. Notably, the total summer *R* were similar at all EC sites (276, 261, and 258 mm for SS, RM, and OS, respectively), while greater variability (329 ± 114 mm) was found across the rain gauge network (Table 3.1). The EC sites had a similar number of rainfall events of a particular size, as shown in Table 3.3. At OS, however, more precipitation occurred during large events ($R > 25$ mm d^{-1}). Overall, these differences can be considered small given the large spatial variations in rainfall in the network. To illustrate this, Figure 4 presents the monthly rainfall (*R*) during the summer of 2017 in comparison to the long-term data. At the campaign rain gauges, the month of July in 2017 had considerably more rainfall than the long-term average (132% and 162%), while rainfall in August and September of 2017 were below average (both 45%). As a result, vegetation greening in 2017 exhibited anomalous behavior with respect to the long-term average, as shown using *NDVI* for the EC sites and for the areas occupied by their respective ecosystems in Figure 3.4. We note that greening in 2017 occurred earlier than average (in July) at all EC sites, with a more pronounced effect at SS and RM. Similarly, the early demise of the NAM (i.e., below average rainfall in August and September) led to an earlier onset of dormancy relative to the long-term trend. In the case of OS, the ecosystem showed a slightly above average greening during most of the NAM season, despite the lower monthly *R* during August and September.

Table 3.3: Comparison of daily rainfall event sizes during sampling period at each site.

Rainfall Event Size	**SS**		**RM**		**OS**	
	Days	**% *R***	**Days**	**% *R***	**Days**	**% *R***
$R = 0$ mm d^{-1}	82	0	90	0	95	0
0 mm $d^{-1} < R \leq 5$ mm d^{-1}	23	12.20	33	18.24	35	15.75
5 mm $d^{-1} < R \leq 15$ mm d^{-1}	10	32.17	3	8.93	5	18.15
15 mm $d^{-1} < R \leq 25$ mm d^{-1}	3	19.83	5	37.90	0	0.00
$R > 25$ mm d^{-1}	3	35.80	3	34.92	3	66.10
All Events	121	100	134	100	138	100

The vegetation response at the EC sites was consistent with the variability across similar vegetation types in the region during 2017, as shown in Figs. 3.4b-d. At SS, the ecosystem average was higher than the EC site, likely due to the spatial variation of rainfall in the large extent of subtropical scrublands. To explore this further, we created *NDVI* maps for 2017 and compared these to long-term averaged conditions based on *NDVI* difference maps (2017 minus 2002-2018) as shown in Figure 3.5. During May and June, *NDVI* values were low, except in high elevation sites, while differences with the long-term average conditions were small. In July, a large increase in *NDVI* occurs in response to the NAM onset (note the 8-day rainfall totals from 12 to 166 mm). Given the above average rainfall, vegetation greening in July 2017 for RM and SS was greater than the long-term average (123% and 117%), while OS was similar to the long-term average. In August, an initial decrease of *NDVI* occurs in subtropical scrublands in southern areas and then spreads during September to all low elevations. As compared to the long-term average, these two months have lower *NDVI* for RM and SS (90% and 86%), indicating a more rapid senescence during 2017, except at higher elevations (OS) where there is more persistent greenness.

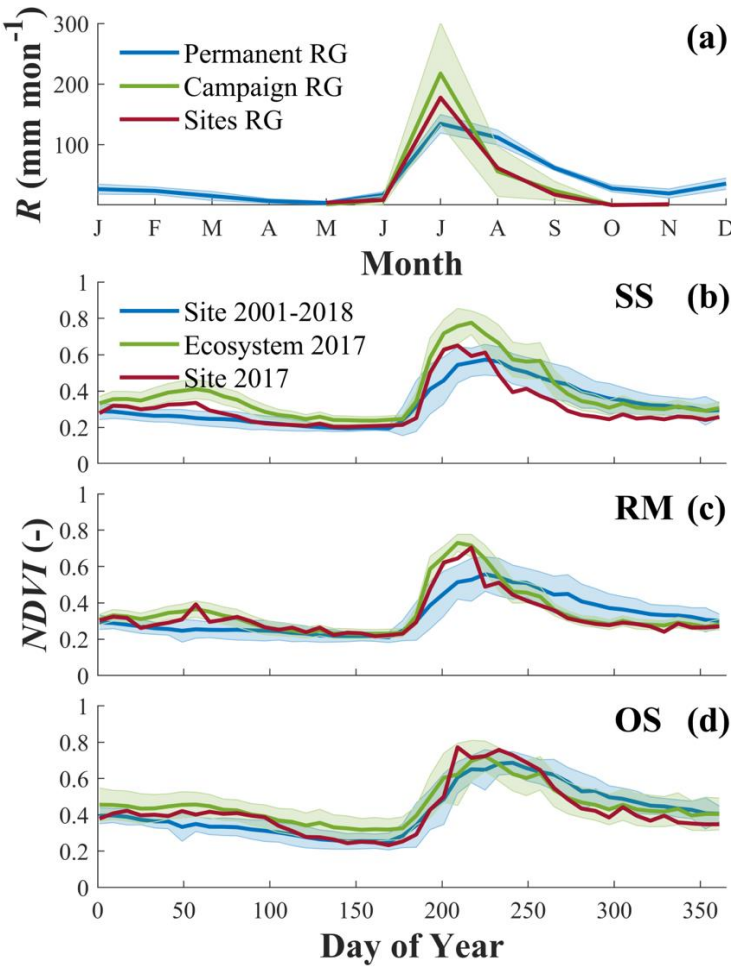

Figure 3.4: (a) Monthly *R* at EC sites ('Sites RG') and campaign rain gauge network ('Campaign RG', with average and ±1 temporal standard deviation) in comparison to long-term monthly *R* at permanent rain gauges ('Permanent RG', with average and ±1 temporal standard deviation). (b-d) Monthly *NDVI* from 2017 at the three sites ('Site 2017'), the long-term *NDVI* at sites ('Site 2002-2018', with average and ±1 standard deviation), and the ecosystem average *NDVI* for 2017 ('Ecosystem 2017', with average and ±1 spatial standard deviation).

Daily Variations in Meteorological Conditions

Figure 3.6 presents daily meteorological and soil variables at the three EC sites, while Table 3.4 presents averages over stages II, III, and IV, selected to focus on monsoon conditions. Storm events generally led to a decrease in T_{air} and an increase in *RH* at the three sites, in particular during stage II (early monsoon). As expected, the

higher elevation OS site (average T_{air} of 23.85 °C) was cooler than the lower elevation SS and RM sites (average T_{air} of 28.4 and 27.32 °C, $p < 0.01$). Daily-average values of *RH* and *VPD* showed differences that are statistically significant between SS and the other sites (Table 3.4). Even though gaps were present in R_n values at SS and RM, a similar daily variability of R_n was noted ate the three sites. Daily R_n were somewhat lower at SS and RM (average of 138 and 143 W m^{-2}) than at OS (average of 167.5 W m^{-2}). *s* exhibited a strong seasonality reflecting the overall wetting and drying during the NAM. Note that SS exhibited more rapidly depleted soil water as compared to RM and OS, an indication of differences in soil water losses by the ecosystems, including evapotranspiration.

Response of Water-Energy-Carbon Fluxes

We present the total seasonal values of *R*, *ET*, and *NEE* in Table 3.4. While *R* was similar at the sites, *ET* varied considerably, suggesting that different water use strategies existed across the sites. Total *NEE* during the season also varied substantially. SS and RM behaved as net carbon sources, while the OS site was a net carbon sink. A gradient was noted across the sites, with *GPP* increasing in the order of SS, RM, and OS and exhibiting statistical differences, while R_{eco} was statistically similar at RM and OS, but lower and statistically different at SS.

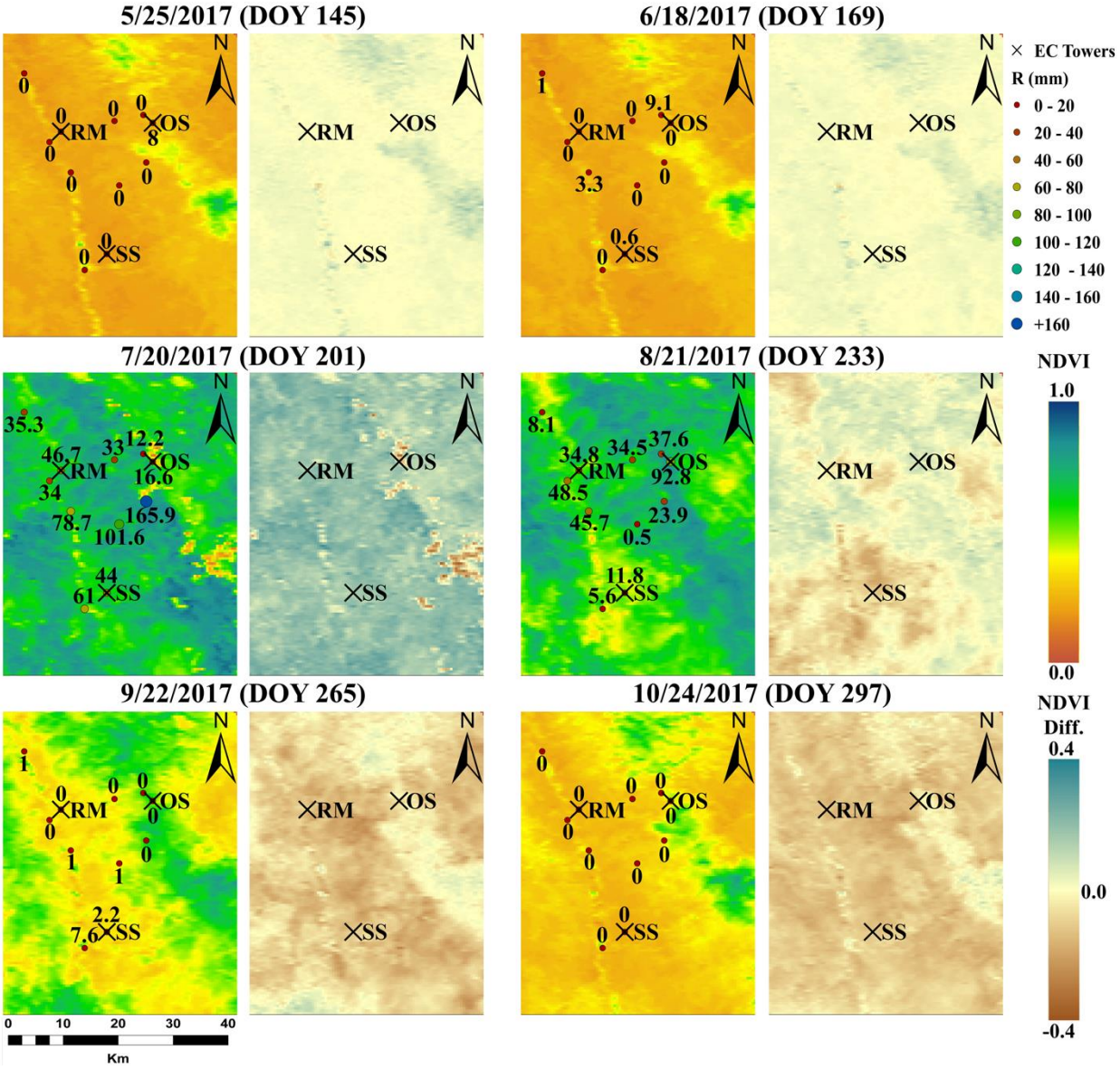

Figure 3.5: Variation of *NDVI* from May 25, 2017 to October 24, 2017. For each date, the image pair shows MODIS *NDVI* 8-day composite values (left) and the difference between each image and the MODIS long-term *NDVI* average during 2002 to 2018 (right). Circles represent the sum of *R* during the 8-day period with values labeled using numbers.

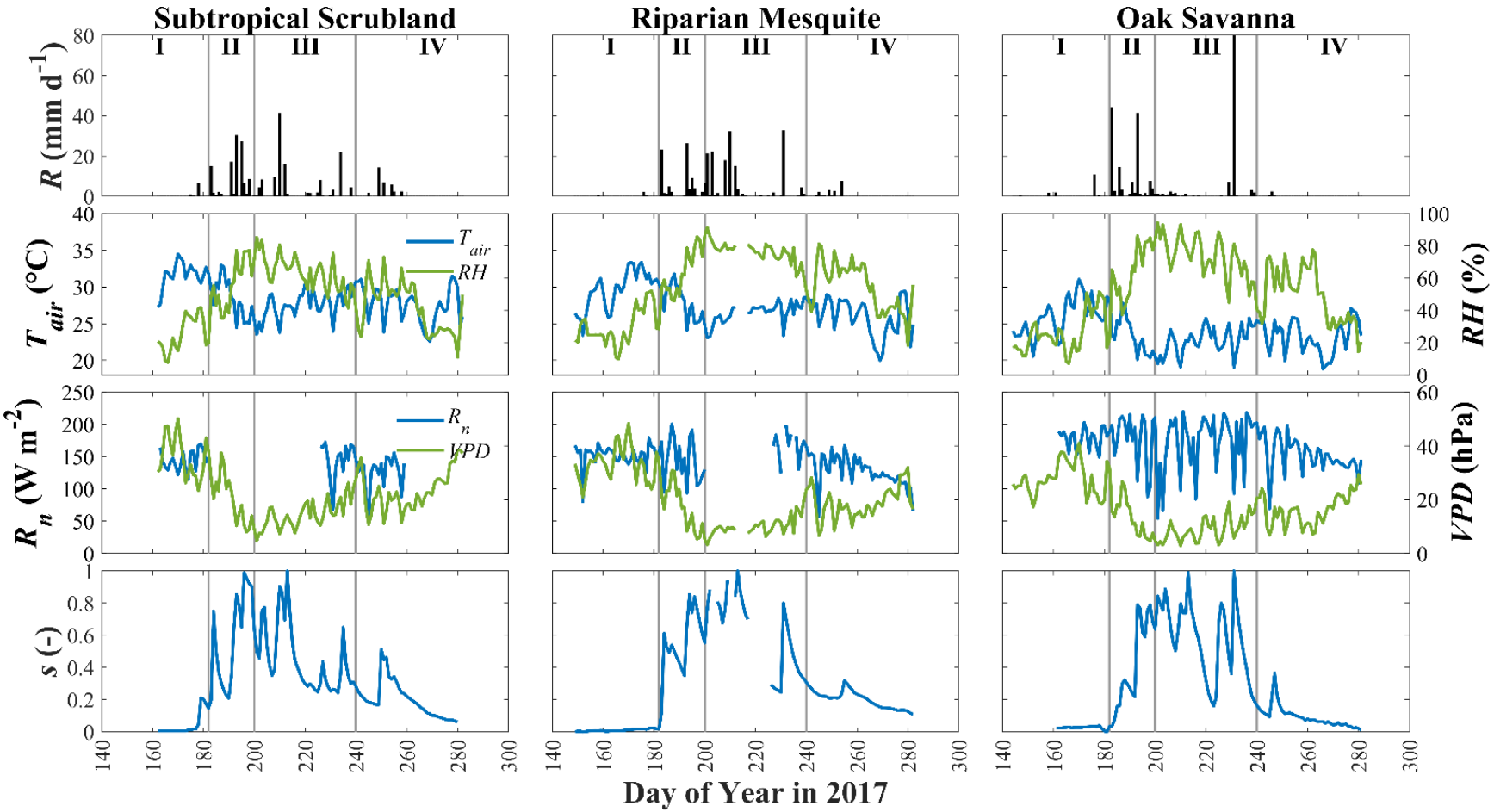

Figure 3.6: Daily variations in rainfall (R), air temperature (T_{air}), relative humidity (RH), net radiation (R_n), vapor pressure deficit (VPD), and relative water content (s) at the three study sites in the NAM stages of: (I) pre-monsoon, (II) early monsoon, (III) late monsoon, and (IV) post-monsoon.

Table 3.4: Comparison of seasonal values of meteorological variables, turbulent fluxes, water budget, and carbon budget across the three sites for stages II, III, and IV. The use of superscript [a], [b] and [c] for SS, RM, and OS, respectively, indicate groupings with no statistically significant differences, if used together.

	SS[a]	**RM[b]**	**OS[c]**
Meteorological Variables			
T_{air} (°C)	28.40[a]	27.32[b]	23.85[c]
RH (%)	48.27[a]	55.24[bc]	51.65[bc]
VPD (hPa)	22.15[a]	19.95[bc]	17.00[bc]
Turbulent Fluxes (W m^{-2})			
λET	54.65[a]	60.85[bc]	62.91[bc]
H	83.80[a]	66.68[b]	50.53[c]
Water Budget (mm)			
ET	228.54[a]	273.40[bc]	300.05[bc]
ET_f	244.48[ab]	319.96[abc]	406.73[bc]
R	276.00[abc]	260.87[abc]	257.80[abc]
$Z_r \Delta S$	0.21[ac]	5.28[ab]	-0.50[ac]
Carbon Budget (g CO$_2$ m^{-2})			
NEE	9.56[ab]	151.66[ab]	-299.25[c]
R_{eco}	1601.00[a]	2712.31[bc]	2753.21[bc]
GPP	1591.46[a]	2560.57[b]	3052.42[c]

Figure 3.7 presents daily totals of *R* and *NEE*, daily averages of λET and *H*, and 8-day composite values of *NDVI*. During the pre-monsoon (I), values of λET, *NEE*, R_{eco}, *GPP*, and *NDVI* were close to zero due to vegetation dormancy, while maximum values of *H* occurred. In the early monsoon (II), rainfall and increased soil water content led to an increase in λET followed by a decrease in *H*, and a positive *NEE* resulting from an increase of R_{eco} with the first storms. Fluxes in stage II were similar to previous years at SS and OS, such that initially 2017 had a behavior similar to average conditions. In the late monsoon (III), maximum *NDVI* at each EC site resulted in persistently high λET and low *H*, while *GPP* was higher than R_{eco}, leading to CO_2 uptake, with values of *NEE* of

about -20 and -14 g CO_2 m^{-2} d^{-1} for SS and OS. At RM, periods of CO_2 uptake and release occurred with a similar frequency, leading to *NEE* near zero.

As *NDVI* decreased in the post-monsoon (IV), changes were noted in λET, *H*, and *NEE*, with larger variations between the ecosystems. Recall that below average rainfall and *NDVI* were noted for August and September. As a result, *NEE* values close to zero were measured at SS, which was more carbon neutral than the long-term average conditions (2008-2012), due to the sudden increase of R_{eco} from a weak reactivation from storm events in the late monsoon (III). In contrast, the OS site remained active throughout stage IV, with above average *NDVI* and higher *NEE* values as compared to previous years (2008-2014). *GPP* and R_{eco} showed a clear distinction among the sites in the post-monsoon that provide insight into the plant water use strategies and the phenological differences between the sites. At SS, there was a marked decrease of *GPP* and R_{eco} in September, in response to the end of rainfall. In contrast, RM and OS were able to sustain levels of *GPP* and R_{eco} for longer periods, possibly due to additional water sources, with a more notable extension at OS, where *GPP* was maintained for a longer period and had higher values than R_{eco}, leading to positive *NEE*. The variations of the carbon flux components highlighted clearly the ecosystem differences as compared to prior work that relied solely on *ET* and *NDVI*.

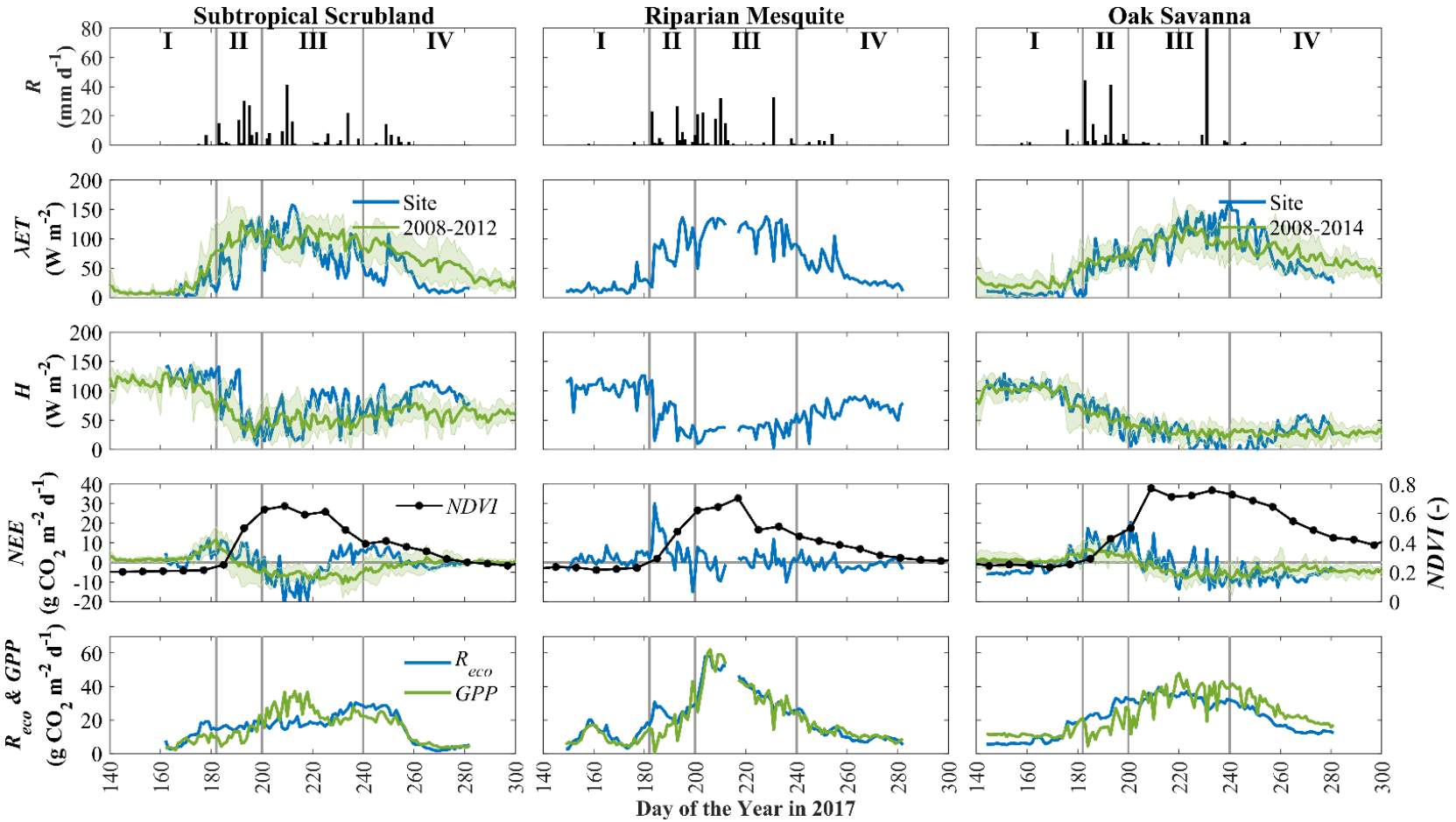

Figure 3.7: Daily variations of rainfall (*R*), sensible heat flux (*H*), latent heat flux (λ*ET*), net ecosystem exchange (*NEE*), ecosystem respiration (R_{eco}), gross primary productivity (*GPP*), and normalized difference vegetation index (*NDVI*) at the three study sites and during the NAM stages of: (I) pre-monsoon, (II) early monsoon, (III) late monsoon, and (IV) post-monsoon. Solid lines are values obtained during 2017 (labeled 'Site') and solid lines with envelopes are daily averages of previous years with ±1 temporal standard deviation (at SS and OS only).

Landscape Controls along Ecosystem Gradient

Next, we quantified the landscape controls related to elevation-induced soil and microclimate conditions for stages II, III, and IV using the path analysis (Table 3.5). Since T_{air} varied significantly across the sites, it has a significant direct contribution to *ET*, R_{eco}, and *GPP*, with increases in these fluxes at higher air temperatures. *NEE* did not exhibit a significant dependence on T_{air} but showed a positive relation at all sites. While *VPD* could be considered a critical factor, significant differentiation was only noted between SS and the other sites (Table 4). Higher *VPD* was negatively correlated with *ET*, R_{eco}, and *GPP* in the three ecosystems, generally at significant levels. However, *NEE* had a limited dependence on *VPD*. The RM sites showed a positive and significant effect, but the SS and OS sites exhibited no significant effect of *VPD* on *NEE*. This implies that the seasonality noted in *VPD* only impacts *NEE* at RM, whereas the other sites have temporal variations that did not resemble *VPD*. Finally, soil water content had a significant direct and positive effect on *ET*. However, the strength and significance of this effect decreased from SS, to RM, and to OS, indicating less dependence on shallow soil water for evapotranspiration. Furthermore, *NEE* dependence on *s* varied among the sites. For SS, there was no significant direct effect of *s* on *NEE*, while the RM and OS sites showed similar positive effects such that higher *s* led to a higher *NEE*. Underlying these variations in *NEE* are differences in the direct effect of *s* on R_{eco} and *GPP* across the ecosystem gradient.

To assess the effect of groundwater access, we present values of *EI* and ET_{gw}, as well as their uncertainty estimates, and *IWUE* for stages II, III, and IV in Table 3.6. *EI* showed a clear difference along the gradient. SS had values of *EI* less than unity, such that the

ecosystem had lower *ET* than *R*, even when accounting for measurement uncertainty. At both RM and OS, *EI* was equal to or greater than 1, indicating that a water source in addition to *R* was used. This is consistent with positive ET_{gw} estimates for all cases at RM and OS, including those with $2Z_r$. The robustness of positive ET_{gw} to the various sources of uncertainty suggest that RM and OS could have consumed water from deeper soil layers. Potential differences in water sources also impacted water use efficiency as measured by *IWUE*. During the early monsoon (II), similar *IWUE* values were noted along the ecosystem gradient due to rainfall availability and low atmospheric water demand. By stage IV, *IWUE* displays clear differences that could be related to access to groundwater since SS showed the highest *IWUE* and had low soil water during the post-monsoon. Since the elevation at SS and RM was similar, but *IWUE* in stage IV exhibit large differences with less efficiency at RM, soil and microclimate conditions have a smaller effect on water use efficiency as compared to groundwater access.

Discussion

Water-Energy-Carbon Fluxes along Ecosystem Gradient

Prior efforts have characterized ecosystem responses to seasonal NAM rainfall using remotely-sensed vegetation indices and evapotranspiration measurements (e.g., Forzieri et al., 2011; Méndez-Barroso et al., 2014). While useful, these evaluations have limitations in their ability to distinguish the relationship between water and carbon fluxes which are essential to identifying water use patterns in arid and semiarid regions (e.g., Barron-Gafford et al., 2013; Scott et al., 2014). By inspecting conditions along an ecosystem gradient, we identified the variations of microclimatic conditions, access to

Table 3.5: Direct and indirect effects of soil and meteorological variables on *ET*, *NEE*, R_{eco}, and *GPP* from the PA standardized path coefficient (β) for stages II, III, and IV. Correlation between soil and meteorological variables also tested. * indicates a statistical significance at $p < 0.01$, $^{+}$ at $p < 0.05$, and ^{X} at $p < 0.1$.

		T_{air}			s		VPD
	Direct	**Total**	**Correlation**	**Direct**	**Total**	**Correlation**	**Direct**
SS							
			-		-	-	
NEE	0.106	0.200		-0.066	0.156		0.187
ET	0.272*	0.099	-	0.761*	0.927	-	-0.346*
R_{eco}	0.643*	0.282	-	0.074	0.421	-	-0.723*
GPP	0.483*	0.098	-	0.115	0.485	-	-0.770*
T_{air}	-	-	-	-	-	0.428*	-
s	-	-	0.428*	-	-	-	-
			-	-	-	-	
VPD	0.500	-		0.480*			-
RM							
NEE	0.084	0.303	-	0.574*	0.265	-	0.509*
ET	0.307*	0.124	-	0.627*	0.886	-	-0.426*
R_{eco}	0.171*	0.140	-	0.838*	0.882	-	-0.073
GPP	0.142^{X}	0.021	-	0.582*	0.753	-	-0.282^{+}
T_{air}	-	-	-	-	-	-0.330*	-
s	-	-	-0.330*	-	-	-	-
			-	-	-	-	
VPD	0.430*	-		0.608*			-
OS							
NEE	0.032	0.067	-	0.473*	0.500	-	0.064
			-		-	-	
ET	0.394*	-0.016		0.171^{X}	0.145		-0.745*
R_{eco}	0.448*	0.021	-	0.430*	0.101	-	-0.776*
			-		-	-	
GPP	0.403*	-0.039		0.025	0.315		-0.803*
T_{air}	-	-	-	-	-	-0.480*	-
s	-	-	-0.480*	-	-	-	-
VPD	0.550*	-	-	0.424	-	-	-

Table 3.6: Seasonal *EI*, ET_{gw}, and values of *IWUE* for stages II, III, and IV in the three ecosystems. *EI* and ET_{gw} include uncertainty estimates using R_c and ET_f.

	SS	**RM**	**OS**
***EI* (-)**			
ET / R	0.83	1.05	1.16
ET / R_c	0.79	1.00	1.11
ET_f / R	0.89	1.23	1.58
ET_f / R_c	0.84	1.17	1.50
$\boldsymbol{ET_{gw}}$ **(mm)**			
$ET_{gw} = ET - R - Z_r\Delta S$	-47.25	17.81	41.75
$ET_{gw} = ET - R_c - Z_r\Delta S$	-61.05	4.77	28.86
$ET_{gw} = ET_f - R - Z_r\Delta S$	-31.31	64.37	148.42
$ET_{gw} = ET_f - R_c - Z_r\Delta S$	-45.11	51.32	135.53
$ET_{gw} = ET - R - 2Z_r\Delta S$	-47.05	23.09	41.24
$ET_{gw} = ET_f - R_c - 2Z_r\Delta S$	-44.91	56.61	135.03
IWUE **(g CO_2 hPa mm^{-1})**			
II	85.06	98.95	97.34
III	120.62	105.18	86.49
IV	247.24	165.47	170.51

groundwater, intensive or extensive phenology, and seasonal carbon fluxes under similar rainfall conditions. Figure 3.8 presents a summary for the sampled gradient along which both T_{air} and *VPD* decrease (from left to right), though access to groundwater varies with landscape position. Net seasonal carbon budgets along the gradient also depend on the relative growth rates of *GPP* and R_{eco}. Subtropical scrublands appear dependent on shallow soil water from rainfall events due to their placement in alluvial fans that have deep groundwater. Riparian mesquite and oak savanna sites seem to have access to subsurface water stored in an alluvial aquifer and within a fractured rock aquifer, respectively. The lack of groundwater in subtropical scrublands leads to a high dependence on seasonal rainfall variability, leading to an intensive phenological pattern,

as well as a dependence on near surface soil and microclimatic conditions (Verduzco et al., 2018), and a near neutral carbon budget (similar R_{eco} and *GPP*). Access to groundwater at the riparian site does not appear sufficient to convert the riparian mesquite into a net carbon sink despite the high *ET*, as R_{eco} was greater than *GPP*, consistent with values reported in other riparian mesquites (Scott et al., 2014; Yepez et al., 2007). This is linked to the intensive phenological traits of the riparian mesquite trees. The oak savanna site with access to groundwater and extensive greening is influenced to a lower extent by seasonal rainfall variability and is capable of supporting *GPP* at higher rates than R_{eco}, in particular for the late-monsoon stage, when it has a supplementary water source. Variations in microclimatic conditions had a small effect on *NEE* across the gradient, despite influencing *GPP* and R_{eco}, except at the riparian site where high T_{air}, *VPD*, and supplemental water co-occur.

Water Efficiency and Groundwater Contributions

For the conditions of the field campaign, access to groundwater appears to be the more important landscape control on evapotranspiration, though soil and microclimatic conditions modulate the seasonal carbon budget when plants can access deeper subsurface water. For ecosystems dependent on recent rainfall, such as subtropical scrublands, a significant water limitation is present after the end of the NAM, leading to a higher water use efficiency, in particular for the late and post-monsoon stages. A threshold in access to groundwater appears to be required for there to be a transition from intensive to extensive water use strategies. For instance, the riparian site exhibits the phenological traits of intensive water users, but has a much lower water use efficiency

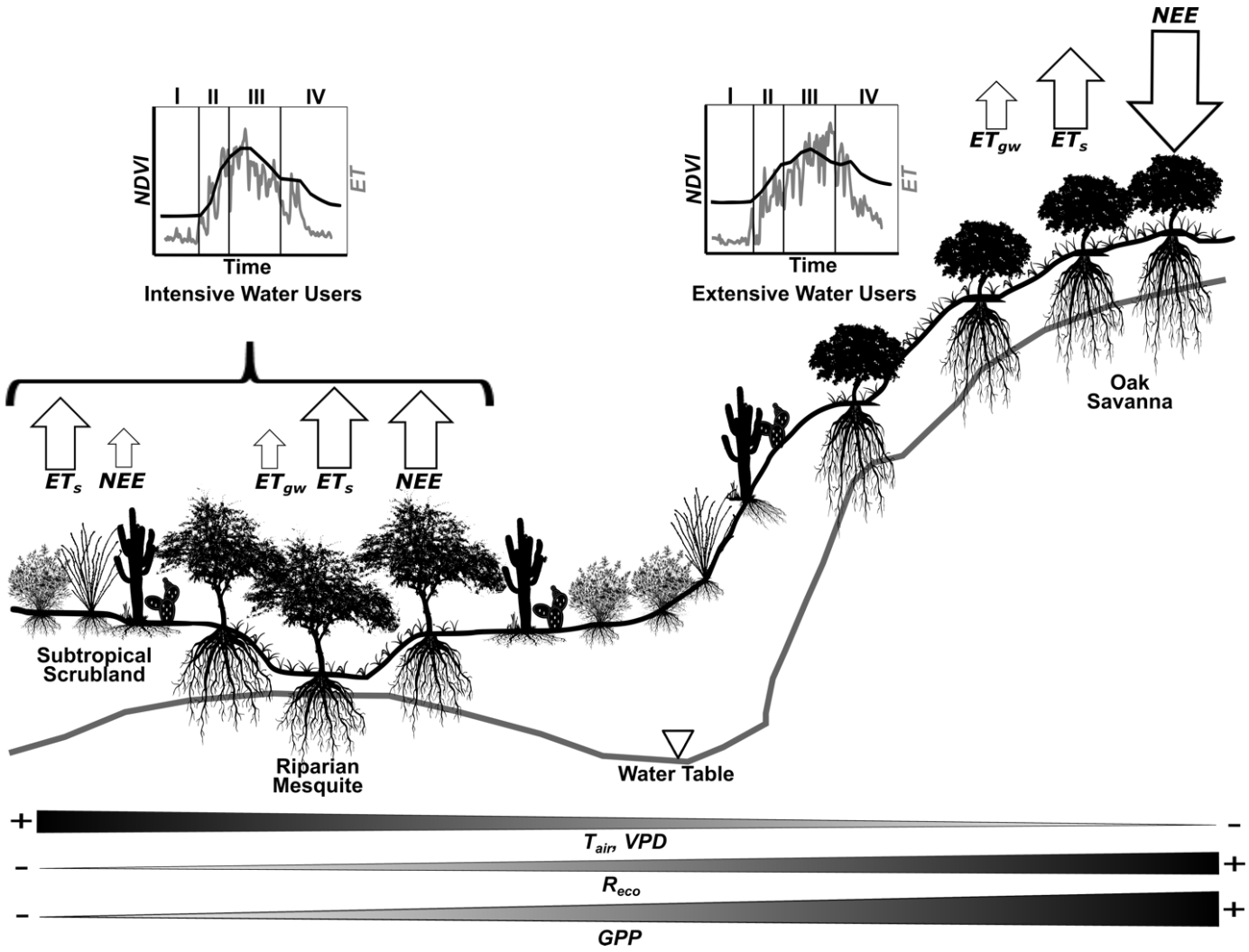

Figure 3.8: Schematic of the effect of landscape controls, including microclimatic conditions and access to groundwater, on water-energy-carbon fluxes during the North American monsoon for intensive and extensive water use strategies. Schematic is not to scale.

due to groundwater access, suggesting that the landscape location did not cross the threshold of available subsurface water. As a result, we infer that a more stable groundwater source is present in the fractured rock of the mountain block such that OS is the only site with plausibly reliable groundwater (e.g., Paco et al., 2009; Rodríguez-Robles et al., 2017), as compared to the lower elevation alluvial aquifers (RM) which are sporadically recharged by ephemeral flooding (e.g., Goodrich et al., 2004; Wilson and Guan, 2004). The riparian mesquite site seems to have intermediate access to groundwater near the ephemeral channel likely after sequences of late monsoon (stage III) storms that could induce streamflow, in contrast to Scott et al. (2014) who found more permanent access near a perennial river.

Hydrologic Dynamics and Their Link to Carbon Fluxes

Groundwater dependence at riparian and mountain sites link their ecosystem processes to hydrologic dynamics including water table fluctuations, lateral subsurface transport, and episodic recharge (e.g., Laio et al., 2009; Martinet et al., 2009; Eamus et al., 2015). Additional measurements at these sites, including streamflow measurements, sampling of subsurface water levels through piezometers, and water sampling for isotopic analysis, are needed to confirm the hydrologic dynamics identified in this study. At sites with potential groundwater access, evapotranspiration can extend beyond the end of the rainy season, but seasonal carbon budgets depend on the soil and microclimate conditions as well as the plant phenological traits. In contrast, subtropical scrublands exhibit evapotranspiration primarily during the rainfall period and showed a nearly neutral seasonal carbon budget for the sampled period. Prior efforts to quantify differences between intensive and extensive water use strategies in the NAM region relied only upon

evapotranspiration measurements or remotely-sensed vegetation indices since phenological traits such as the timing of leaf senescence are linked to water use (e.g., Forzieri et al., 2011; Méndez-Barroso et al., 2014). As shown here, the seasonal carbon fluxes provide an important differentiation among sites, in particular that microclimatic conditions and plant water use strategies modulate carbon exchange patterns at sites with access to groundwater. While vegetation indices can be used to distinguish between intensive and extensive greening and provide a long-term context, these observations have limitations in identifying the net seasonal carbon budget across different sites. Additional sampling periods would be needed to identify the inter-annual variability of the carbon budget which has been shown to fluctuate from a net carbon source to a net carbon sink in arid and semiarid ecosystems (e.g., Biederman et al., 2017).

Conclusions

In this study, we analyzed the water-energy-carbon fluxes during the North American monsoon of 2017 in three ecosystems of northwestern México. The analysis consisted of an assessment of the field campaign conditions with respect to rainfall data, remotely-sensed vegetation, and flux measurements in the MexFlux database from previous years, which allow inferences to be made across a larger region and across other time periods. We conducted daily analyses during various NAM stages and used a set of indices to determine relations between water and carbon fluxes. We summarize the study conclusions as follows:

1. Rainfall and its subsequent vegetation response during the 2017 NAM season had a similar onset to long-term datasets but exhibited more (less) pronounced activity in July (August and September), leading to a shorter duration of the NAM. As a

consequence, the water-energy-carbon fluxes showed more significant exchanges in the early part of the NAM season and lower activity in the later part, which primarily impacted the lower elevation ecosystem (SS) that depended solely on shallow soil water. Nevertheless, even the high elevation ecosystem with access to groundwater (OS) was influenced to a minor extent by the seasonal rainfall variability.

2. During the field campaign, the ecosystems had a similar rainfall amount, but differences in access to subsurface water appear to have led to divergent patterns of water and carbon fluxes. Over the study period, low elevation ecosystems with intensive phenological traits were net sources of CO_2 (9.56 and 151.66 g CO_2 m^{-2} at SS and RM), while the high elevation ecosystem (OS) with an extensive plant strategy acted as a net carbon sink of -299.25 g CO_2 m^{-2}. This suggest that soil (*s*) and microclimatic (T_{air}, *VPD*) conditions modulated the seasonal carbon budget through differential effects on ecosystem respiration and gross primary productivity. In addition, extended leaf phenology at OS allowed for continued productivity during the post-monsoon stage when ecosystem respiration became more subdued with decreases in *s* and T_{air}.

3. Elevation-induced soil and microclimate conditions varied in their influence on water-energy-carbon fluxes at the sites, as revealed by the path analysis. As air temperature increased at all sites, we noted a statistically significant increase in evapotranspiration and carbon flux components, but a weak influence on net ecosystem exchange. The effect of *VPD* on *NEE* was only statistically significant at the riparian mesquite site, where there was co-occurrence of high temperature,

atmospheric demand, and supplemental water sources. Higher soil water content was positively correlated to evapotranspiration at all sites, while CO_2 release (higher R_{eco} and *NEE*) was promoted with higher *s* only for sites with access to groundwater where vegetation and microbial activity was likely to be promoted.

4. Estimates of groundwater used for evapotranspiration varied significantly among the ecosystems such that deeper sources were likely consumed at the riparian and mountain settings. This was accompanied by differences in water use efficiency, with subtropical scrublands having higher efficiency under water stressed conditions. In contrast, groundwater access allows riparian mesquites and oak savannas to have lower efficiencies at the end of the rainy season. Inferences from the water-energy-carbon fluxes indicate that a more stable groundwater source is likely present at the mountain block site as compared to the site in an alluvial aquifer.

Despite the long-term context provided, the study outcomes remain conditioned on a single NAM season, suggesting that additional field monitoring is warranted across the seasonally dry ecosystem gradient, in particular given the high inter-annual variability of the NAM (e.g., Gutzler, 2004; Forzieri et al., 2011). Verduzco et al. (2015), for instance, identified large inter-annual differences in net seasonal carbon budgets due to variations in NAM rainfall amounts as well as the effects of the preceding winter. As such, we could expect variations in the relative roles of access to groundwater and microclimatic conditions driven by changes in rainfall availability. While previous MexFlux datasets are helpful as shown here, these do not contain the riparian mesquite woodland that

serves as an important intermediate site, with both access to groundwater and the soil and microclimatic conditions of low elevation areas.

Future work should consider the permanent installation of water-energy-carbon flux sites across an ecosystem gradient that exposes differences in landscape controls in a structured manner, including a mountain site without access to groundwater to serve as an additional comparative location. Finding sites that isolate a particular landscape control, for instance an elevation effect, without the concomitant presence of another control, for instance access to groundwater, is difficult. However, such EC sites would potentially reveal if groundwater access provides a stabilizing role to the seasonal and annual water and carbon budgets in the midst of the high inter-annual rainfall variability as well as the legacy effects previously noted between winter and summer seasons (e.g., Verduzco et al., 2015; Delgado-Balbuena et al., 2019). This is particularly relevant given anticipated changes in seasonal rainfall due to climate change in the NAM region (e.g., Seager et al., 2007; Cook and Seager, 2013; Pascale et al., 2019). Under scenarios of lower rainfall amounts delivered as more extreme events, we anticipate that ecosystems with access to groundwater will rely more heavily on this source to sustain evapotranspiration and carbon uptake during the NAM. In contrast, ecosystems with intensive water use strategies will require adjustments via higher water use efficiency to avoid a reorganization of plant assemblages.

CHAPTER IV

SEASONAL VARIATION OF WATER-CARBON DYNAMICS IN A DRYLAND ECOSYSTEM

Introduction

In arid and semiarid landscapes, primary productivity is controlled by soil water availability (e.g., Noy-Meir, 1973; Reynolds et al., 2000; 2004; Scott et al., 2006). Rainfall has been commonly used as a proxy of water availability to determine productivity using annual values (Sala et al, 1998; Huxman et al., 2004; Ogle and Reynolds, 2004; Thomey et al., 2011; Hsu et al., 2012; Sala et al., 2012; Scott et al., 2015; Biederman et al., 2016; Flanagan and Flanagan, 2018; Maurer et al., 2020). Nevertheless, several studies have found weak relations between annual rainfall and productivity (Jia et al., 2016; Biederman et al., 2018; Ukkola et al., 2021) and have suggested that seasonal variations may have a greater importance in those arid and semiarid ecosystems with single or multiple rainy periods within a year (e.g., Méndez-Barroso et al., 2009; Jia et al., 2016; Baldocchi et al., 2018; Liu et al., 2020). As a result, further research is warranted on the seasonal patterns of ecosystem productivity and its link to soil water availability.

Biogeochemical processes in arid and semiarid ecosystems are closely tied to the hydrological cycle (e.g., Huxman et al., 2004; Scott et al., 2006; Yahdjian et al., 2006; Williams et al., 2006; Lohse et al., 2009; Yahdjian et al., 2011). While rainfall is a useful proxy for this coupling, the hydrological partitioning or the water balance within a landscape constrains the availability and use of water by vegetation (e.g., Scott et al.,

2015; Biederman et al., 2016; Jia et al., 2016). For instance, evapotranspiration and shallow soil moisture have been recognized as improved indicators of ecosystem water use (e.g., Kurc and Small, 2004, 2007; Yépez et al., 2007; Vivoni et al., 2008; Biederman et al., 2016, 2017; Scott and Biederman, 2017). Biederman et al. (2018) showed that arid and semiarid shrublands in the North American deserts had stronger relations between productivity and evapotranspiration than similar analyses using rainfall. Less attention has been placed on how water storage below the plant rooting zone can modulate water availability to plants and overall ecosystem productivity and water use.

Water input in most ecosystems of the North American deserts occurs during the winter and summer seasons (Sponseller et al., 2012). This bimodal regime is characterized by high intensity, localized convective storms during the summer, and lower intensity, widespread frontal storms during the winter (Scott et al., 2009; Scott and Biederman, 2019). The seasonal variability of water input and atmospheric conditions generates differences in hydrologic partitioning and can lead to divergent patterns of ecosystem water use and productivity. For instance, during the North American monsoon (Adams and Comrie, 1997), larger rainfall events combined with higher radiation and atmospheric water demand typically will lead to higher water losses through evapotranspiration and runoff (e.g., Vivoni et al., 2010; Méndez-Barroso et al., 2009; Templeton et al., 2014; Pierini et al., 2014; McKenna and Sala, 2018; Pérez-Ruiz et al., 2021). In contrast, the lower intensity precipitation during the winter, when radiation and atmospheric water demands are much lower, typically favor the downward percolation of water into deeper soil layers but may still support ecosystem productivity and water use

within the season (e.g., Wilcox et al., 2006; Anderson-Teixeira et al., 2011; Scott and Biederman, 2019).

Some shrubland ecosystems follow a bimodal productivity regime that is controlled both by the winter and summer seasons. Studies have shown a high ecosystem carbon uptake in the winter season due to the presence of evergreen species or those shrubs with spring leaf-out which have a rooting structure that allows access to deep soil moisture (Huxman et al., 2004; Kurc and Small, 2004; Ogle and Reynolds 2004; Reynolds et al., 2004; Wohlfahrt et al., 2008; Kurc and Benton, 2010; Biederman et al., 2018). Since water storage in deeper layers is influenced by the seasonality of water input and its partitioning, it is important to elucidate the mechanisms of primary productivity in those shrubland ecosystems where a bimodal rainfall regime might lead to carry-over effects between different seasons. Subsurface water storage accessed by deep shrub roots is a mechanism by which water input during the summer seasons can be linked to drier winter periods or subsequent years (e.g., Duniway et al., 2007, 2010; Schwinning, 2010; Schreiner-McGraw and Vivoni, 2017, 2018). Thus, soil water storage legacies or carry-over effects may be an important link between seasons in bimodal regimes where plants can access deep soil water.

In this study, we investigated the seasonal dynamics in hydrological partitioning and its relation to primary productivity in a mixed shrubland of the Chihuahuan Desert using the eddy covariance (EC) method (Baldocchi, 2003). To achieve this, we analyzed seasonal distributions of water balance components and carbon fluxes over a 10-year period. The bimodality of hydrological processes and ecosystem productivity in this dryland ecosystem offered an opportunity to explore the carry-over effects between

seasons and the role played by the gross primary productivity and ecosystem respiration on the net carbon balance. Specifically, we address the following questions: (1) What are the links between net ecosystem production and water availability in the winter and summer seasons?, (2) How do seasonal variations of gross primary productivity and ecosystem respiration affect the overall carbon balance?, and (3) How does the summer season proportion of annual rainfall influence annual net ecosystem production?. In addition, we used the long-term record of coordinated observations to discuss interannual variations in seasonal rainfall and its impact on the seasonal and annual carbon budget.

Methods

Study Site

The study site is a mixed shrubland in the Jornada Experimental Range (JER), ~20 km north of Las Cruces, New México, USA, within the northern portion of the Chihuahuan Desert (Figure 4.1). A small first-order watershed of approximately 4.7 ha was instrumented in 2010 to monitor water and carbon flux components (Templeton et al., 2014; Anderson and Vivoni, 2016; Mascaro and Vivoni, 2016; Schreiner-McGraw et al., 2016, 2017). Local climate is classified as a cold desert (Koppen zone BWk), with an annual average rainfall (R) of 277.9 mm and a mean annual temperature of 17.9 °C during the study period of 2011 to 2020. A bimodal rainfall regime leads to ~65% of annual rainfall during the North American Monsoon (NAM) in July through September (Adams and Comrie, 1997). Climate conditions and the process of woody plant encroachment in the last 150 years (Gibbens et al., 2005) have led to a mixed shrubland consisting of creosote bush (*Larrea tridentata*), honey mesquite (*Prosopis glandulosa* Torr.), mariola (*Parthenium incanum*), tarbush (*Flourensia cernua*), and snakeweed

(*Gutierrezia sarothrae*), as well as the lower presence of several grass species, including bush muhly (*Muhlenbergia porteri*), tobosa grass (*Pleuraphis mutica*), and sand dropseed (*Sporobolus cryptandrus*). A high-resolution terrain and vegetation product (Templeton et al., 2014) indicates that the watershed consists of ~4% grasses, ~30% shrubs, and ~66% bare soil. The study site has sandy-loam soil textures with a high gravel content at the surface, and a petrocalcic horizon at a depth of ~40 cm (Anderson and Vivoni, 2016). The watershed has north-, south- and west-facing hillslopes with modest slopes (0 to 6º), except along the channel and its banks where higher slopes are found (15 to 25°). The main channel of ~0.5 m width has a sandy bottom that allows percolation of runoff generated on hillslopes (Schreiner-McGraw and Vivoni, 2017). More limited vertical infiltration occurs on the hillslopes themselves due to the petrocalcic horizon.

Water balance and carbon fluxes measurements

High frequency measurements of water, energy, and carbon fluxes were obtained using the EC method (Baldocchi, 2003). Fluxes included net ecosystem production (*NEP*), latent heat flux (λET), and sensible heat flux (H). The EC system consisted of an infrared gas analyzer (IRGA) to measure H_2O and CO_2 concentrations and a sonic anemometer to measure wind components. The IRGA used was a LI-7500 (Li-COR Biosciences, Lincoln, Nebraska), while the sonic anemometer was a CSAT-3 (Campbell Scientific, Logan, Utah). The EC system was installed at 7.1 meters above the ground, at an elevation of 1469 m and the ecosystem had an average canopy height of 1 meter (Templeton et al., 2014). Fluxes were calculated at 30-min intervals with EddyPro® 7.0.6. Quality control and processing followed the standards of the EC community as described in Pérez-Ruiz et al. (2021). As a result, the EC site is

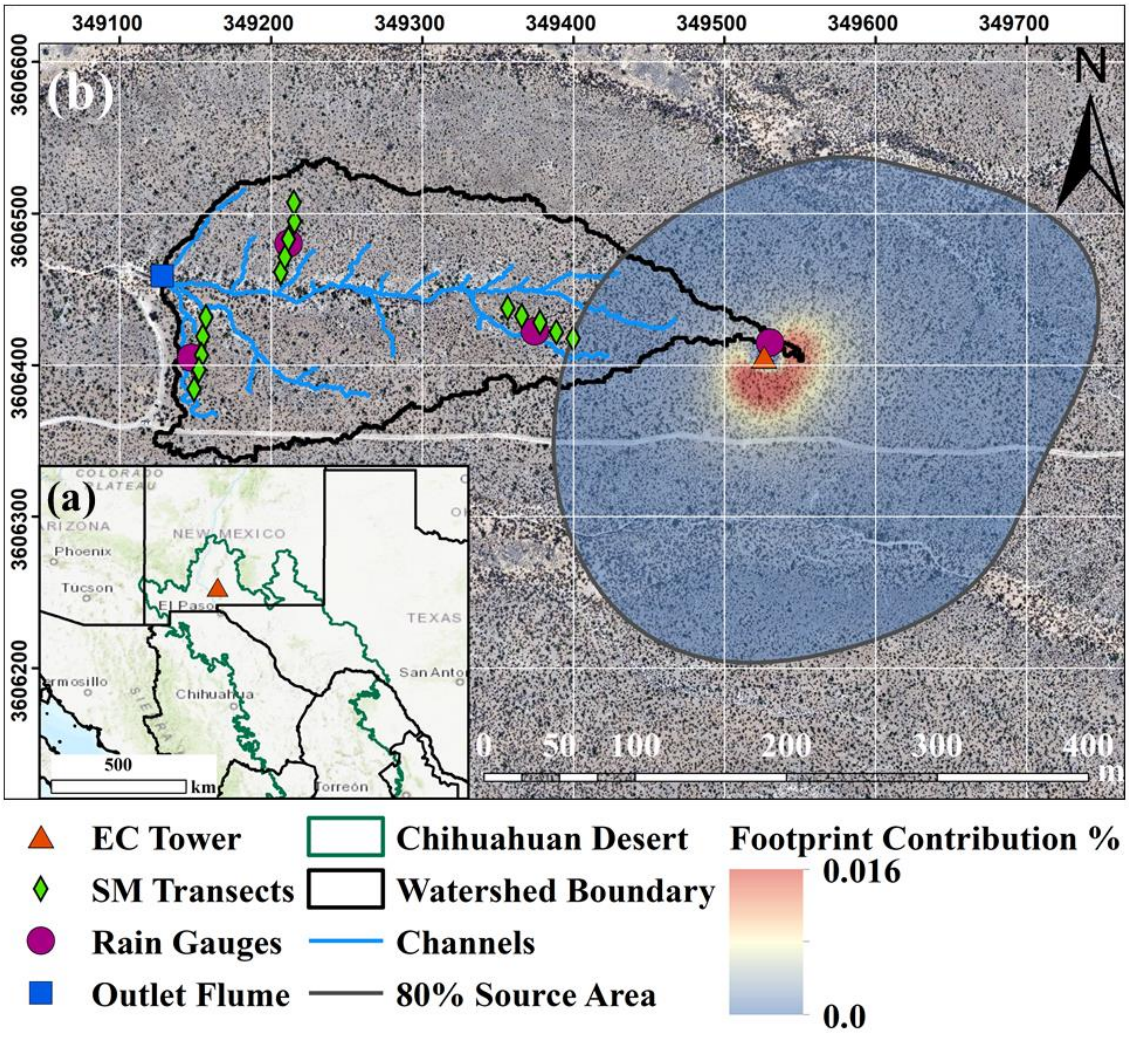

Figure 4.1: (a) Location of the study site in relation to the southwestern United States and the Chihuahuan Desert. (b) Instrumented first-order watershed showing the location of the eddy covariance (EC) tower, soil moisture (SM) transects, rain gauges, and outlet flume, as well as the 80% source area of fluxes and the percentage of contribution to the EC footprint.

registered as part of the Ameriflux network as "Jornada Experimental Range Mixed Shrubland" code US-Jo2 (https://ameriflux.lbl.gov/sites/siteinfo/US-Jo2), and data presented here are published at the AmeriFlux repository (Vivoni and Perez-Ruiz, 2021) .

Processed average 30-min fluxes were filtered to exclude periods with rainfall (R > 0.2 mm per 30-min), for data when winds were ±10˚ from the opposite direction of the

instruments (206 to 226°), and for data beyond plausible values ($NEP \pm 6$ μmol CO_2 m^{-2} s^{-1}, λET from -50 to 450 W m^{-2}, and H from -200 to 600 W m^{-2}), following the procedures of Schmid et al. (2000). We filtered the dataset using a friction velocity criterion of $u^* <$ 0.16 m s^{-1} estimated using the Moving Point Test (Papale et al., 2006). Gap filling of missing data was applied using Reichstein et al. (2005) through REddyProc (Wutzler et al., 2018). During the study period, about 36.0%, 35.4%, and 6.8% of data was missing for *NEP*, λET, and H respectively. The average footprint of the 80% source area was obtained using the approach of Kjlun et al. (2015), as shown in Figure 4.1b.

We estimated the components of *NEP*, ecosystem respiration (R_{eco}) and gross primary productivity (*GPP*), using the flux partitioning tool in REddyProc. Since $NEP = GPP - R_{eco}$, positive values of *NEP* represent carbon uptake, while negative values indicate carbon release. The partitioning procedure was based on the night-time sensitivity of *NEP* to air temperature (T_{air}) using the exponential regression model of Lloyd and Taylor (1994). As part of the quality control, we inspected the energy balance closure using two methods; (1) the ratio between the sum of scalar fluxes and available energy ($\varepsilon = \sum(H + \lambda ET) / \sum(R_n - G)$), and (2) a simple linear regression ($H + \lambda ET = m(R_n - G) + b$), where R_n is the net radiation and G is the ground heat flux measured at the EC site (Templeton et al., 2014). The energy balance closure was determined for periods of simultaneous fluxes, finding that results are within the range of other EC studies ($\varepsilon = 0.82$, $m = 0.61$, $b = 20.6$, and $R^2 = 0.83$) across different ecosystems (Wilson et al., 2002).

Water balance components were estimated following Schreiner-McGraw and Vivoni (2017). Rainfall (R) was measured using up to four tipping-bucket rain gauges (TE525MM; Texas Electronics, Dallas, Texas, USA; Vivoni et al., 2021a) to construct a

30-min spatial average using Thiessen polygons. Streamflow (Q) at 30-min intervals was measured at the outlet using a Santa Rita supercritical runoff flume (Smith et al., 1981), a pressure transducer (CS450; Campbell Scientific, Logan, Utah, USA), and a local calibration (Turnbull et al., 2013). Evapotranspiration (ET) was calculated at 30-min resolution with the EC method. The watershed average volumetric soil moisture (s) was obtained using soil dielectric probes (Hydra Probe; Stevens Water, Portland, Oregon, USA) along three hillslope profiles (sensors placed at 5, 15, and 30 cm depths) in the watershed (Vivoni et al., 2021b). Percolation (P) was estimated as the residual of the watershed water balance:

$$Z_r \frac{\Delta s}{\Delta t} = R - ET - Q - P, \quad (4.1)$$

where Δs is the change in volumetric soil moisture over the time interval Δt (1 month) and Z_r is the soil depth. Positive P values indicate percolation from the shallow soil surface into the deeper subsurface below Z_r, particularly due to channel transmission losses as a result from overland flow to the channel network by infiltration-excess runoff, while negative P values suggest an upward movement of water from beneath Z_r (Schreiner-McGraw and Vivoni, 2017). As the petrocalcic horizon is considered a semi-impermeable boundary, Z_r was estimated as 40 cm in (5).

Ancillary meteorological data

Long-term (1983-2015) daily averages of T_{air} and relative humidity (RH) were obtained from the JER LTER weather station (32°31'17" N, 106°47'50" W) (Anderson, 2018). Daily averages of vapor pressure deficit (VPD) were calculated from T_{air} and RH. Similarly, long-term (1915-2020) average monthly values of R were obtained from the JER Headquarters NOAA weather station (32°36'58.0" N, 106°44'25.5" W) (Thatcher,

2021). During the study period (2011-2020), 30-min averages of the energy balance components were obtained at the EC site, including R_n with a CNR2 sensor (Kipp & Zonen, Delft, The Netherlands) and G using a soil heat flux plate HFP01 (Hukseflux, Delft, The Netherlands) with corrections made using soil thermocouple probes TCAV (Campbell Scientific, Logan, Utah) at 2 and 4 cm.

Data analysis

We divided each year in two seasons that represent dry (January to June) and wet (July to December) periods, each with six months. The dry season included the six driest months, while the wet season consisted of the six wettest months. Daily values of the water balance components (R, ET, Q, s, and P), carbon fluxes (GPP, R_{eco}, and NEP), and meteorological data (T_{air} and VPD) were aggregated to monthly, seasonal, and annual scales (see Figure 4.2 for examples of daily variations of water and carbon fluxes). We compared water balance components and carbon fluxes across the dry and wet seasons using a Mann-Whitney U Statistic Rank Sum Test (Mann and Whitney, 1947). To assess the relationship between water and carbon fluxes, Pearson correlation coefficients were obtained between annual, dry season, and wet season sums. All statistics were tested with significance determined by $p < 0.05$ using IBM SPSS Statistics 26.

Results

Long-term seasonal variations of meteorological conditions

Figure 4.3 shows the long-term (1915-2020) monthly proportion of the annual rainfall (R) where the bimodal rainfall regime was dominated by the wet season (average of 186.9 mm) as compared to the dry season (average of 60.7 mm). On average, the wet season accounted for 75.5% of the annual R of 247.6 mm yr^{-1}, through the interannual

variability was high (see Peters et al., 2021 for additional details), with wet season *R* proportions ranging from 43.6% to 97.1%. However, more than 98% of the years had a wet season *R* that exceeded 50% of the annual *R* (Figure 2a inset). Long-term (1983-2015) records of T_{air} and *VPD* demonstrated the impact of the NAM on atmospheric conditions. In the dry season, the variables were coupled and showed increases until June, with minimum and maximum values of 6.5 °C and 27.8 °C and 5.3 hPa and 28.2 hPa, respectively. However, during wet season there is a decoupling between T_{air} and *VPD*, generating a period with high temperature but lower atmospheric water demand.

Seasonal variations of water balance components

During the study period, the site had similar distributions of *R* as compared to the long-term record (Figure 4.4, Table 4.1). The dry season received 67 ± 44 mm of *R* (ranging from 8.9 to 129.2 mm) representing a 24.4% of annual *R*, while the wet season had *R* of 211 ± 62.4 mm (from 82.3 to 291.1 mm) or 75.6% of annual *R*. Annual evapotranspiration (*ET*) represented 95.3% (264.8 ± 50.9 mm yr^{-1}) of annual rainfall. The remainder corresponded to streamflow from the basin (*Q*, 2.7% of annual *R* or 7.6 ± 6.7 mm yr^{-1}), percolation (*P*, 1.8% or 5.0 ± 38.4 mm yr^{-1}), and change in volumetric soil moisture (Δs, 0.5 ± 23.5 mm yr^{-1}).

In contrast to annual totals, the wet season had *ET*/*R* of 79.4% (167.6 ± 38.2 mm), leading to larger proportion of streamflow losses, *Q*/*R* = 3.6% (7.6 ± 6.7 mm), and percolation, *P*/*R* = 10.4% (21.8 ± mm), as well as to a greater amount of soil water storage, $\Delta s/R$ = 6.6% (14 mm). During the wet season, high *s* was more evenly distributed throughout the measured soil depth ending at Z_r, with seasonal averages of 6.9 ± 1.5%, 8.2 ± 1.6%, and 7.6 ± 1.3% at 5, 15, and 30 cm depths, respectively. Thus, the

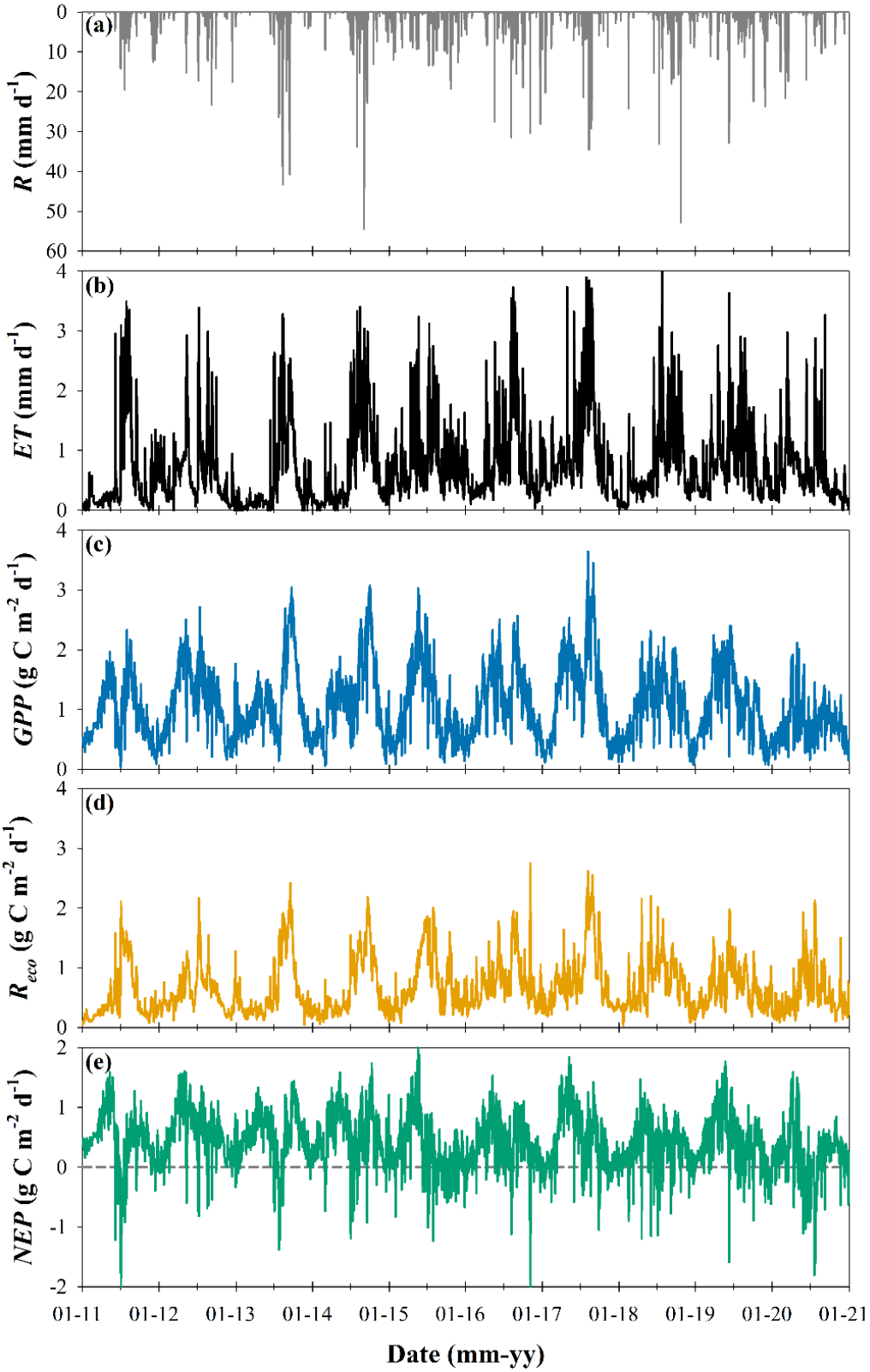

Figure 4.2: Daily values of water and carbon fluxes during the study period.

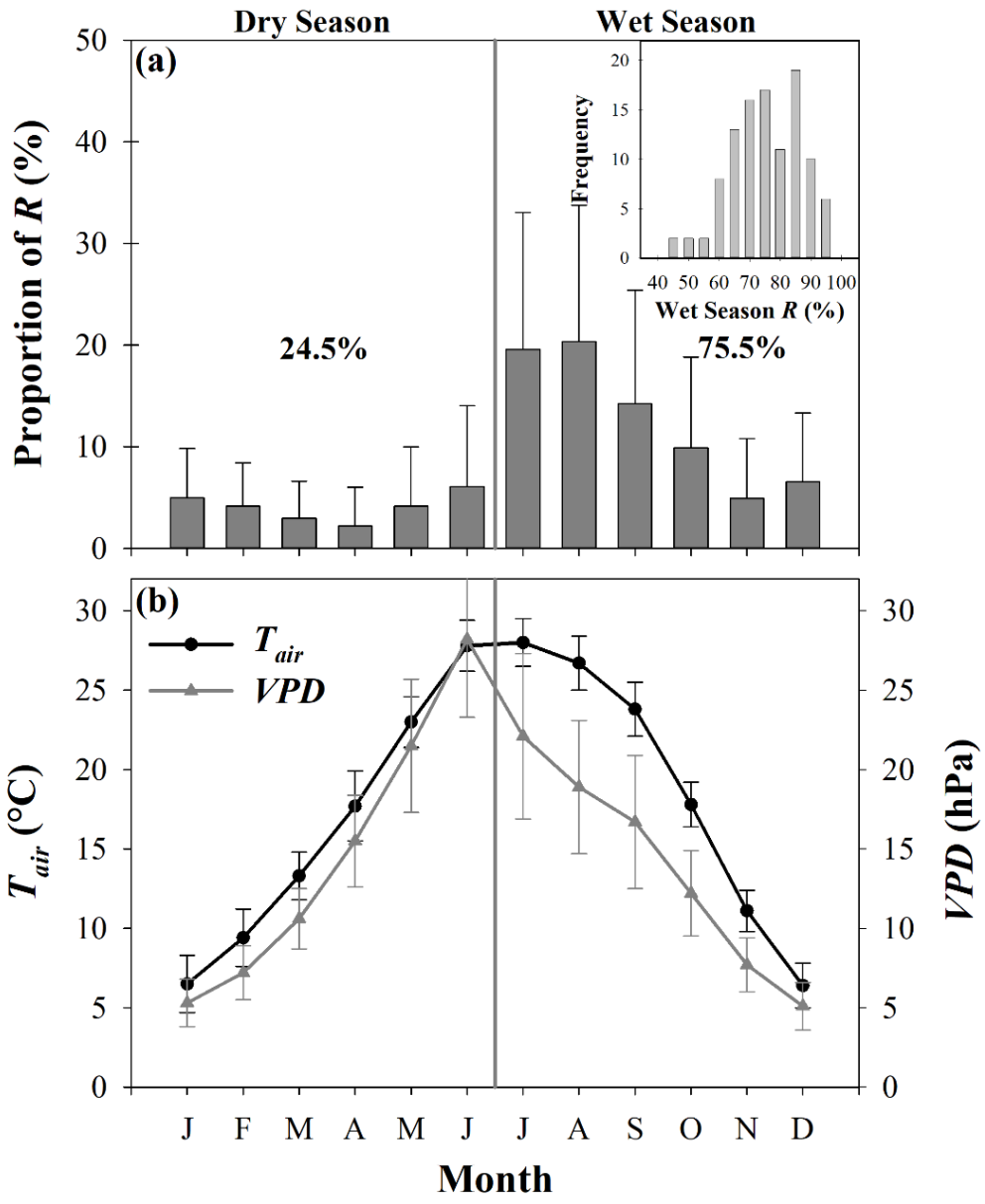

Figure 4.3: (a) Long-term (1915-2020) average monthly proportion (%) of annual rainfall (*R*). The inset is the frequency distribution of wet season proportion of annual *R* (%). (b) Long-term monthly averages of T_{air} and *VPD* (1983-2015). Bars represent ±1 monthly standard deviations. Vertical lines divide the dry and wet seasons.

wet season preferentially led to soil water increases in both the shallow and deep soil layers, with this latter mechanism inferred from the positive values of percolation. During the dry season, the shrubland had *ET* of 97.2 ± 49 mm, representing 145.3% of *R* (66.9 ± 44 mm) in the same period. During several months with *ET* much greater than *R* (April through June), reductions were noted in *s* throughout the soil depths and percolation was negative, indicating that water from deeper soil layers was consumed (Schreiner-McGraw and Vivoni, 2017). Of the additional water used by the mixed shrubland for *ET* during the dry season, 13.4 ± 12.6 mm corresponded to Δs and 16.8 ± 13.8 mm to *P*.

Seasonal variations of carbon fluxes

During the study period, the shrubland acted as a net carbon sink in all years, with an annual *NEP* of 153.2 ± 42.6 g C m^{-2} yr^{-1}, resulting from annual *GPP* of 393.6 ± 57.2 g C m^{-2} yr^{-1} and annual R_{eco} of 240.4 ± 38.6 g C m^{-2} yr^{-1} (Table 4.1). Seasonal differences in *GPP* and R_{eco} led to an uneven distribution of *NEP* among seasons (Figure 4.5). The dry season had a higher contribution to net carbon uptake during all years at 99.6 ± 26.7 g C m^{-2}, or 65% of the annual *NEP*, with the remainder during the wet season (Table 4.2). In contrast, *GPP* showed two evenly distributed peaks in the dry and wet seasons, contributing to 49.8% and 50.2% of the annual *GPP*. Variations in the seasonal distribution of *NEP* and *GPP* are attributed to R_{eco}, which had much higher values during the wet season (60.2% of annual R_{eco} or 144.1 ± 28.6 g C m^{-2}).

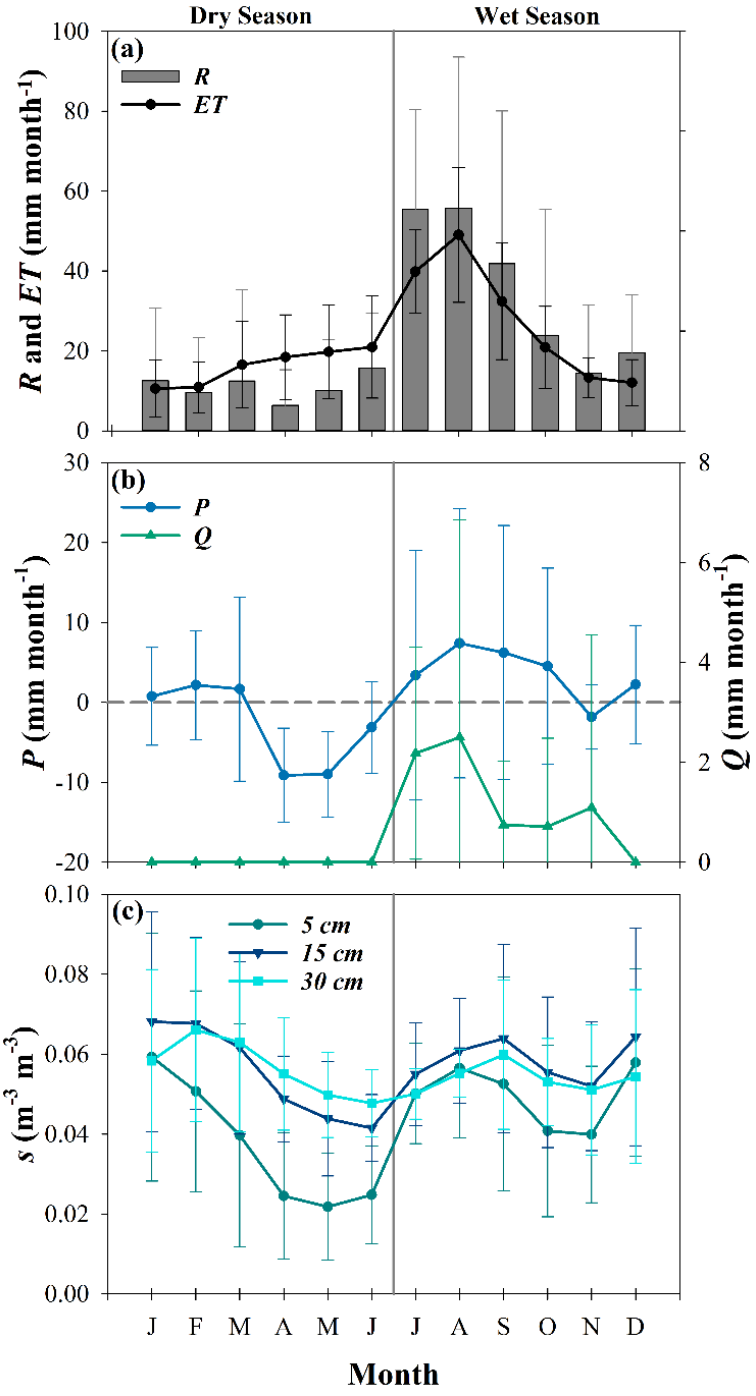

Figure 4.4: Monthly averages of water balance components from 2011 to 2020. (a) Rainfall (*R*) and evapotranspiration (*ET*). (b) Streamflow (*Q*) and percolation (*P*). (c) Volumetric soil moisture (*s*) at 5, 15, and 30 cm depths. Bars represent ± 1 monthly standard deviations. Vertical lines divide the dry and wet seasons.

Table 4.1: Annual values of water and carbon fluxes.

	2011	**2012**	**2013**	**2014**	**2015**	**2016**	**2017**	**2018**	**2019**	**2020**	**Total**
***R* (mm)**	193.3	212.4	284.7	307.8	303.2	332.5	327.3	329.7	276.4	211.4	2778.7
***ET* (mm)**	200.9	237.0	198.9	253.7	292.2	304.9	364.5	269.9	291.7	234.1	2647.8
***Q* (mm)**	2	8	11	6	0	20	17	6	6	0	76.0
***P* (mm)**	-56.6	-1.8	75.0	42.6	1.0	16.1	-39.7	26.9	-16.3	2.6	49.8
***GPP* (g C m^{-2})**	340.2	420.5	421.6	432.1	375.3	424	476.7	378.9	396.3	270.5	3936.1
***R_{eco}* (g C m^{-2})**	174.4	218.8	230.6	233.9	266.5	280.7	305.7	257.3	235.6	200.6	2404.1
***NEP* (g C m^{-2})**	165.8	201.7	191.0	198.2	108.8	143.3	171.0	121.6	160.7	69.9	1532.0

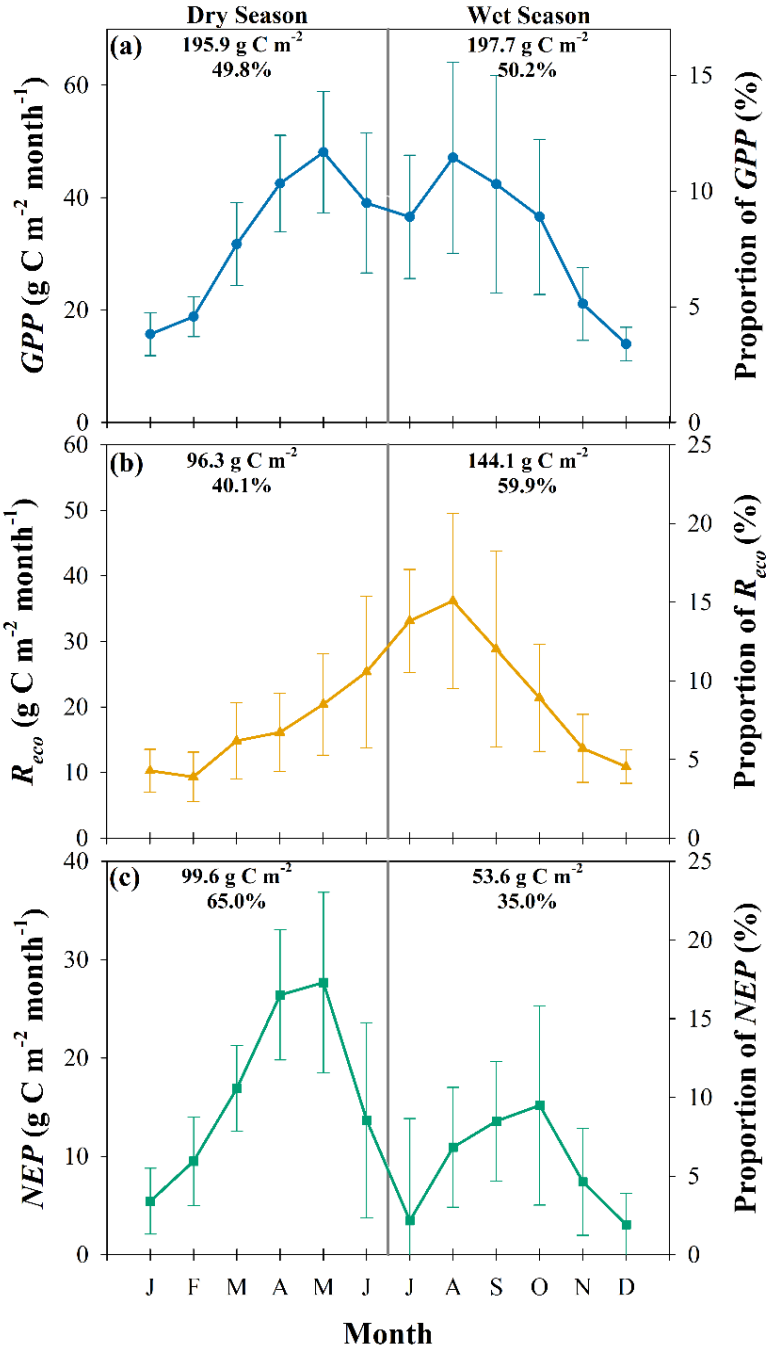

Figure 4.5: Monthly averages (left) and proportions (right) of carbon balance components from 2011 to 2020. (a) *GPP*. (b) R_{eco}. (c) *NEP*. Bars represent ± 1 monthly standard deviations. Vertical lines divide the dry and wet seasons.

Table 4.2: Seasonal values of water and carbon fluxes. Mean, Std., and CV are the average, standard deviation and coefficient of variation among years. Bold represents statistically significant difference between seasons ($p < 0.05$).

	***R* (mm)**		***ET* (mm)**		***GPP* (g C m^{-2})**		***R_{eco}* (g C m^{-2})**		***NEP* (g C m^{-2})**	
	Dry	**Wet**	**Dry**	**Wet**	**Dry**	**Wet**	**Dry**	**Wet**	**Dry**	**Wet**
2011	**8.9**	**184.4**	**37.7**	**163.2**	170.1	170.1	**53**	**121.4**	**117.1**	**48.7**
2012	**45.3**	**167.1**	112.2	124.8	**228.0**	**192.5**	99.8	119	**128.2**	**73.5**
2013	**13.6**	**271.1**	**21.5**	**177.4**	**175.2**	**246.4**	**61.3**	**169.3**	**113.8**	**77.1**
2014	**16.6**	**291.1**	**41.6**	**212.1**	**168.8**	**263.3**	**55**	**178.9**	**113.8**	**84.4**
2015	99.9	203.4	**128.5**	**163.7**	**226.4**	**148.9**	126.5	140	**99.9**	**8.9**
2016	**85**	**247.4**	**116.4**	**188.5**	214.9	209.1	**124.8**	**155.9**	**90**	**53.3**
2017	111.1	216.2	150.1	214.4	229.0	247.7	**117.4**	**188.3**	**111.6**	**59.4**
2018	**61.3**	**268.4**	**75.9**	**194**	**177.4**	**201.5**	**110.7**	**146.6**	66.7	54.9
2019	98	178.4	149.1	142.6	**234.5**	**161.8**	121.3	114.3	**113.2**	**47.5**
2020	129.2	82.3	**138.9**	**95.2**	134.8	135.7	**93.3**	**107.3**	41.6	28.3
Mean	66.9	211.0	97.2	167.6	195.9	197.7	96.3	144.1	99.6	53.6
Std.	44.0	62.4	49.0	38.2	34.7	44.3	29.5	28.6	26.7	22.7
CV	65.8	29.6	50.4	22.8	17.7	22.4	30.6	19.8	26.8	42.3

Water-carbon dynamics

Table 4.3 shows the Pearson correlation coefficients between water balance components (*R*, *ET*, *Q*, and *P*) and carbon fluxes (*GPP*, R_{eco}, and *NEP*) for annual and seasonal periods. *GPP* generally showed positive correlations with water balance components, but these were only significant for the wet season. A significant negative correlation between *GPP* and *P* in the dry season can be attributed to the upward movement (negative *P*) of deeper soil water (Figure 4.4). R_{eco} showed a statistically significant correlation with both *R* and *ET* over the annual scale and for each season suggesting that water availability was critical for carbon releases. As a result of the different correlations for *GPP* and R_{eco}, *NEP* generally showed non-significant relations with the water balance components, in particular at the annual scale and for the wet season. A negative correlation between *NEP* and *P* during the dry season suggests that higher carbon uptake is linked to uptake of subsurface water below Z_r available from the prior wet season.

Figure 4.6 shows how the wet season rainfall was linked to the seasonal and annual *NEP* in the shrubland ecosystem. Annual *NEP* was calculated from July to June to capture the potential carry-over effect from a wet season to the subsequent dry season. We excluded calendar year 2020 from the analysis as datasets were not available yet for 2021. All years from 2011 to 2019 had wet season rainfall amounts that accounted for greater than 64% of the annual *R*. In contrast, the wet season proportion of *NEP* remained below 45% of the annual *NEP*, indicating a dominance of dry season in the annual ecosystem productivity. Despite a significant short-term decrease of wet season *R* during the study period, no significant trend was noted in wet season *NEP*, suggesting a lack of

Table 4.3: Pearson correlation coefficients between carbon fluxes (*GPP*, R_{eco}, and *NEE*) and water balance components (*R*, *ET*, *Q*, and *P*) for annual and seasonal values. Bold represents statistically significant correlation at $p < 0.05$.

	Annual			**Dry Season**			**Wet Season**		
	GPP	***R_{eco}***	***NEP***	***GPP***	***R_{eco}***	***NEP***	***GPP***	***R_{eco}***	***NEP***
R	0.614	**0.883**	0.023	0.261	**0.799**	-0.544	**0.788**	**0.782**	0.552
ET	0.503	**0.879**	-0.121	0.524	**0.849**	-0.258	**0.788**	**0.893**	0.414
Q	**0.749**	**0.656**	0.410	--	--	--	**0.640**	0.613	0.477
P	0.159	0.096	0.125	**-0.713**	0.228	**-0.675**	0.553	0.459	0.502

sensitivity to rainfall in the wet season. Nevertheless, the annual *NEP* was significantly controlled by wet season *R*, implying that carried-over subsurface water influenced the dry season and annual scale ecosystem productivity in the mixed shrubland.

Discussion

Ecosystem water use and its sources

In arid and semiarid regions, evapotranspiration is the principal means by which water is lost from an ecosystem, and the ratio *ET*/*R* tends to be close to 1 on annual to interannual scales (e.g., Kurc and Small, 2004; Yépez et al., 2007; Scott, 2010; Tarín et al., 2020; Vivoni et al., 2021). However, the seasonality of subsurface water storages can lead to seasons or longer periods when $ET/R > 1$ (e.g., Scott et al., 2008; Flerchinger et al., 2020; Knowles et al., 2020; Pérez-Ruiz et al., 2021). While this has been recognized in other settings, we found that a mixed shrubland watershed of the Chihuahuan Desert relied on carry-over subsurface water to support ecosystem productivity during the dry season. High rainfall during the wet season

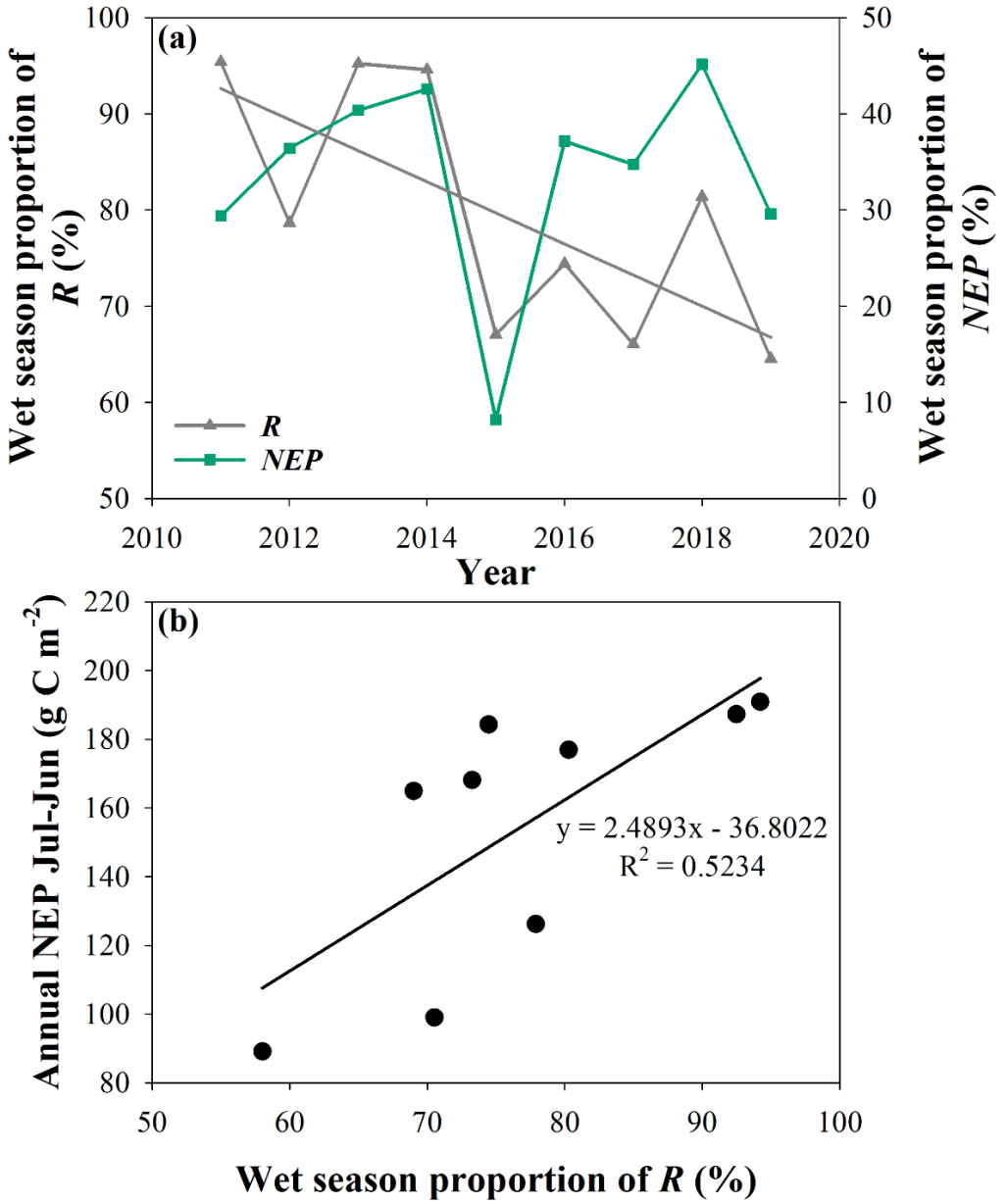

Figure 4.6: (a) Wet season proportions (%) of rainfall (*R*) and net ecosystem production (*NEP*) from 2011 to 2019. (b) Relation between wet season proportion of *R* and annual *NEP* obtained over the period July to June. Calendar year 2020 is excluded from this analysis. Lines represent statistically significant correlations.

provided sufficient water to meet the ecosystem water use (wet season ET/R = 0.79), despite the small losses to runoff (Q/R = 0.04), while also supporting large increases in shallow and deep soil water, $(\Delta s + P)/R$ = 0.17. As described by Schreiner-McGraw and Vivoni (2017), summer storms led to soil infiltration and hillslope runoff that contributed to percolation or transmission losses in the downstream channel, both serving as carry-over water for subsequent seasons. Percolated water beyond Z_r can remained stored in deeper layers of the channel sediments or in or beneath the petrocalcic horizon (Duniway et al., 2007, 2010). Shallow soil water was consumed rapidly in the fall season, while percolation persisted to at least the following spring.

During the dry season, ecosystem water use exceeded the seasonal water input (ET/R = 1.45), implying that 30.3 mm on average was from carry-over subsurface water storage, of which about half of the amount (13.4 mm) was stored in the soil profile above Z_r. Below Z_r, the presence of petrocalcic horizons could provide the opportunity to store water which is available for plants to extract over periods from several months to a year (Duniway et al., 2007, 2010). The deep rooting systems of creosote bush, honey mesquite, and tarbush can extend into and below $CaCO_3$ horizons as well as into the subsurface sediments underneath sandy channels (e.g., Gile et al, 1998; Gibbens and Lenz, 2001; Schwinning, 2010). Large, negative values of percolation in the dry season (P/R = -0.30) indicated an upward movement of water that is simultaneous with springtime evapotranspiration and carbon uptake. Of the several species in the shrubland, evergreen creosote bush and winter deciduous honey mesquite have phenological activity during the dry season which could be linked to the uptake of deep soil water (e.g., Muldavin et al., 2008; Kurc and Benton, 2010; Schreiner-McGraw and Vivoni, 2018).

Water use efficiency and bimodality of ecosystem production

Shrublands in the North American deserts are net carbon sinks at the annual scale (e.g., Petrie et al., 2015; Biederman et al., 2017; Verduzco et al., 2018; Hinojo-Hinojo et al., 2019) and it has been argued that the winter season plays an important role through a reduced amount of ecosystem respiration (Biederman et al., 2018). At our mixed shrubland site, we found that the ecosystem carbon balance was strongly affected by the seasonality of both *GPP* and R_{eco}. Water use efficiency (*WUE* = *GPP*/*ET*) during the dry season (*WUE* = 2.02 g C per mm H_2O was substantially larger than during the wet season (*WUE* = 1.18 g C per mm H_2O). We attribute this to the consumption of carry-over water from subsurface storage augmenting available rainfall and the lower evaporation rates from large fractional bare soil in the dry season (e.g., Yépez et al., 2007; Wang et al., 2010; Scott and Biederman, 2017). These results were consistent when using rainfall use efficiency with rainfall as a measure of water availability instead of evapotranspiration. Lower wet season *WUE* is another indication that water is available beyond evapotranspiration demands and leads to subsurface storage through infiltration or transmission losses. This seasonal behavior is consistent with the lower *WUE* identified as mean annual precipitation increases across biomes (Huxman et al., 2004b)

The dominant contribution of the dry season to net ecosystem productivity in shrublands has been attributed to winter rainfall (e.g., Huenneke et al., 2002; Huxman et al., 2004a; Wohlfahrt et al., 2008; Muldavin et al., 2008; Petrie et al., 2015; Biederman et al., 2018). We found that *GPP* showed a bimodal pattern in shrub productivity during the year that cannot be solely explained by dry season rainfall since *ET*/*R* largely exceeds unity. The decoupling of *ET* and *R* in the dry season, despite the high *GPP*, indicates an

important component of carry-over subsurface water from prior wet seasons. Notably, the bimodality observed in *NEP* during the year is asymmetric, with higher values in the dry season than in the wet season, leading to 65% of the annual carbon uptake occurring in the dry season. We attribute this to the dependance of R_{eco} on higher air temperature (Reichstein et al., 2005) and water availability in shallow soils (e.g., Kurc and Small, 2007; Anderson-Teixera et al., 2011; Biederman et al., 2018) which were more prominent during the wet season. Higher R_{eco} in the wet season counteracted the nearly equal seasonal amounts of *GPP* and led to the asymmetric bimodality in *NEP*. The bimodality in *GPP* and *NEP* are consistent patterns across all years but exhibited interannual variations in relative size depending on the seasonal water availability.

Role of wet season hydrological partitioning

The interannual variability of water-carbon dynamics revealed that net ecosystem productivity during the wet season was unaffected by its proportion of annual rainfall. Note that the wet season contributed about 75% of annual *R* on average, such that it is the main source of water to the ecosystem. We attribute this to the inability of the sparse shrubland to fully utilize available soil water within the wet season as well as the hydrological processes leading to runoff production and channel transmission losses (Schreiner-McGraw and Vivoni, 2017). Despite a decreasing trend in the wet season proportion of annual rainfall, no trend was observed in the wet season proportion of *NEP* (average of 45% of annual *NEP*). Though the sensitivity of *NEP* to rainfall is low within the wet season, we found a statistically significant relation between the wet season proportion of *R* and the subsequent annual *NEP*. This evidence indicated the importance of the wet season in defining the magnitude of the annual carbon sink in the mixed

shrubland ecosystem. Higher proportional rainfall during wet season benefits the hydrological partitioning of water into subsurface storage which then serves to increase the dry season *NEP*. The lagged effect mediated by landscape properties in the watershed (e.g., $CaCO_3$ horizons in hillslope soils, subsurface porous media under channels) allowed for water to be reserved for ecosystem use during the dry season when *GPP* can be sustained at higher levels than R_{eco}, thus enhancing annual *NEP* and the strength of the mixed shrubland carbon sink.

The study period was characterized by average rainfall conditions at the JER as compared to the long-term record, as noted by Peters et al. (2021) who analyzed multi-year sequences of above-, below- and average precipitation each lasting about 5 to 6 years. As a result, the effects of the carry-over subsurface water on the annual carbon budget are robust features during average hydrological conditions of the study site. Furthermore, comparisons to the work of Reichmann et al. (2013) at a nearby flat location at JER are illustrative of the importance of landscape properties in the watershed on the seasonal carry-over effect. The authors showed through a rainfall manipulation experiment that soil water was not carried from one season over to the next, even under extreme conditions when precipitation was increased by 80%. As a result, the connected system of hillslopes and channels in the shrubland watershed favored subsurface water storage used in the subsequent dry season. We hypothesize that landscape properties, such as bare soil cover and its connectivity in the shrubland, and terrain conditions, such as slope and the arrangement of hillslopes and channels, will determine the degree of carry-over water in a watershed setting. Thus, enhancements in subsurface water storage, for instance through higher shrub cover or more permeable channels (Schreiner-McGraw

and Vivoni, 2018; Schreiner-McGraw et al., 2020), promote a larger annual fraction of productivity during the dry season.

Conclusions

In this study, we found that hydrological partitioning has an amplified role on ecosystem productivity in a mixed shrubland of the Chihuahuan Desert that exhibits topographic and subsurface complexity. Fed by soil infiltration and channel transmission losses, the subsurface environment can serve as a temporary water storage reservoir that can be accessed by deep rooted shrubs over longer time scales. As a result, water recharged during periods of high rainfall can support ecosystem water use in dry periods, including the subsequent spring. In addition, this carry-over effect allows evapotranspiration and gross primary productivity to occur when shrub phenological processes are more favorable since ecosystem respiration and soil evaporation are more limited under dry shallow soils and lower temperatures. For larger proportions of water during the summer, evapotranspiration and gross primary productivity are favored to a greater extent, allowing for a stronger net carbon sink. While previous studies have highlighted the important role of winter periods for North American shrubland carbon dynamics, we documented how hydrologic and ecological processes interact to favor the establishment of deep-rooted shrubs in complex watersheds that can store water in the subsurface across multiple seasons.

CHAPTER V

CONCLUSIONS, FUTURE WORK, IMPLICATIONS AND DATA AVAILABILITY

Conclusions

Landscapes biogeochemical processes in arid and semiarid areas of southwestern US and northwestern México have a clear dependance to precipitation and water availability, and the NAM provides most of the water input to support the biophysical processes of ecosystems, however, landscapes characteristics, such topographical position, elevation, complex terrain, access to groundwater, microclimatic conditions or land cover heterogeneity, can play a fundamental role in differentiating the individual responses of ecosystem processes. For that reason, it is important to understand how different landscape controls modulate the ecosystem dynamics, particularly the biosphere-atmosphere energy and mass exchanges.

In Chapter 2, the role of anthropogenic, biogenic, and meteorological controls on carbon fluxes was explored in four different urban landscapes within the Phoenix Metropolitan Area (PMA) through turbulent flux measurements using the EC technique. Urban landscapes represented typical land covers of the PMA, encompassing a highly urbanized site (parking lot, PL), a highly vegetated site (mesic landscape, ML) and two mixed sites (xeric landscape, XL, and suburban neighborhood, REF). Urban landscape controls evaluation included: (1) vehicular influence through relating carbon fluxes to traffic counts and comparing days with high vehicular activity (weekdays) and low vehicular activity (weekends); (2) vegetation activity through relating carbon fluxes to vegetation fractions and indices and comparing days with normal radiation input (sunny)

and low radiation input (cloudy); and (3) precipitation influence through the comparison of carbon fluxes for wet and dry days.

Results showed a behavior of carbon fluxes consistent with the urban land cover type during the sampling periods, with landscapes with medium to high urbanization (PL, XL and REF) acted as net sources of carbon, while the highly vegetated site (ML) acted as a net sink of carbon. Sites with large transportation surfaces (PL, XL and REF) showed a clear dependance of diurnal variations to rush hours and traffic counts, and a statistically significant difference was found between days with low (weekends) and high (weekdays) vehicular activity. In sites with irrigation-supported vegetation (ML, XL and REF), mid-day values of carbon fluxes showed a consistent pattern with maximum vegetation activity and the increase in latent heat flux and showed a statistically significant difference between days with normal (sunny) or low (cloudy) radiation input. Finally, where outdoor water use is abundant and frequent, carbon fluxes were insensitive to the occurrence of precipitation (wet versus dry days) or the time since the last rainfall event. Based on the results obtained, vegetation fraction and built surfaces contributed to the differentiated behavior of carbon fluxes in urban patches. Two sites can be considered as end members that are dominated either by the effects of traffic and other anthropo- genic emissions (PL) or by the carbon dioxide uptake from vegetation activity (ML). The other two sites (XL and REF) are characterized by combinations of these land cover types and thus exhibit intermediate or mixed behavior with respect to carbon fluxes conditions.

In Chapter 3, the role of elevation-induced soil and microclimatic conditions and access to groundwater on water-energy and carbon fluxes was evaluated in three different ecosystems in northwestern México during the NAM of 2017. The ecosystems consisted

in a subtropical scrubland (SS) which represented a low elevation ecosystem with no access to groundwater, a riparian mesquite (RM) which represented a low elevation ecosystem with intermittent access to groundwater, and an oak savanna (OS) representing a high elevation ecosystem with stable groundwater access. Analysis performed allowed an assessment of the field campaign conditions with respect to long-term precipitation data, remotely-sensed vegetation, and flux measurements which permitted inferences to be made across a larger region and across other time periods. Analysis to determine relations between water and carbon fluxes to landscape controls were conducted dividing the NAM in four stages: (I) pre-monsoon corresponding to the dry season prior to the beginning of the NAM, (II) early monsoon at the onset of the NAM, (III) late monsoon during the peak of the NAM, and (IV) post-monsoon at the end of the NAM.

Rainfall and vegetation during the onset of the NAM of 2017 showed a magnitude and response above the long-term average, however, as the NAM advanced, the late monsoon exhibited a lower activity leading to a shorter duration of the NAM as compared to the long-term behavior. This affected primarily the lower elevation with no groundwater access site (SS) but had minor effect in the high elevation site with access to groundwater (OS). Despite having similar amounts of precipitation, groundwater-induced differences led to divergent patterns of water and carbon fluxes, with SS and RM acting as net sources of carbon and OS acting as a net sink of carbon during the NAM season. This suggested that soil and microclimatic conditions modulated the seasonal carbon budget through differential effects on ecosystem respiration and gross primary productivity, as evapotranspiration and carbon flux components showed a statistically significant positive correlation with temperature, and soil moisture promoted high

evapotranspiration on all sites and ecosystem respiration in sites with groundwater access, as ecosystem respiration is mostly controlled by shallow soil moisture. Groundwater use estimations showed the riparian (RM) and mountain (OS) settings were likely dependent on subsurface water as ecosystems consumed more water than the total rainfall, while SS was dependent solely on shallow soil water, leading to differences in water use efficiency.

Finally, in Chapter 4 I investigated the seasonal dynamics in hydrological partitioning and its relation to primary productivity in a mixed shrubland of the Chihuahuan Desert over a 10-year study period. Some shrublands in the NAM area follow a bimodal productivity regime that is controlled by the winter and summer seasons water availability. Measurements and estimations of carbon fluxes (net ecosystem production, gross primary productivity) and water balance components (rainfall, evapotranspiration, streamflow, soil moisture storage change and percolation) were made in a small first-order watershed with complex terrain. To perform the seasonality analysis, the year was divided in two six-month seasons, representing the dry (January to June) and wet (July to December) seasons and daily values were aggregated to monthly, seasonal, and annual scales. Water balance components and carbon fluxes were compared across the dry and wet seasons and the relationship between water and carbon fluxes was assessed for annual, dry season, and wet season sums.

In this study, divergent seasonal dynamics in hydrological partitioning and carbon fluxes were found, which led to differences in water use and water sources in the ecosystems and in the response and behavior of net productivity components. Wet season rainfall provided sufficient water to meet the ecosystem water use and supported large

increases in shallow and deep soil water. During the dry season, ecosystem water use exceeded the seasonal water input, implying that excess water use was from carry-over water accumulated in the subsurface during the wet season. Ecosystem carbon balance was strongly affected by the seasonality of both productivity and respiration, with an evenly distributed seasonal bimodal regime of gross productivity and a wet season dominated respiration regime, which created a dry season dominated net carbon uptake. In the ecosystem, subsurface carry-over water from the wet season can serve as moisture storage to support ecosystem activity during the dry season and causing the ecosystem to be a constant net sink of carbon.

Overall, the results and conclusions of this dissertation represent an important contribution to the understanding of how the inherent landscape characteristics of ecosystems in arid and semiarid areas control and modulate the differential response of ecosystem, despite a clear general dependence to precipitation and water availability.

Future work

While the outcomes of this dissertation imply a significant input to the knowledge of the dynamics of arid and semiarid landscapes, an area of opportunity looms on the horizon.

In Chapter 2, results clearly showed the differential influence of anthropogenic, biogenic, and meteorological factors on different urban landscapes, and the reference site served as a key element to the conclusions found, as mobile deployments spanned short-term non simultaneous periods. Even when results are valuable, it would be desirable to perform a full-year comparison between sites which would allow researchers to

determine the annual sink or source behavior of the urban landscapes as well as allow a spatio-temporal comparison of vehicular and vegetation activity and precipitation influence over the entire span of seasonal environmental forcing. Results obtained can be of great value to perform comparisons with bottom-up approaches to elucidate sources and sink of carbon in urban patches as well as to help in the validation of modelling and simulation efforts of fluxes in urban landscapes.

The results of Chapter 3 remain conditioned on a single NAM season, and despite the long-term context of rainfall and vegetation response, field monitoring efforts spanning the entire year would be needed to define the annual source and sink behavior of the ecosystems and to identify the effect of seasonality of the ecosystems in a gradient of elevation and groundwater access. A field monitoring able to capture the inter-annual variations would have an incredible potential due to the high interannual variability of the NAM, however, logistic constrains in the area could potentially limit efforts of this nature, but future work should consider the permanent installation of water-energy-carbon flux sites.

Additionally, Chapter 3 just evaluated the landscape controls over a low elevation site with no groundwater access, a low elevation site with groundwater access and a mountain site with groundwater access. Future efforts must include a mountain site with no access to groundwater to guarantee a fairer comparison and to allow a better isolation of elevation-induced landscape controls on water-energy-carbon fluxes. The use of NDVI in the study clearly captured the phenological response of the intensive and extensive water use traits, so the use of long-term NDVI data as well as other remotely-sensed products (for instance, evapotranspiration, gross primary productivity, etc.), together with long-

term meteorological data, could help to understand the response of ecosystems to the interannual variability of the NAM over a more extended area.

Finally, the long-term nature of the datasets used in Chapter 4 offer an excellent opportunity to explore the response of the mixed shrubland of the Chihuahuan Desert to a wide range of controlling factors at different time scales. For instance, the role of interannual variability of precipitation in modulating the response of water and carbon fluxes, the control of precipitation events characteristics (intensity, frequency, etc.) in the hydrologic partitioning and the carbon balance, meteorological controls on the carbon balance in the study site, among others. Additionally, a clear potential exists to explore to which extent the bimodal regime of vegetation productivity and the dry season dominance of net productivity extends in the ecosystem of the area or if a gradual trend to a wet season dominated productivity exists with a woody plant encroachment or grass domination gradient. Not only the use of others field monitoring sites (AmeriFlux or Fluxnet for instance) is useful but also the use of remote sensing gross primary productivity products to include a wider spatio-temporal context. For instance, MODIS GPP product captures the bimodality of productivity of the mixed shrubland in a similar way than the flux measurements. MODIS GPP could be used to explore the spatio-temporal dynamic of vegetation productivity in the shrublands of North America. This can be compared with the AmeriFlux available data for North American shrubs. Additionally, numerical models considering hydrological and phenological variables typically do not consider the use of water from deeper layers of the soil or carry-over moisture and are not able to capture the bimodality of vegetation productivity. Our

findings can help model developers to consider in their simulations the effect of carry-over moisture in vegetation productivity.

As part of my future academic and research activities in México, I will continue addressing the ecohydrology of arid and semiarid landscapes, particularly focusing on urban landscapes and ecosystems of the Chihuahuan Desert. Currently, a flux monitoring site exists in one of the campus of the Universidad Autónoma de Ciudad Juárez, which is registered in the AmeriFlux network as "MX-Iit: Instituto de Ingenieria y Tecnologia – UACJ" (https://ameriflux.lbl.gov/sites/siteinfo/MX-Iit). This monitoring site will allow me to continue with the study of the role of urban landscapes characteristics in water, energy and carbon fluxes. Additionally, I will involve in the consolidation of MexFlux, the network of ecosystem fluxes monitoring sites of México, where I pretend to contribute with data management, quality control and synthesis analysis of fluxes in Mexican ecosystems. The wide variety of urban, natural and agroecosystem in México could offer an opportunity to elucidate a variety of mechanisms that control the water, energy and carbon fluxes in a wide range of biomes, elevations and hydroclimatic conditions.

Implications

The results of this dissertation represent an important contribution to the knowledge of the landscape control over land surface-atmosphere fluxes and as expected, a series of questions emerge when trying to elucidate the mechanisms behind the landscapes controls, particularly the role of subsurface water and carry-over moisture in sustaining ecosystem productivity, the bimodality of vegetation productivity, the actual

water sources to support that productivity and the role of land management and vegetation structure in defining the water use and productivity of ecosystems. In the case of Chapter 4, the long-term nature of the datasets offers the potential of performing additional analysis that could help to explain several questions that arose during the discussion of the results.

For instance, even when Schreiner-McGraw and Vivoni (2017) mentioned runoff from hillslopes contributed significantly to deep percolation through channel transmission losses, our results indicate the percolated water is being used by vegetation to support productivity during dry season, but where is this carry-over water being store? How do the shrubs in the landscape obtain this stored water? Petrocalcic horizons have the capacity to retain large quantities of water (Duniway et al., 2007), however it is not clear if water is being stored in the channel and then redistributed to the petrocalcic horizon, if infiltration in the hillslope recharge the petrocalcic horizon or if both mechanisms can occur. Shrubs in the study site have roots systems that can access the stored water in the petrocalcic horizon, however, it is not clear how plants obtain the water. Water use by plants could be obtained by the root system in the petrocalcic horizon, but maybe shrub root systems can access water stored in layers deeper than the petrocalcic horizon, have a root system so complex that reach water stored in the channels or even perform hydraulic redistribution as a competition or survival mechanism.

Woody plant encroachment, hydroclimatic variability as well as land management in the last 150 years have created the mixed shrubland landscape studied in Chapter 4. The status of the landscape is responsible for the ecohydrological mechanisms studied in

Chapter 4; however, it is interesting to speculate how spatio-temporal variations on land management, woody plant encroachment and vegetation phenology could affect the land surface-atmosphere fluxes in the ecosystems of southwestern USA and northwestern México. For instance, several phenological patterns are present in the different shrub and grass species of the site. Wet season provides sufficient water to support a generalized response of all plants in the ecosystem. Most of the plants remain dormant during dry season, however, creosote bush is an evergreen shrub active year-round, and mesquites have a blooming period during spring. This differences in phenological response indicate that vegetation productivity during the wet season is because of a generalized greening of shrubs (creosote, mesquite, tarbush, mariola, etc.) and grasses, while mesquite and creosote, which have deep root systems, are responsible for dry season vegetation productivity.

The carry-over processes leading to the bimodality of vegetation productivity in the ecosystem can be explained by the vegetation phenology and water sources described in the two previous paragraphs. However, it would be interesting to analyze how much of this bimodality in productivity can be explained by the process of woody plant encroachment. For instance, a study encompassing the water use, water sources and productivity of ecosystems in a woody plant encroachment gradient from grassland to shrubland would be useful. In this case, ecosystems with similar characteristic to our study site (high connectivity, shrub dominated, complex terrain, etc.) could have a similar bimodal productivity regime supported by carry-over moisture. However, changes in ecosystem structure can lead to different productivity and water use patterns. An ecosystem in a flat terrain would have a lower runoff generation and channel

transmission losses decreasing the deep percolation. The presence of grasses could have an impact not only in the ecosystem productivity but also in the hydrologic partitioning. For instance, a combination of shrubs and grasses would represent the presence of two different functional traits and the decrease of exposed bare soil. While shrubs tend to use water from deeper layers of the soil, grasses with shallow roots systems use rapid and actively the water in shallow layers in the soils. The use of water in both shallow and deep layers of the soil would decrease the infiltration rates and thus the percolation to deeper layers of the soil in hillslopes. Furthermore, a higher grass cover would decrease runoff generating and sheetflow with a subsequent decrease in channel transmission losses and deep percolation. The decrease in infiltration and deep percolation could have an impact diminishing the amount of water stored in deeper layer of the soil, generating a weaker carry-over process, and creating an ecosystem with a higher dominance of wet season productivity.

Even as the arguments proposed in the previous paragraph are focused on a woody plant encroachment gradient, the carry-over soil moisture dependance of ecosystems can also be analyzed in a different context. In Chapter 3, the riparian mesquite and oak savanna had also a dependance to deep soil water. In this case, the riparian and mountain nature of the ecosystems provided the additional sources of water to support the water use during the NAM season. However, as the study was delimited to a single NAM season, it is not clear if the additional sources of water corresponded to carry-over moisture from previous seasons or if the NAM provided enough water to have an exceeding storage of water in the riparian landscape and in the bedrock in the mountain setting. Of course, the functional traits and rooting systems of the vegetation in

the riparian mesquite and oak savanna are different than those in the mixed shrubland, so similar carry-over processes, water use, and water sources are likely to be different.

The carbon sink behavior of shrublands in North America has been assessed by several studies. Values of ecosystem productivity have been obtained using several methodologies, including allometric equations, remote sensing products, eddy covariance, etc. Values of *NEP*, *GPP* and R_{eco} found in our mixed shrubland are comparable with those obtained with similar methods (Petrie et al., 2015; Biederman et al., 2018) and to MODIS GPP but higher than those reported for aboveground net primary production (ANPP), which only consider the carbon gained by aerial plant coverage and not root development and soil respiration (Muldavin et al., 2008). It is not clear where the carbon is accumulating in the study site to be consistently a carbon sink. Changes on vegetation cover, aerial and root biomass increase or organic matter in the soil would need to be monitored extensively to determine if the vegetation is contributing to store the captured carbon. Additionally, it would be possible that inorganic carbon pools, as the augmentation of the petrocalcic horizon could be playing a more important role in the carbon sink behavior of the ecosystem.

Finally, land management can have a preponderant effect in modifying the landscapes characteristics. Even when our mixed shrubland site has not have a recent record of grazing and fire, land management techniques can lead to changes in landscapes controls, ecosystem structure and vegetation productivity. Excessive grazing has been recognized as an important factor contributing to woody plant encroachment. It not only decreasing the grass cover, but it can contribute to the compacting of soil, increasing the organic matter of soil and damaging the structure of plants. Fires have the potential to

consume larges areas of grasslands and shrublands in short periods of time. These changes can lead to a higher connectivity and lower infiltration rates that could potentially increase the runoff generation, channel transmission losses and deep percolation in the landscapes of the area. While several efforts have been carried out trying to stop the woody plant encroachment in the area, we still need to make the scientific knowledge available to decision makers and the public in general. It is important to make them understand how the land management, livestock, land cover change and anthropogenic activities in general can have a deep impact in the biogeochemical processes of ecosystems. Ecosystems provide a set of good and services essential for the development and welfare of society. It represents a challenge to the scientific community to find the means and mechanisms to make the knowledge accessible for the decision makers and public in general in order to generate a real impact in society.

Data availability

During my entire Ph.D., I had the challenge to retrieve, process, organize and analyze a significant amount and variety of data. A fundamental aspect of scientific research is reproducibility and data sharing. Making the obtained data available for public access was an important task I had to achieve after successfully publishing my dissertation chapters.

For Chapters 2 and 3, the final versions of the processed data were published in the digital repository Zenodo. In the case of Chapter 2, three files were made available as "Water, energy and carbon fluxes and ancillary meteorological measurements of four

different urban landscapes in Phoenix, AZ during 2015", including a site information file, a file with meteorological variables and a file with fluxes (https://doi.org/10.5281/zenodo.3625224). Chapter 3 included two files with the final dataset of fluxes and meteorological data as well as precipitation data under the name "The North American Monsoon GPS Hydrometeorological Network 2017: Flux and Precipitation Data" (https://doi.org/10.5281/zenodo.3522331).

For Chapter 3, the Jornada Experimental Range LTER required specific ways to make the data publicly available. Initially, all data generated from research carried out within the Jornada Experimental Range needed to be uploaded to the EDI Data Portal. Data made available through EDI included "Precipitation data from four locations within the Tromble Weir experimental watershed, located at the Jornada Basin LTER site, 2010-ongoing" (https://portal.edirepository.org/nis/mapbrowse?scope=knb-lter-jrn&identifier=210338002), "Soil volumetric water content data from fifteen locations, 3 depths at each location, within the Tromble Weir experimental watershed at the Jornada Basin LTER site, 2010-ongoing" (https://portal.edirepository.org/nis/mapbrowse?scope=knb-lter-jrn&identifier=210338004) and "Standard meteorology and ancillary data from the Tromble Weir experimental watershed tower at the Jornada Basin LTER site, 2010-ongoing" (https://portal.edirepository.org/nis/mapbrowse?scope=knb-lter-jrn&identifier=210338006). Additional daily values of carbon and water fluxes and ancillary meteorological variables can be found in Zenodo as "Hydrologic data from long-term research catchments at the Santa Rita and Jornada Experimental Ranges"

(https://doi.org/10.5281/zenodo.4290771), which also includes data from the Santa Rita Experimental Range.

Half-hour values of water, energy and carbon fluxes and ancillary soil and meteorological variables were published in AmeriFlux, which is a network of sites measuring ecosystem CO_2, water, and energy fluxes in North, Central and South America. Data is available through their site (https://ameriflux.lbl.gov/) with a CC-BY-4.0 License, and the two sites are registered as "US-Jo2: Jornada Experimental Range Mixed Shrubland" (https://ameriflux.lbl.gov/sites/siteinfo/US-Jo2) and "US-SRS: Santa Rita Experimental Range Mesquite Savanna" (https://ameriflux.lbl.gov/sites/siteinfo/US-SRS).

Finally, this dissertation has a set of appendices with the data described before as well as with all the high frequency and original data used to obtain the final datasets. These appendices would serve as a digital repository of all the data obtaining through my Ph.D. efforts.

REFERENCES

Adams D.K., and Comrie A.C. 1997. The North American monsoon. *Bulletin of the American Meteorological Society*. 78: 2197-2213.

Ahlström, A., Raupach, M.R., Schurgers, G., Smith, B., Arneth, A., Jung, M., Reichstein, M., Canadell, J.G., Friedlingstein, P., Jain, A., Kato, E., Pulter, B., Sitch, S., Stocker, B., Viovy, N., Wang, Y.P., Wiltshire, A., Zaehle, S., and Zeng, N. 2015. The dominant role of semi-arid ecosystems in the trend and variability of the land CO_2 sink. *Science*. 348: 895-899.

Anderson C.A., and Vivoni E.R. 2016. Impact of land surface states within the flux footprint on daytime land-atmosphere coupling in two semiarid ecosystems of the southwestern US. *Water Resources Research*. 52(6), 4785-4800.

Anderson, J. 2018. LTER Weather Station daily summary climate data ver 113. Environmental Data Initiative. (Accessed 2021-06-01).

Anderson-Teixeira, K.J., Delong, J.P., Fox, A.M., Brese, D.A., and Litvak, M.E. 2011. Differential responses of production and respiration to temperature and moisture drive the carbon balance across a climatic gradient in New México. *Global Change Biology*. 17: 410-424.

Awal M.A., Ohta T, Matsumoto K., Toba T., Daikoku K., Hattori, S., Hiyama, T., and Park, H. 2010. Comparing the carbon sequestration capacity of temperate deciduous forests between urban and rural landscapes in central Japan. *Urban Forestry and Urban Greening*. 9(3): 261-270.

Baldocchi, D., Falge, E., Gu, L., Olson, R., Hollinger, D., Running, S., Anthoni, P., Bernhofer, Ch., Davis, K., Evans, R., Fuentes, J., Goldstein, A., Katul, G., Law, B., Lee, X., Malhi, Y., Meyers, T., Munger, W., Oechel, W., Paw U, K.T., Pilegaard, K., Schmid, H P., Valentini, R., Verma, S., Vesala, T., Wilson, K., and Wofsy, S. 2001. FLUXNET: A new tool to study the temporal and spatial variability of ecosystem-scale carbon dioxide, water vapor, and energy flux densities. *Bulletin of the American Meteorological Society*. 82(11): 2415-2434.

Baldocchi, D.D. 2003. Assessing ecosystem carbon balance: problems and prospects of the eddy covariance technique. *Global Change Biology*. 9(4): 479-492.

Baldocchi, D., 2008. 'Breathing'of the terrestrial biosphere: lessons learned from a global network of carbon dioxide flux measurement systems. *Australian Journal of Botany*. 56(1): 1-26.

Baldocchi, D., Falge, E., Gu, L., Olson, R., Hollinger, D., Running, S., Anthoni, P., Bernhofer, C., Davis, K., Evans, R. and Fuentes, J., 2001. FLUXNET: A new tool to study the temporal and spatial variability of ecosystem-scale carbon dioxide, water vapor, and energy flux densities. *Bulletin of the American Meteorological Society*. 82(11): 2415-2434.

Baldocchi, D.D., Xu, L., and Kiang, N. 2004. How plant functional-type, weather, seasonal drought, and soil physical properties alter water and energy fluxes of an oak–grass savanna and an annual grassland. *Agricultural and Forest Meteorology*. 123: 13-39.

Baldocchi, D., Chu, H., and Reichstein, M. 2018. Inter-annual variability of net and gross ecosystem carbon fluxes: A review. *Agricultural and Forest Meteorology*. 249: 520-533.

Barron-Gafford, G.A., Scott, R.L., Jenerette, G.D., Hamerlynck, E.P., and Huxman, T.E. 2013. Landscape and environmental controls over leaf and ecosystem carbon dioxide fluxes under woody plant expansion. *Journal of Ecology*. 101(6): 1471-1483.

Beer, C., Ciais, P., Reichstein, M., Baldocchi, D., Law, B.E., Papale, D., Soussana, J.-F. Ammann, C., Buchmann, N., Frank, D., Gianelle, D., Janssens, I.A., Knohl, A., Köstner, B., Moors, E., Roupsard, O., Verbeeck, H., Vesala, T., Williams, C.A., and Wohlfahrt, G. 2009. Temporal and among-site variability of inherent water use efficiency at the ecosystem level. *Global Biogeochemical Cycles*. 23(2): GB2018,

Bergeron, O., and Strachan, I.B. 2011. CO2 sources and sinks in urban and suburban areas of a northern mid-latitude city. *Atmospheric Environment*. 45(8): 1564-1573.

Biederman, J.A., Scott, R.L., Goulden, M.L., Vargas, R., Litvak, M.E., Kolb, T.E., Yépez, E.A., Oechel, W.C., Blanken, P.D., Bell, T.W., Garatuza-Payan, J., Maurer, G.E., Dore, S., and Burns, S.P., 2016. Terrestrial carbon balance in a drier world: the effects of water availability in southwestern North America. *Global Change Biology*. 22: 1867-1879.

Biederman, J.A., Scott, R.L., Bell, T.W., Bowling, D.R., Dore, S., Garatuza-Payan, J., Kolb, T.E., Krishnan, P., Krofcheck, D.J., Litvak, M.E., Maurer, G.E., Meyers, T.P., Oechel, W.C., Papuga, S.A., Ponce-Campos, G.E., Rodriguez, J.C., Smith, W.K., Vargas, R., Watts, C.J., Yépez, E.A., and Goulden, M.L. 2017. CO_2 exchange and evapotranspiration across dryland ecosystems of southwestern North America. *Global Change Biology*. 23(10): 4204-4221.

Biederman, J.A., Scott, R.L., Arnone III, J.A., Jasoni, R.L., Litvak, M.E., Moreo, M.T., Papuga, S.A., Ponce-Campos, G.E., Schreiner-McGraw, A.P., and Vivoni, E.R. 2018. Shrubland carbon sink depends upon winter water availability in the warm deserts of North America. *Agricultural and Forest Meteorology*. 249: 407-419.

Bjorkegren, A.B., Grimmond, C.S.B., Kotthaus, S., and Malamud, B.D. 2015. CO2 emission estimation in the urban environment: Measurement of the CO2 storage term. *Atmospheric Environment*. 122: 775-790.

Bowling, D.R., Bethers-Marchetti, S., Lunch, C.K., Grote, E.E., and Belnap, J. 2010. Carbon, water, and energy fluxes in a semiarid cold desert grassland during and following multiyear drought. *Journal of Geophysical Research: Biogeosciences*. 115(G4): G04026.

Brown, D.E. 1994. *Biotic Communities: southwestern United States and northwestern México*. University of Utah Press, Salt Lake City, UT, 342 pp.

Brunel, J.-P. 2009. Sources of water used by natural mesquite vegetation in a semi-arid region of northern México. *Hydrological Sciences Journal*. 54(2): 375-381.

Buckley, S.M., Mitchell, M.J., McHale, P.J., and Millard, G.D. 2016. Variations in carbon dioxide fluxes within a city landscape: Identifying a vehicular influence. *Urban Ecosystems*. 19(4): 1479-1498.

Budyko, M.I. 1974. *Climate and Life*. Academic Press, New York, NY, 508 pp.

Cable, D.R. 1977. Seasonal use of soil water by mature velvet mesquite. *Journal of Range Management*. 30: 4-11.

Cavazos, T., Comrie, A.C., and Liverman, D.M. 2002. Intraseasonal variability associated with wet monsoons in southeast Arizona. *Journal of Climate*. 15(17): 2477-2490.

Chow, W.T.L., Volo, T.J., Vivoni, E.R., Jenerette, G.D., and Ruddell, B.L. 2014. Seasonal dynamics of a suburban energy balance in Phoenix, Arizona. *International Journal of Climatology*. 34: 3863-3880.

Chow, W.T.L., Salamanca, F., Georgescu, M., Mahalov, A., Milne, J.F., and Ruddell, B.L. 2014. A multi-method and multi-scale approach for estimating city-wide anthropogenic heat fluxes. *Atmospheric Environment*. 99: 64-76.

Christen, A., Coops, N.C., Crawford, B.R., Kellett, R., Liss, K.N., Olchovski, I., Tooke, T.R., Van Der Laan, M., and Voogt, J.A. 2011. Validation of modeled carbon-dioxide emissions from an urban neighborhood with direct eddy-covariance measurements. *Atmospheric Environment*. 45(33):6057-69.

Churkina, G. 2008. Modeling the carbon cycle of urban systems. *Ecological Modelling*. 216(2): 107-113.

Clement R. EdiRe Data Software (Version 1.5.0.32), Sch. Of Geosci., Univ. of Edinburgh, Edinburgh, U.K. 1999. [Available at http://www.geos.ed.ac.uk/abs/research/micromet/EdiRe.]

Cook, B.I., and Seager, R. 2013. The response of the North American Monsoon to increased greenhouse gas forcing. *Journal of Geophysical Research: Atmospheres*. 118(4): 1690-1699.

Coutts, A.M., Beringer, J., and Tapper, N.J. 2007. Characteristics influencing the variability of urban CO_2 fluxes in Melbourne, Australia. *Atmospheric Environment*. 41(1): 51-62.

Crawford, B., Grimmond, C.S.B., and Christen, A. 2011. Five years of carbon dioxide fluxes measurements in a highly vegetated suburban area. *Atmospheric Environment*. 45(4): 896-905.

Crawford, B., and Christen, A. 2014. Spatial variability of carbon dioxide in the urban canopy layer and implications for flux measurements. *Atmospheric Environment*. 98: 308-322.

Crawford, B., Christen, A., and McKendry, I. 2016. Diurnal course of carbon dioxide mixing ratios in the urban boundary layer in response to surface emissions. *Journal of Applied Meteorology and Climatology*. 55(3), 507-529.

Davis, K.J., Deng, A., Lauvaux, T., Miles, N.L., Richardson, S.J., Sarmiento, D.P., Gurney, K.R., Hardesty, R.M., Bonin, T.A., Brewer, W.A., Lamb, B.K., Shepson, P.B., Harvey, R.M., Cambaliza, M.O., Sweeney, C., Turnbull, J.C., Whetstone, J., and Karion, A. 2017. The Indianapolis Flux Experiment (INFLUX): A test-bed for developing urban greenhouse gas emission measurements. *Elementa: Science of the Anthropocene*. 5: 21,

Delgado-Balbuena, J., Yépez, E.A., Paz-Pellat, F., Ángeles-Pérez, G., Aguirre-Gutiérrez, C., Alvarado-Barrientos, M.S., Arredondo, T., Ayala-Niño, F., Bullock, S.H., Castellanos, A.E., Cueva, A., Figueroa-Espinoza, B., Garatuza-Payan, J., Gonzales-del Castillo, E., González-Sosa, E., Guevara-Escobar, A., Hinojo-Hinojo, C., Paw U, K.T., Lizárraga-Celaya, C., Maya-Delgado, Y., Oechel, W., Pérez-Ruiz, E.R., Quesada-Avendaño, M., Robles-Zazueta, C.A., Rodríguez, J.C., Rojas-Robles, N.E., Tarín-Terrazas, T., Troyo-Diéguez, E., Uuh-Sonda, J., Vargas-Terminel, M.L., Vargas, R., Vega-Puga, M.G., Verduzco, V.S., Vivoni, E.R., and Watts, C.J. 2019. Base de datos de flujos verticales de dioxido de carbono en ecosistemas terrestres y costeros en México. *Elementos para Políticas Públicas*. 2(2): 93-108.

Delgado-Balbuena, J., Arredondo, J.T., Loescher, H.W., Pineda-Martinez, L.F., Carbajal, J.N., and Vargas, R. 2019. Seasonal precipitation legacy effects determine the carbon balance of a semiarid grassland. *Journal of Geophysical Research: Biogeosciences*. 124(4): 987-1000.

Douglas, M.W., Maddox, R.A., Howard, K., and Reyes, S. 1993. The Mexican monsoon. *Journal of Climate*. 6(8): 1665-1677.

Duniway, M.C., Herrick, J.E., and Monger, H.C. 2007. The high water-holding capacity of petrocalcic horizons. *Soil Science Society of America Journal*. 71(3): 812-819.

Duniway, M.C., Herrick, J.E., and Monger, H.C. 2010. Spatial and temporal variability of plant-available water in calcium carbonate-cemented soils and consequences for arid ecosystem resilience. *Oecologia*. 163(1): 215-226.

Eamus, D., Zolfaghar, S., Villalobos-Vega, R., Cleverly, J., and Huete, A. 2015. Groundwater-dependent ecosystems: Recent insights from satellite and field-based studies. *Hydrology and Earth System Sciences*. 19: 4229-4256.

Feigenwinter, C., Vogt, R., and Christen, A. Eddy covariance measurements over urban areas. In: Aubinet, M., Vesala, T. and Papale, D. (eds.) *Eddy Covariance*. Springer Atmospheric Sciences. Springer, Dordrecht, Netherlands. 2012.

Flanagan, L.B., and Flanagan, J.E. 2018. Seasonal controls on ecosystem-scale CO_2 and energy exchange in a Sonoran Desert characterized by the saguaro cactus (Carnegiea gigantea). *Oecologia*. 187(4): 977-994.

Flerchinger, G.N., Fellows, A.W., Seyfried, M.S., Clark, P.E., and Lohse, K.A. 2020. Water and carbon fluxes along an elevational gradient in a sagebrush ecosystem. *Ecosystems*. 23(2): 246-263.

Foken, T. 2006. 50 Years of the Monin-Obukhov similarity theory. *Boundary Layer Meteorology*. 119: 431-447.

Forzieri, G., Castelli, F., and Vivoni, E.R. 2011. Vegetation dynamics within the North American monsoon region. *Journal of Climate*. 24(6): 1763-1783.

Forzieri, G., Feyen, L., Cescatti, A., and Vivoni, E.R. 2014. Spatial and temporal variations in ecosystem response to monsoon precipitation variability in southwestern North America. *Journal of Geophysical Research: Biogeosciences*. 119(10): 1999-2017.

Gately, C.K., Hutyra, L.R., Wing, I.S., and Brondfield, M.N. 2013. A bottom up approach to on-road CO_2 emissions estimates: Improved spatial accuracy and applications for regional planning. *Environmental Science and Technology*. 47(5): 2423-2430.

Gately, C.K., Hutyra, L.R., and Wing, I.S. 2015. Cities, traffic, and CO_2: A multidecadal assessment of trends, drivers, and scaling relationships. *Proceedings of the National Academy of Sciences*. 112(16): 4999-5004.

Georgescu, M., Mahalov, A., and Moustaoui, M. 2012. Seasonal hydroclimatic impacts of Sun Corridor expansion. *Environmental Research Letters*. 7(3): 034026.

Gibbens, R.P., and Lenz, J.M. 2001. Root systems of some Chihuahuan Desert plants. *Journal of Arid Environments*. 49(2): 221-263.

Gibbens, R.P., McNeely, R.P., Havstad, K.M., Beck, R.F., and Nolen, B. 2005. Vegetation changes in the Jornada Basin from 1858 to 1998. *Journal of Arid Environments*. 61: 651-668.

Gile, L.H., Gibbens, R.P., and Lenz, J.M. 1998. Soil-induced variability in root systems of creosotebush (Larrea tridentata) and tarbush (Flourensia cernua). *Journal of Arid Environments*. 39(1): 57-78.

Goodrich, D.C., Williams, D.G., Unkrich, C.L., Hogan, J.F., Scott, R.L., Hultine, K.R., Pool, D., Coes, A.L., and Miller, S. 2004. Comparison of methods to estimate ephemeral channel recharge, Walnut Gulch, San Pedro River Basin, Arizona. In: Phillips, F., Hogan, J., and Scanlon, B. (Eds.), *Groundwater recharge in a desert environment, The southwestern United States*. Washington, DC, American Geophysical Union.

Grimmond, C.S.B., King, T.S., Cropley, F.D., Nowak, D.J., and Souch, C. 2002. Local-scale fluxes of carbon dioxide in urban environments: methodological challenges and results from Chicago. *Environmental Pollution*. 116: S243-S254.

Grimmond, C.S.B., Salmond, J.A., Oke, T.R., Offerle, B., and Lemonsu, A. 2004. Flux and turbulence measurements at a densely built-up site in Marseille: Heat, mass (water and carbon dioxide), and momentum. *Journal of Geophysical Research - Atmospheres*. 109(D24): D24101.

Grimmond, C.S.B. 2006. Progress in measuring and observing the urban atmosphere. *Theoretical and Applied Climatology*. 84: 3-22.

Grimmond, C.S.B., and Christen, A. 2012. Flux measurements in urban ecosystems. *Fluxletter: Newsletter of Fluxnet*. 5(1): 1-8.

Gurney, K.R., Liang, J., O'Keeffe, D., Patarasuk, R., Hutchins, M., Huang, J., Rao, P., and Song, Y. 2019. Comparison of global downscaled versus bottom-up fossil fuel CO2 emissions at the urban scale in four US urban areas. *Journal of Geophysical Research - Atmospheres*. 124: 2823-2840.

Gutzler, D.S. 2004. An index of interannual precipitation variability in the core of the North American monsoon region. *Journal of Climate*. 17: 4473-4480.

Hardiman, B.S., Wang, J.A., Hutyra, L.R., Gately, C.K., Getson, J.M., and Friedl, M.A. Accounting for urban biogenic fluxes in regional carbon budgets. *Science of The Total Environment*. 2017;592: 366-372.

Helfter, C., Tremper, A.H., Halios, C.H., Kotthaus, S., Bjorkegren, A., Grimmond, C.S.B., Barlow, J.F., and Nemitz, E. 2016. Spatial and temporal variability of urban fluxes of methane, carbon monoxide and carbon dioxide above London, UK. *Atmospheric Chemistry and Physics*. 16(16): 10543-10557.

Hemond, H.F., and Fechner, E.J. *Chemical fate and transport in the environment*, Chapter 4 The Atmosphere. 3rd Edition. Academic Press. 2015. Pp. 311-454.

Higgins, R.W., Chen, Y., and Douglas, A.V. 1999. Interannual variability of the North American warm season precipitation regime. *Journal of Climate*. 12(3): 653-680.

Hiller, R.V., McFadden, J.P., and Kljun, N. 2011. Interpreting CO_2 fluxes over a suburban lawn: the influence of traffic emissions. *Boundary Layer Meteorology*. 138(2), 215-230.

Hinojo-Hinojo, C., Castellanos, A.E., Rodríguez, J.C., Delgado-Balbuena, J., Romo-León, J.R., Celaya-Michel, H., and Huxman, T.E. 2016. Carbon and water fluxes in an exotic Buffelgrass savanna. *Rangeland Ecology and Management*. 69(5): 334-341.

Hinojo-Hinojo, C., Castellanos, A.E., Huxman, T., Rodriguez, J.C., Vargas, R., Romo-León, J. R., and Biederman, J.A. 2019. Native shrubland and managed buffelgrass savanna in drylands: Implications for ecosystem carbon and water fluxes. *Agricultural and Forest Meteorology*. 268: 269-278.

Hirano, T., Sugawara, H., Murayama, S., and Kondo, H. 2015. Diurnal variation of CO_2 flux in an urban area of Tokyo. *Sola*. 11, 100-103.

Hsu, J.S., Powell, J., and Adler, P.B. 2012. Sensitivity of mean annual primary production to precipitation. *Global Change Biology*. 18(7): 2246-2255.

Hutyra, L.R., Duren, R., Gurney, K.R., Grimm, N., Kort, E.A., Larson, E., and Shrestha, G. 2014. Urbanization and the carbon cycle: Current capabilities and research outlook from the natural sciences perspective. *Earth's Future*. 2(10): 473-495.

Huenneke, L.F., Anderson, J.P., Remmenga, M., and Schlesinger, W.H., 2002. Desertification alters patterns of aboveground net primary production in Chihuahuan ecosystems. *Global Change Biology*. 8: 247-264.

Hui, D., Luo, Y., and Katul, G. 2003. Partitioning interannual variability in net ecosystem exchange between climatic variability and functional change. *Tree Physiology*. 23(7): 433-442.

Huxman, T.E., Turnipseed, A.A., Sparks, J.P., Harley, P.C., and Monson, R.K. 2003. Temperature as a control over ecosystem CO_2 fluxes in a high-elevation, subalpine forest. *Oecologia*. 134(4): 537-546.

Huxman, T.E., Snyder, K.A., Tissue, D., Leffler, A.J., Ogle, K., Pockman, W.T., Sandquist, D.R., Potts, D.L., and Schwinning, S. 2004a. Precipitation pulses and carbon fluxes in semiarid and arid ecosystems. *Oecologia*. 141: 254-268.

Huxman, T.E., Smith, M.D., Fay, P.A., Knapp, A.K., Shaw, R., Loik, M.E., Smith, S.D., Tissue, D.T., Zak, J.C., Weltzin, J.F., Pockman, W.T., Sala, O.E., Haddad, B.M., Harte, J., Koch, G.W., Schwinning, S., Small, E.E., and Williams, D.G. 2004b. Convergence across biomes to a common rain-use efficiency. *Nature*. 429: 651-654 .

Idso, C.D., Idso, S.B., and Balling Jr., R.C. 2002. Seasonal and diurnal variations of near-surface atmospheric CO_2 concentration within a residential sector of the urban CO_2 dome of Phoenix, AZ, USA. *Atmospheric Environment*. 36(10): 1655-1660.

INEGI. 2016. Conjunto de Datos Vectoriales de Uso de Suelo y Vegetación. Escala 1:250 000. Serie VI. Edición: 1. Instituto Nacional de Estadística y Geografía. Aguascalientes, México.

Järvi, L., Nordbo, A., Junninen, H., Riikonen, A., Moilanen, J., Nikinmaa, E., and Vesala, T. 2012. Seasonal and annual variation of carbon dioxide surface fluxes in Helsinki, Finland, in 2006–2010. *Atmospheric Chemistry and Physics*. 12(18): 8475-8489.

Järvi, L., Havu, M., Ward, H.C., Bellucco, V., McFadden, J.P., Toivonen, T., Heikinheimo, V., Kolari, P., Riikonen, A., and Grimmond, C.S.B. 2019. Spatial modeling of local-scale biogenic and anthropogenic carbon dioxide emissions in Helsinki. *Journal of Geophysical Research: Atmospheres*. 124(15), 8363-8384.

Jia, X., Zha, T. S., Wu, B., Zhang, Y. Q., Gong, J. N., Qin, S.G., Chen, G.P., Qian, D., Kellomäki, S., and Peltola, H. 2014. Biophysical controls on net ecosystem CO2 exchange over a semiarid shrubland in northwest China. *Biogeosciences*. 4679.

Jia, X., Zha, T., Gong, J., Wang, B., Zhang, Y., Wu, B., Qin, S., and Peltola, H. 2016. Carbon and water exchange over a temperate semi-arid shrubland during three years of contrasting precipitation and soil moisture patterns. *Agricultural and Forest Meteorology*. 228: 120-129.

Jia, X., Mu, Y., Zha, T., Wang, B., Qin, S., and Tian, Y. 2020. Seasonal and interannual variations in ecosystem respiration in relation to temperature, moisture, and productivity in a temperate semi-arid shrubland. *Science of the Total Environment*. 709: 136210.

Keeling, C.D., Chin, J.F.S., and Whorf, T.P. 1996. Increased activity of northern vegetation inferred from atmospheric CO_2 measurements. *Nature*. 382(6587): 146-149.

Kljun, N., Calanca, P., Rotach, M.W., and Schmid, H.P. 2015. A simple two-dimensional parameterisation for Flux Footprint Prediction (FFP). *Geoscientific Model Development*. 8(11): 3695-3713.

Knowles, J.F., Scott, R.L., Minor, R.L., and Barron-Gafford, G.A. 2020. Ecosystem carbon and water cycling from a sky island montane forest. *Agricultural and Forest Meteorology*. 281: 107835.

Ko, A., Mascaro, G., and Vivoni, E.R. 2019. Strategies to improve and evaluate physics-based hyperresolution hydrologic simulations at regional basin scales. *Water Resources Research*. 55(2): 1129-1152.

Koerner, B., and Klopatek, J. 2002. Anthropogenic and natural CO_2 emission sources in an arid urban environment. *Environmental Pollution*. 116(1): S45-S51.

Koerner, B., and Klopatek, J. 2010. Carbon fluxes and nitrogen availability along an urban-rural gradient in a desert landscape. *Urban Ecosystems*. 13(1): 1-21.

Kordowski, K., and Kuttler, W. 2010. Carbon dioxide fluxes over an urban park area. *Atmospheric Environment*. 44(23): 2722-2730.

Kormann, R., and Meixner, F.X. 2001. An analytical footprint model for non-neutral stratification. *Boundary Layer Meteorology*. 99(2): 207-224.

Kotthaus, S., and Grimmond C.S.B. Identification of micro-scale anthropogenic CO_2, heat and moisture sources–processing eddy covariance fluxes for a dense urban environment. *Atmospheric Environment*. 57: 301-316.

Kurc, S.A., and Small, E.E. 2004. Dynamics of evapotranspiration in semiarid grassland and shrubland ecosystems during the summer monsoon season, central New México. *Water Resources Research*. 40: W09305.

Kurc, S.A., and Small, E.E. 2007. Soil moisture variations and ecosystem-scale fluxes of water and carbon in semiarid grassland and shrubland. *Water Resources Research*. 43(6): W06416.

Kurc, S.A., and Benton, L.M. 2010. Digital image-derived greenness links deep soil moisture to carbon uptake in a creosotebush-dominated shrubland. *Journal of Arid Environments*. 74: 585-594.

Lagergren, F., Lindroth, A., Dellwik, E., Ibrom, A., Lankreijer, H., Launiainen, S., Molder, M., Kolari, P., Pilegaard, K., and Vesala, T. 2008. Biophysical controls on CO_2 fluxes of three Northern forests based on long-term eddy covariance data. *Tellus B: Chemical and Physical Meteorology*. 60(2): 143-152.

Laio, F., Tamea, S., Ridolfi, L., D'Odorico, P., and Rodriguez-Iturbe, I. 2009. Ecohydrology of groundwater-dependent ecosystems: 1. Stochastic water table dynamics. *Water Resources Research*. 45: W05419.

Lauvaux, T., Miles, N.L., Deng, A., Richardson, S.J., Cambaliza, M.O., Davis, K.J., Gaudet, B., Hurney, K.R., Huang, J., O'Keefe, D., Song, Y., Karion, A., Oda, T., Patarasuk, R., Razlivanov, I., Sarmiento, D., Shepson, P., Sweeney, C., Turnbull, J., and Wu, K. 2016. High-resolution atmospheric inversion of urban CO_2 emissions during the dormant season of the Indianapolis Flux Experiment (INFLUX). *Journal of Geophysical Research: Atmospheres*. 121(10). 5213-5236.

Lazzarini, M., Molini, A., Marpu, P.R., Ouarda, T.B.M.J., and Ghedira, H. 2015. Urban climate modifications in hot desert cities: The role of land cover, local climate, and seasonality. *Geophysical Research Letters*. 42: 9980–9989

Li, G., Han, H., Du, Y., Hui, D., Xia, J., Niu, S., Li, X., and Wan, S. 2017. Effects of warming and increased precipitation on net ecosystem productivity: A long-term manipulative experiment in a semiarid grassland. *Agricultural and Forest Meteorology*. 232: 359-366.

Lietzke, B., and Vogt, R. 2013. Variability of CO2 concentrations and fluxes in and above an urban street canyon. *Atmospheric Environment*. 74: 60-72.

Lietzke, B., Vogt, R., Feigenwinter, C., and Parlow, E. 2015. On the controlling factors for the variability of carbon dioxide flux in a heterogeneous urban environment. *International Journal of Climatology*, 35(13), 3921-3941.

Liu, H.Z., Feng, J.W., Järvi, L., and Vesala, T. 2012. Four-year (2006–2009) eddy covariance measurements of CO_2 flux over an urban area in Beijing. *Atmospheric Chemistry and Physics*. 12(17): 7881-7892.

Liu, J., Ma, X., Duan, Z., Jiang, J., Reichstein, M., and Jung, M. 2020. Impact of temporal precipitation variability on ecosystem productivity. *Wiley Interdisciplinary Reviews: Water*. 7(6): e1481.

Lizarraga-Celaya, C., Watts, C.J., Rodríguez, J.C., Garatuza-Payan, J., Scott, R.L., and Saíz-Hernandez, J. 2010. Spatio-temporal variations in surface characteristics over the North American monsoon region. *Journal of Arid Environments*. 74(5): 540-548.

Lloyd, J., and Taylor, J. A. 1994. On the temperature dependence of soil respiration. *Functional Ecology*. 8(3): 315-323.

Lohse, K.A., Brooks, P.D., McIntosh, J.C., Meixner, T., and Huxman, T.E. 2009. Interactions between biogeochemistry and hydrologic systems. *Annual Review of Environment and Resources*. 34: 65-96.

Ma, S., Baldocchi, D.D., Xu, L., and Hehn, T. 2007. Inter-annual variability in carbon dioxide exchange of an oak/grass savanna and open grassland in California. *Agricultural and Forest Meteorology*. 147(3-4): 157-171.

Mann, H.B., and Whitney, D.R., 1947. On a test of whether one of two random variables is stochastically larger than the other. *The annals of mathematical statistics*. 18(1): 50-60.

Martinet, M.C., Vivoni, E.R., Cleverly, J.R., Thibault, J.R., Schuetz, J.F., and Dahm, C.N. 2009. On groundwater fluctuations, evapotranspiration and understory removal in riparian corridors. *Water Resources Research*. 45: W05425.

Mascaro, G., Vivoni, E.R., Gochis, D.J., Watts, C.J., and Rodríguez, J.C. 2014. Temporal downscaling and statistical analysis of rainfall across a topographic transect in northwest México. *Journal of Applied Meteorology and Climatology*. 53(4): 910-927.

Mascaro, G., and Vivoni, E.R. 2016. On the observed hysteresis in field-scale soil moisture variability and its physical controls. *Environmental Research Letters*. 11(8): 084008.

Massman, W.J. 2001. Reply to comment by Rannik on: "A simple method for estimating frequency response corrections for eddy covariance systems". *Agricultural and Forest Meteorology*. 107: 247-251.

McHale, M.R., Hall, S.J., Majumdar, A., and Grimm, N.B. 2017. Carbon lost and carbon gained: a study of vegetation and carbon trade-offs among diverse land uses in Phoenix, Arizona. *Ecological Applications*. 27(2): 644-661.

McKenna, O.P., and Sala, O.E. 2018. Groundwater recharge in desert playas: current rates and future effects of climate change. *Environmental Research Letters*. 13: 014025.

Méndez-Barroso, L.A., Vivoni, E.R., Watts, C.J., and Rodríguez, J.C. 2009. Seasonal and interannual relation between precipitation, surface soil moisture and vegetation dynamics in the North American monsoon region. *Journal of Hydrology*. 377: 59-70.

Méndez-Barroso, L.A., and Vivoni, E.R. 2010. Observed shifts in land surface conditions during the North American monsoon: Implications for a vegetation-rainfall feedback mechanism. *Journal of Arid Environments*. 74(5): 549-555.

Méndez-Barroso, L.A., Vivoni, E.R., Robles-Morua, A., Mascaro, G., Yépez, E.A., Rodríguez, J.C., Watts, C.J., Garatuza-Payan, J., and Saíz-Hernandez, J. 2014. A modeling approach reveals differences in evapotranspiration and its partitioning in two semiarid ecosystems in northwest México. *Water Resources Research*. 50(4): 3229-3252.

Mills, G. 2007. Cities as agents of global change. *International Journal of Climatology*. 27: 1849-1857.

Misson, L., Baldocchi, D.D., Black, T.A., Blanken, P.D., Brunet, Y., Yuste, J.C., Dorsey, J.R., Falk, M., Granier, A., Irvine, M.R., Jarosz, N., Lamaud, E., Launiainen, S., Law, B.E., Longdoz, B., Loustau, D., McKay, M., Paw, K.T., Vesala, T., Vickers, D., Wilson, K.B., and Goldsteing, A.H. 2007. Partitioning forest carbon fluxes with overstory and understory eddy-covariance measurements: A synthesis based on FLUXNET data. *Agricultural and Forest Meteorology*. 144(1-2): 14-31.

Moncrieff, J.B., Massheder, J.M., De Bruin, H., Elbers, J., Friborg, T., Heusinkveld, B., Kabat, P., Scott, S., Soegaard, H., and Verhoef, A. 1997. A system to measure surface fluxes of momentum, sensible heat, water vapour and carbon dioxide. *Journal of Hydrology*. 188: 589-611.

Moncrieff, J., Clement, R., Finnigan, J., and Meyers, T. 2004. Averaging, detrending, and filtering of eddy covariance time series. In *Handbook of Micrometeorology* (pp. 7-31). Springer, Dordrecht.

Monson, R.K., Sparks, J.P., Rosenstiel, T.N., Scott-Denton, L.E., Huxman, T.E., Harley, P.C., Turnipseed, A.A., Burns, S.P., Backlund, B., and Hu, J. 2005. Climatic influences on net ecosystem CO_2 exchange during the transition from wintertime carbon source to springtime carbon sink in a high-elevation, subalpine forest. *Oecologia*. 146(1): 130-147.

Moore, C.J. 1986. Frequency response corrections for eddy correlation systems. *Boundary Layer Meteorology*. 37(1-2): 17-35.

Moriwaki, R., and Kanda, M. 2004. Seasonal and diurnal fluxes of radiation, heat, water vapor, and carbon dioxide over a suburban area. *Journal of Applied Meteorology*. 43(11): 1700-1710.

Muldavin, E.H., Moore, D.I., Collins, S.L., Wetherill, K.R., and Lightfoot, D.C. 2008. Aboveground net primary production dynamics in a northern Chihuahuan Desert ecosystem. *Oecologia*. 155: 123-132.

Nakai, T., and Shimoyama, K. 2012. Ultrasonic anemometer angle of attack errors under turbulent conditions. *Agricultural and Forest Meteorology*. 162: 14-26.

Ng, B.J.L., Hutyra, L.R., Nguyen, H., Cobb, A.R., Kai, F.M., Harvey, C., and Gandois, L. 2015. Carbon fluxes from an urban tropical grassland. *Environmental Pollution*. 203: 227-234.

Noy-Meir, I. 1973. Desert ecosystems: environment and producers. *Annual Review of Ecology and Systematics*. 4(1): 25-51.

Oke, T.R. 1988. The urban energy balance. *Progress in Physical Geography*. 12: 471-508.

Ogle, K., and Reynolds, J.F. 2004. Plant responses to precipitation in desert ecosystems: integrating functional types, pulses, thresholds, and delays. *Oecologia*. 141(2): 282-294.

ORNL DAAC. 2018. MODIS and VIIRS Land Products Global Subsetting and Visualization Tool. ORNL DAAC, Oak Ridge, Tennessee, USA. Accessed April 04, 2019. Subset obtained for MOD13Q1 product at 29.8297N,110.5032W, time period: 2000-02-18 to 2019-03-06, and subset size: 100.25 x 100.25 km. https://doi.org/10.3334/ORNLDAAC/1379.

Paco, T.A., David, T.S., Henriques, M.O., Pereira, J.S., Valente, F., Banza, J., Pereira, F.L., Pinto, C., and David, J.S. 2009. Evapotranspiration from a Mediterranean evergreen oak savannah: The role of trees and pasture. *Journal of Hydrology*. 369: 98-106.

Papale, D., Reichstein, M., Aubinet, M., Canfora, E., Bernhofer, C., Kutsch, W., Longdoz, B., Rambal, S., Valentini, R., Vesala, T., and Yakir, D. 2006. Towards a standardized processing of net ecosystem exchange measured with eddy covariance technique: algorithms and uncertainty estimation. *Biogeosciences*. 3(4): 571-583.

Park, C., and Schade, G.W. 2016. Anthropogenic and Biogenic Features of Long-Term Measured CO_2 Flux in North Downtown Houston, Texas. *Journal of Environmental Quality*. 45(1), 253-265.

Pascale, S., Carvahlo, L.M.V., Adams, D.K., Castro, C.L., and Cavalcanti, I.F.A. 2019. Current and future variations of the monsoons of the Americas in a warming climate. *Current Climate Change Reports*. 5(3): 125-144.

Pataki, D.E., Alig, R.J., Fung, A.S., Golubiewski, N.E., Kennedy, C.A., McPherson, E.G., Nowak, D.J., Pouyat, R.V., and Romero Lankao, P. 2006. Urban ecosystems and the North American carbon cycle. *Global Change Biology*. 12(11): 2092-2102.

Paw U, K.T., Baldocchi, D.D., Meyers, T.P., and Wilson, K.B. 2000. Correction of eddy-covariance measurements incorporating both advective effects and density fluxes. *Boundary Layer Meteorology*. 97: 487-511.

Pawlak, W., Fortuniak, K., and Siedlecki, M. 2011. Carbon dioxide flux in the centre of Łódź, Poland—analysis of a 2-year eddy covariance measurement data set. *International Journal of Climatology*. 31(2), 232-243.

Peel, M.C., Finlayson, B.L., and McMahon, T.A. 2007. Updated world map of the Köppen-Geiger climate classification. *Hydrology and Earth Systems Science*. 11: 1633-1644.

Pérez-Ruiz, E.R., Garatuza-Payan, J., Watts, C.J., Rodriguez, J.C., Yépez, E.A., and Scott, R.L. 2010. Carbon dioxide and water vapour exchange in a tropical dry forest as influenced by the North American Monsoon System (NAMS). *Journal of Arid Environments*. 74(5): 556-563.

Pérez-Ruiz, E.R., and Vivoni, E.R. 2019. The North American Monsoon GPS Hydrometeorological Network 2017: Flux and Precipitation Data [Data set]. Zenodo. http://doi.org/10.5281/zenodo.3522331.

Pérez-Ruiz, E.R., Vivoni, E.R., Yépez, E.A., Rodríguez, J.C., Gochis, D.J., Robles-Morua, A., Delgado-Balbuena, J., and Adams, D.K. 2021. Landscape controls on water-energy-carbon fluxes across different ecosystems during the North American Monsoon. *Journal of Geophysical Research: Biogeosciences*. 126(5): e2020JG005809.

Peters, E.B., and McFadden, J.P. 2012. Continuous measurements of net CO_2 exchange by vegetation and soils in a suburban landscape. *Journal of Geophysical Research: Biogeosciences*. 117(G3).

Peters, D.P.C., Savoy, H.M., Stillman, S., Huang, H., Hudson, A.R., Sala, O.E., and Vivoni, E.R. 2021. Plant species richness in multiyear wet and dry periods in the Chihuahuan Desert. *Climate*. 9(8): 130.

Petrie, M.D., Collins, S.L., Swann, A.M., Ford, P.L., and Litvak, M.E. 2015. Grassland to shrubland state transitions enhance carbon sequestration in the northern Chihuahuan Desert. *Global Change Biology*. 21: 1226-1235.

Pierini, N.A., Vivoni, E.R., Robles-Morua, A., Scott, R.L., and Nearing, M.A. 2014. Using observations and a distributed hydrologic model to explore runoff thresholds linked with mesquite encroachment in the Sonoran Desert. *Water Resources Research*. 50(10): 8191-8215.

Potts, D. L., Scott, R. L., Cable, J. M., Huxman, T.E., and Williams, D.G. 2008. Sensitivity of mesquite shrubland CO_2 exchange to precipitation in contrasting landscape settings. *Ecology*. 89(10): 2900-2910.

Potts, D. L., Scott, R. L., Bayram, S., and Carbonara, J. 2010. Woody plants modulate the temporal dynamics of soil moisture in a semi-arid mesquite savanna. *Ecohydrology*. 3(1): 20-27.

Poulter, B., Frank, D., Ciais, P., Myneni, R.B., Andela, N., Bi, J., Broquet, G., Canadell, J.G., Chevallier, F., Liu, Y.Y., Running, S. W., Sitch, S., and van der Werf, G.R. 2014. Contribution of semi-arid ecosystems to interannual variability of the global carbon cycle. *Nature*. 509(7502): 600-603.

Ramamurthy, P., and Pardyjak, E.R. 2011. Toward understanding the behavior of carbon dioxide and surface energy fluxes in the urbanized semi-arid Salt Lake Valley, Utah, USA. *Atmospheric Environment*. 45(1): 73-84.

Ramamurthy, P., and Pardyjak, E.R. 2015. Turbulent transport of carbon dioxide over a highly vegetated suburban neighbourhood. *Boundary Layer Meteorology*. 157(3): 461-479.

Raz-Yaseef, N., Yakir, D., Schiller, G., and Cohen, S. 2012. Dynamics of evapotranspiration partitioning in a semi-arid forest as affected by temporal rainfall patterns. *Agricultural and Forest Meteorology*. 157:77-85.

Reichmann, L.G., Sala, O.E., and Peters, D.P.C. 2013. Precipitation legacies in desert-grassland primary production occur through previous-year tiller density. *Ecology*. 94: 435-443.

Reichstein, M., Falge, E., Baldocchi, D., Papale, D., Aubinet, M., Berbigier, P., Bernhofer, C., Buchmann, N., Gilmanov, T., Granier, A., Grünwald, T., Havránková, K., Ilvesniemi, H., Janous, D., Knohl, A., Laurila, T., Lohila, A., Loustau, D., Matteucci, G., Meyers, T., Miglietta, F., Ourcival, J-M., Pumpanen, J., Rambal, S., Rotenberg, E., Sanz, M., Tenhunen, J., Seufert, G., Vaccari, F., Vesala, T., Yakir, D., and Valentini, R. 2005. On the separation of net ecosystem exchange into assimilation and ecosystem respiration: Review and improved algorithm. *Global Change Biology*. 11(9): 1424-1439.

Reynolds, J.F., Kemp, P.R., and Tenhunen, J.D. 2000. Effects of long-term rainfall variability on evapotranspiration and soil water distribution in the Chihuahuan desert: a modeling analysis. *Plant Ecology*. 150: 145-159.

Reynolds, J.F., Kemp, P.R., Ogle, K., and Fernández, R.J. 2004. Modifying the 'pulse–reserve' paradigm for deserts of North America: precipitation pulses, soil water, and plant responses. *Oecologia*. 141(2): 194-210.

Richardson, S.J., Miles, N.L., Davis, K.J., Lauvaux, T., and Martins, D. 2017. Tower measurement network of CO_2, CO, and CH_4 in support of the Indianapolis FLUX (INFLUX) Experiment. *Elementa: Science of the Anthropocen*. 2017;5: p.59.

Rodriguez-Iturbe, I., Porporato, A., Laio, F., and Ridolfi, L. 2001. Intensive or extensive use of soil moisture: plant strategies to cope with stochastic water availability. *Geophysical Research Letters*. 28(23): 4495-4497.

Rodríguez-Robles, U., Arredondo, T., Huber-Sannwald, E., and Yépez, E.A. 2017. Application of geophysical tools for tree root studies in forest ecosystems with complex soils. *Biogeosciences*. 14: 5343-5357.

Rojas-Robles, N.E., Garatuza-Payán, J., Álvarez-Yépiz, J.C., Sánchez-Mejía, Z.M., Vargas, R., and Yépez, E.A. 2020. Environmental controls on carbon and water fluxes in an old-growth tropical dry forest. Journal of Geophysical Research: *Biogeosciences*. 125(8): e2020JG005666.

Roth, M., Jansson, C., and Velasco, E. 2016. Multi-year energy balance and carbon dioxide fluxes over a residential neighbourhood in a tropical city. *International Journal of Climatology*. 37(5): 2679-2698.

Saito, M., Kato, T., and Tang, Y. 2009. Temperature controls ecosystem CO_2 exchange of an alpine meadow on the northeastern Tibetan Plateau. *Global Change Biology*, 15(1): 221-228.

Sala, O.E., Parton, W.J., Joyce, L.A., and Lauenroth, W.K. 1988. Primary production of the central grassland region of the United States. *Ecology*. 69: 40-45.

Sala, O.E., Gherardi, L.A., Reichmann, L., Jobbágy, E., and Peters, D.P.C. 2012. Legacies of precipitation fluctuations on primary production: Theory and data synthesis. *Philosophical Transactions of the Royal Society B*. 367: 3135-3144.

Sargent M., Barrera, Y., Nehrkorn, T., Hutyra, L.R., Gately, C.K., Jones, T., McKain, K., Sweeney, C., Hegarty, J., Hardiman, B., Wang, J.A. and Wofsy, S.C. 2018. Anthropogenic and biogenic CO_2 fluxes in the Boston urban region. *Proceedings of the National Academy of Sciences*. 115(29): 7491-7496.

Schenk, H.J., and Jackson, R.B. 2002. The global biogeography of roots. *Ecological Monographs*. 72(3): 311-328.

Schmid, H.P. 1994. Source areas for scalars and scalar fluxes. *Boundary Layer Meteorology*. 67(3): 293-318.

Schmid, H.P., Grimmond, C.S.B., Cropley, F., Offerle, B., and Su, H.B. 2000. Measurements of CO_2 and energy fluxes over a mixed hardwood forest in the mid-western United States. *Agricultural and Forest Meteorology*. 103(4): 357-374.

Schmidli, R.J., and Jamison, A. 1996. Climate of Phoenix, Arizona. NOAA.

Schmutz, M., Vogt, R., Feigenwinter, C., and Parlow, E. 2016. Ten years of eddy covariance measurements in Basel, Switzerland: Seasonal and interannual variabilities of urban CO_2 mole fraction and flux. *Journal of Geophysical Research - Atmospheres*. 121(14): 8649-8667.

Schreiner-McGraw, A.P., Vivoni, E.R., Mascaro, G., and Franz, T.E. 2016. Closing the water balance with cosmic-ray soil moisture measurements and assessing their relation with evapotranspiration in two semiarid watersheds. *Hydrology and Earth System Sciences*. 20: 329-345.

Schreiner-McGraw, A.P., and Vivoni, E.R. 2017. Percolation observations in an arid piedmont watershed and linkages to historical conditions in the Chihuahuan Desert. *Ecosphere*. 8(11): e02000.

Schreiner-McGraw, A.P., and Vivoni, E.R. 2018. On the sensitivity of hillslope runoff and channel transmission losses in arid piedmont slopes. *Water Resources Research*. 54(7): 4498-4518.

Schreiner-McGraw, A.P., Vivoni, E.R., Ajami, H., Sala, O.E., Throop, H.L., and Peters, D.P.C. 2020. Woody plant encroachment has a larger impact than climate change on dryland water budgets. *Scientific Reports*. 10(1): 8112.

Schwinning, S. 2010. The ecohydrology of roots in rocks. *Ecohydrology*. 3(2): 238-245.

Scott, R.L. 2010. Using watershed water balance to evaluate the accuracy of eddy covariance evaporation measurements for three semiarid ecosystems. *Agricultural and Forest Meteorology*. 150(2): 219-225.

Scott, R.L., and Biederman, J.A. 2017. Partitioning evapotranspiration using long-term carbon dioxide and water vapor fluxes. *Geophysical Research Letters*. 44(13): 6833-6840.

Scott, R.L., and Biederman, J.A. 2019. Critical zone water balance over 13 years in a semiarid savanna. *Water Resources Research*. 55(1): 574-588.

Scott, R.L., Edwards, E.A., Shuttleworth, W.J., Huxman, T.E., Watts, C.J., and Goodrich, D.C. 2004. Interannual and seasonal variation in fluxes of water and carbon dioxide from a riparian woodland ecosystem. *Agricultural and Forest Meteorology*. 122(1-2). 65-84.

Scott, R.L., Huxman, T.E., Williams, D.G., and Goodrich, D.C. 2006. Ecohydrological impacts of woody-plant encroachment: Seasonal patterns of water and carbon dioxide exchange within a semiarid riparian environment. *Global Change Biology*. 12(2): 311-324.

Scott, R.L., Huxman, T.E., Cable, W. L., and Emmerich, W. E. 2006. Partitioning of evapotranspiration and its relation to carbon dioxide exchange in a Chihuahuan Desert shrubland. *Hydrological Processes*. 20(15): 3227-3243.

Scott, R.L., Cable, W.L., Huxman, T.E., Nagler, P.L., Hernandez, M., and Goodrich, D.C. 2008. Multiyear riparian evapotranspiration and groundwater use for a semiarid watershed. *Journal of Arid Environments*. 72(7): 1232-1246.

Scott, R.L., Jenerette, G.D., Potts, D.L., and Huxman, T.E. 2009. Effects of seasonal drought on net carbon dioxide exchange from a woody-plant-encroached semiarid grassland. *Journal of Geophysical Research: Biogeosciences*. 114: G04004.

Scott, R.L., Hamerlynck, E.P., Jenerette, G.D., Moran, M.S., and Barron-Gafford, G.A. 2010. Carbon dioxide exchange in a semidesert grassland through drought-induced vegetation change. *Journal of Geophysical Research: Biogeosciences*. 115: G03026.

Scott, R.L., Huxman, T.E., Barron-Gafford, G.A., Darrel Jenerette, G., Young, J.M., and Hamerlynck, E. P. 2014. When vegetation change alters ecosystem water availability. *Global Change Biology*. 20(7): 2198-2210.

Scott, R.L., Biederman, J.A., Hamerlynck, E.P., and Barron-Gafford, G.A. 2015. The carbon balance pivot point of southwestern US semiarid ecosystems: Insights from the 21st century drought. *Journal of Geophysical Research: Biogeosciences*. 120(12): 2612-2624.

Seager, R., Ting, M., Held, I., Kushnir, Y., Lu, J., Vecchi, G., Huang, H.P., Harnik, N., Leetmaa, A., Lau, N.C., Li, C., Velez, J., and Naik, N. 2007. Model projections of an imminent transition to a more arid climate in southwestern North America. *Science*. 316(5828): 1181-1184.

Shao, J., Zhou, X., Luo, Y., Li, B., Aurela, M., Billesbach, D., Blanken, P. D., Bracho, R., Chen, J., Fischer, M., Fu, Y., Gu, L., Han, S., He, Y., Kolb, T., Li, Y., Nagy, Z., Niu, S., Oechel, W. C., Pinter, K., Shi, P., Suyker, A., Torn, M., Varlagin, A., Wang, H., Yan,

J., Yu, G., and Zhang, J. 2016. Direct and indirect effects of climatic variations on the interannual variability in net ecosystem exchange across terrestrial ecosystems. *Tellus B: Chemical and Physical Meteorology*. 68(1): 30575.

Smith, R.W., Chery, D.L., Renard, K.G., and Gwinn, W.R. 1981. Supercritical flow flumes for measuring sediment-laden flow. Technical Bulletin 1655. US Government Printing Office, Washington, D.C., USA, 72 pp.

Soegaard, H., and Møller-Jensen, L. 2003. Towards a spatial CO_2 budget of a metropolitan region based on textural image classification and flux measurements. *Remote Sensing of Environment*. 87(2-3): 283-294.

Song, T., and Wang, Y. 2012. Carbon dioxide fluxes from an urban area in Beijing. *Atmospheric Research*. 106: 139-149.

Song, J., Wang, Z.H., and Wang, C. 2017. Biospheric and anthropogenic contributors to atmospheric CO_2 variability in a residential neighborhood of Phoenix, Arizona. *Journal of Geophysical Research - Atmospheres*. 122(6): 3317-3329.

Sponseller, R.A., Hall, S.J., Huber, D.P., Grimm, N.B., Kaye, J.P., Clark, C.M., and Collins, S.L. 2012. Variation in monsoon precipitation drives spatial and temporal patterns of Larrea tridentata growth in the Sonoran Desert. *Functional Ecology*. 26(3): 750-758.

Stagakis, S., Chrysoulakis, N., Spyridakis, N., Feigenwinter, C. and Vogt, R. 2019. Eddy Covariance measurements and source partitioning of CO_2 emissions in an urban environment: Application for Heraklion, Greece. *Atmospheric Environment*. 201, 278-292.

Stewart, I.D., and Oke, T.R. 2012. Local climate zones for urban temperature studies. *Bulletin of the American Meteorological Society*. 93: 1879-1900.

Tarín, T., Nolan, R.H., Eamus, D., and Cleverly, J. 2020. Carbon and water fluxes in two adjacent Australian semi-arid ecosystems. *Agricultural and Forest Meteorology*. 281: 107853

Tarín, T., Yépez, E.A., Garatuza-Payán, J., Rodríguez, J.C., Méndez-Barroso, L.A., Watts, C.J., and Vivoni, E.R. 2020. Evapotranspiration flux partitioning at multi-species shrubland with stable isotopes of soil, plant, and atmospheric water pools. *Atmosfera*. 33(4): 319-335.

Templeton, R.C., Vivoni, E.R., Méndez-Barroso, L.A., Pierini, N.A., Anderson, C.A., Rango, A., Laliberte, A.S., and Scott, R.L. 2014. High-resolution characterization of a semiarid watershed: implications on evapotranspiration estimates. *Journal of Hydrology*. 509: 306-319.

Templeton, N.P., Vivoni, E.R., Wang, Z.H., and Schreiner-McGraw, A.P. 2018. Quantifying water and energy fluxes over different urban land covers in Phoenix, Arizona. *Journal of Geophysical Research - Atmospheres*. 123(4): 2111-2128.

Thatcher, D. 2021. Monthly precipitation data from a network of standard gauges at the Jornada Experimental Range (Jornada Basin LTER) in southern New México, January 1916 - ongoing ver 738. Environmental Data Initiative.

Thomey, M.L., Collins, S.L., Vargas, R., Johnson, J.E., Brown, R.F., Natvig, D.O., and Friggens, M.T. 2011. Effect of precipitation variability on net primary production and soil respiration in a Chihuahuan Desert grassland. *Global Change Biology*. 17(4): 1505-1515.

Turnbull, L., Parsons, A.J., and Wainwright, J. 2013. Runoff responses to long-term rainfall variability in a shrub-dominated shrubland. *Journal of Arid Environments*. 91: 88-94.

Twine, T. E., Kustas, W. P., Norman, J. M., Cook, D. R., Houser, P., Meyers, T. P., Prueger, J. H., Starks, P. J., and Wesely, M. L. 2000. Correcting eddy-covariance flux underestimates over a grassland. *Agricultural and Forest Meteorology*. 103(3): 279-300.

Ueyama, M., and Ando, T. 2016. Diurnal, weekly, seasonal, and spatial variabilities in carbon dioxide flux in different urban landscapes in Sakai, Japan. *Atmospheric Chemistry and Physics*. 16(22): 14727-14740.

Ukkola, A.M., De Kauwe, M.G., Roderick, M.L., Burrell, A., Lehmann, P., and Pitman, A.J., 2021 (Early Access). Annual precipitation explains variability in dryland vegetation greenness globally but not locally. *Global Change Biology*.

Unger, S., Maguas, C., Pereira, J.S., Aires, L.M., David, T.S., and Werner, C. 2009. Partitioning carbon fluxes in a Mediterranean oak forest to disentangle changes in ecosystem sink strength during drought. *Agricultural and Forest Meteorology*. 149(6-7): 949-961.

Unger, S., Máguas, C., Pereira, J.S., David, T.S., and Werner, C. 2012. Interpreting post-drought rewetting effects on soil and ecosystem carbon dynamics in a Mediterranean oak savannah. *Agricultural and Forest Meteorology*. 154: 9-18.

US Census Bureau. 2010. 2010 Census Data. http://2010.census.gov/2010censusdata/data/.

Van de Boer, A., Moene, A.F., Schuttemeyer, D., and Graf, A. 2013. Sensitivity and uncertainty of analytical footprint models according to a combined natural tracer and ensemble approach. *Agricultural and Forest Meteorology*. 169: 1-11.

Vargas, R., Yépez, E., Andrade, J., Angeles, G., Arredondo, T., Castellanos, A., Delgado, J., Garatuza-Payan, J., Gonzalez del Castillo, E., Oechel, W., Sanchez-Azofeifa, A., Velasco, E., Vivoni, E.R., and Watts, C. 2013. Progress and opportunities for monitoring greenhouse gas fluxes in Mexican ecosystems: The MexFlux Network. *Atmosfera*. 26(3): 325-336.

Velasco, E., Pressley, S., Allwine, E., Westberg, H., and Lamb, B. 2005. Measurements of CO_2 fluxes from the México City urban landscape. *Atmospheric Environment*. 39(38): 7433-7446.

Velasco, E., and Roth, M. 2010. Cities as net sources of CO2: Review of atmospheric CO_2 exchange in urban environments measured by eddy covariance technique. *Geography Compass*. 4(9): 1238-1259.

Velasco, E., Roth, M., Tan, S.H., Quak, M., Nabarro, S.D.A., and Norford, L. 2013. The role of vegetation in the CO_2 flux from a tropical urban neighbourhood. *Atmospheric Chemistry and Physics*. 13(20): 10185-10202.

Velasco, E., Perrusquia, R., Jiménez, E., Hernández, F., Camacho, P., Rodríguez, S., Retama, A., and Molina, L.T. 2014. Sources and sinks of carbon dioxide in a neighborhood of México City. *Atmospheric Environment*. 97: 226-238.

Velasco, E., Roth, M., Norford, L., and Molina, L.T. 2016. Does urban vegetation enhance carbon sequestration?. *Landscape and Urban Planning*. 148: 99-107.

Verduzco, V.S., Garatuza-Payán, J., Yépez, E.A., Watts, C.J., Rodríguez, J.C., Robles-Morua, A., and Vivoni, E.R. 2015. Variations of net ecosystem production due to seasonal precipitation differences in a tropical dry forest of northwest México. *Journal of Geophysical Research: Biogeosciences*. 120(10): 2081-2094.

Verduzco, V.S., Vivoni, E.R., Yépez, E.A., Rodríguez, J.C., Watts, C.J., Tarín, T., Garatuza-Payan, J., Robles-Morua, A., and Ivanov, V.Y. 2018. Climate change impacts on net ecosystem productivity in a subtropical shrubland of northwestern México. *Journal of Geophysical Research: Biogeosciences*. 123(2): 688-711.

Vermote, E., and Wolfe, R. MOD09GQ MODIS/Terra Surface Reflectance Daily L2G Global 250m SIN Grid V006 [Data set]. NASA EOSDIS LP DAAC. 2015. doi: 10.5067/MODIS/MOD09GQ.006

Vickers, D., and Mahrt, L. 1997. Quality control and flux sampling problems for tower and aircraft data. *Journal of Atmospheric and Oceanic Technology*. 14(3): 512-526.

Vitousek, P.M., Mooney, H.A., Lubchenco, J., and Melillo, J.M. 1997. Human domination of Earth's ecosystems. *Science*. 277(5325): 494-499.

Vivoni, E.R., Gutiérrez-Jurado, H.A., Aragón, C.A., Méndez-Barroso, L.A., Rinehart, A.J., Wyckoff, R.L., Rodríguez, J.C., Watts, C., Bolten, J.D., Lakshmi, V., and Jackson, T.J. 2007. Variation of hydrometeorological conditions along a topographic transect in northwestern México during the North American monsoon. *Journal of Climate*. 20(9): 1792-1809.

Vivoni, E.R., Moreno, H.A., Mascaro, G., Rodriguez, J.C., Watts, C.J., Garatuza-Payan, J., and Scott, R.L. 2008. Observed relation between evapotranspiration and soil moisture in the North American monsoon region. *Geophysical Research Letters*. 35: L22403.

Vivoni, E.R., Rodríguez, J.C., and Watts, C.J. 2010. On the spatiotemporal variability of soil moisture and evapotranspiration in a mountainous basin within the North American monsoon region. *Water Resources Research*. 46: W02509.

Vivoni, E.R., Pérez-Ruiz, E.R., Keller, Z.T., Escoto, E.A., Templeton, R.C., Templeton, N.P., Anderson, C.A., Schreiner-McGraw, A.P., Mendez-Barroso, L.A., Robles-Morua, A., Scott, R.L., Archer, S.R., and Peters, D.P.C. 2021. Long-term Research Catchments to Investigate Shrub Encroachment in the Sonoran and Chihuahuan Deserts: Santa Rita and Jornada Experimental Ranges. *Hydrological Processes*. 35: e14031.

Vivoni, ER and Perez-Ruiz, ER. 2020. AmeriFlux BASE US-Jo2 Jornada Experimental Range Mixed Shrubland, Ver. 1-5, AmeriFlux AMP, (Dataset). https://doi.org/10.17190/AMF/1617696

Vivoni, E.R., E.R. Perez-Ruiz, A.P. Schreiner-McGraw, R.C. Templeton, and C.A. Anderson. 2021a. Precipitation data from four locations within the Tromble Weir experimental watershed, located at the Jornada Basin LTER site, 2010-ongoing ver 22. Environmental Data Initiative. https://doi.org/10.6073/pasta/6724ba4a1d5714ad9f1d76fb933dd12d (Accessed 2021-10-04).

Vivoni, E.R., E.R. Perez-Ruiz, A.P. Schreiner-McGraw, R.C. Templeton, and C.A. Anderson. 2021b. Soil volumetric water content data from fifteen locations, 3 depths at each location, within the Tromble Weir experimental watershed at the Jornada Basin LTER site, 2010-ongoing ver 19. Environmental Data Initiative. https://doi.org/10.6073/pasta/c0cb4911122c455e333ffb2db490b578 (Accessed 2021-10-04).

Vogt, R., Christen, A., Rotach, M.W., Roth, M., and Satyanarayana, A.N.V. 2003. Fluxes and profiles of CO_2 in the urban roughness sublayer. In: Fifth International Conference on Urban Climate, Lodz, Poland. 4 pp.

Vogt, R., Christen, A., Rotach, M.W., Roth, M., and Satyanarayana, A.N.V. 2006. Temporal dynamics of CO_2 fluxes and profiles over a Central European city. *Theoretical and Applied Climatology*. 84(1-3): 117-126.

Volo, T.J., Vivoni, E.R., Martin, C.A., Earl, S., and Ruddell, B.L. 2014. Modelling soil moisture, water partitioning and plant water stress under irrigated conditions in desert urban areas. *Ecohydrology*. 7(5): 1297-1313.

Volo, T.J., Vivoni, E.R., and Ruddell, B.L. 2015. An ecohydrological approach to conserving urban water through optimized landscape irrigation schedules. *Landscape and Urban Planning*. 133: 127-132.

Wang, L., Caylor, K.K., Villegas, J.C., Barron-Gafford, G.A., Breshears, D.D., and Huxman, T.E. 2010. Partitioning evapotranspiration across gradients of woody plant cover: Assessment of a stable isotope technique. *Geophysical Research Letters*. 37(9): L09401.

Wang, S., Zhang, Y., Lü, S., Su, P., Shang, L., and Li, Z. 2016. Biophysical regulation of carbon fluxes over an alpine meadow ecosystem in the eastern Tibetan Plateau. *International Journal of Biometeorology*. 60(6): 801-812.

Ward, H.C., Kotthaus, S., Grimmond, C.S.B., Bjorkegren, A., Wilkinson, M., Morrison, W.T.J., Evans, J.G., Morrison, J.I.L., and Iamarino, M. 2015. Effects of urban density on carbon dioxide exchanges: Observations of dense urban, suburban and woodland areas of southern England. *Environmental Pollution*. 198: 186-200.

Webb, E.K., Pearman, G.I., and Leuning, R. 1980. Correction of flux measurements for density effects due to heat and water vapor transfer. *Quarterly Journal of the Royal Meteorological Society*. 106: 85-106.

Weissert, L.F., Salmond, J.A., Turnbull, J.C., and Schwendenmann, L. 2016. Temporal variability in the sources and fluxes of CO_2 in a residential area in an evergreen subtropical city. *Atmospheric Environment*. 143, 164-176.

Westenburg, C.L., Harper, D.P., and DeMeo, G.A. 2006. *Evapotranspiration by Phreatophytes Along the Lower Colorado River at Havasu National Wildlife Refuge, Arizona*. US Geological Survey Scientific Investigations Report 2006–5043, 44 pp., http://pubs.water.usgs.gov/sir20065043.

White, R.P., and Nackoney, J. *Drylands, people, and ecosystem goods and services: a web-based geospatial analysis* (PDF version). World Resources Institute, 2003. ([Available at: http://pdf. wri. org/drylands).

Wilcox, B.P., Dowhower, S.L., Teague, W.R., and Thurow, T.L. 2006. Long-term water balance in a semiarid shrubland. *Rangeland Ecology and Management*. 59(6): 600-606.

Wilczak, J.M., Oncley, S.P., and Stage, S.A. 2001. Sonic anemometer tilt correction algorithms. *Boundary Layer Meteorology*. 99: 127-150.

Williams, D.G., Scott, R.L., Huxman, T.E., Goodrich, D. C., and Lin, G. 2006. Sensitivity of riparian ecosystems in arid and semiarid environments to moisture pulses. *Hydrological Processes*. 20(15): 3191-3205.

Williams, C.A., Reichstein, M., Buchmann, N., Baldocchi, D., Beer, C., Schwalm, C., Wohlfahrt, G., Hasler, N., Bernhofer, C., Foken, T., Papale, D., Schymanski, S., and Schaefer, K. 2012. Climate and vegetation controls on the surface water balance: Synthesis of evapotranspiration measured across a global network of flux towers. *Water Resources Research*. 48: W06523.

Williams, I.N., and Torn, M.S. 2015. Vegetation controls on surface heat flux partitioning, and land-atmosphere coupling. *Geophysical Research Letters*. 42(21): 9416-9424

Wilson, K., Goldstein, A., Falge, E., Aubinet, M., Baldocchi, D., Berbigier, P., Berhhofer, C., Ceulemans, R., Dolman, H., Field, C., Grelle, A., Ibrom, A., Law, B.E., Kowalski, A., Meyers, T., Moncrieff, J., Monson, R., Oechel, W., Tenhunen, J.,

Valentini, R., and Verma, S. 2002. Energy balance closure at FLUXNET sites. *Agricultural and Forest Meteorology*, 113(1-4): 223-243.

Wilson, J.L., and Guan, H. 2004. Mountain-block hydrology and mountain-front recharge. In: Phillips, F., Hogan, J., and Scanlon, B. (Eds.), *Groundwater recharge in a desert environment, The southwestern United States*. Washington, DC, American Geophysical Union.

Wohlfahrt, G., Fenstermaker, L.F., and Arnone III, J.A. 2008. Large annual net ecosystem CO_2 uptake of a Mojave Desert ecosystem. *Global Change Biology*. 14(7): 1475-1487.

Wutzler, T., Lucas-Moffat, A., Migliavacca, M., Knauer, J., Sickel, K., Šigut, L., Menzer, O., and Reichstein, M. 2018. Basic and extensible post-processing of eddy covariance flux data with REddyProc. *Biogeosciences*. 15(16): 5015-5030.

Yahdjian, L., Gherardi, L.A., and Sala, O.E. 2011. Nitrogen limitation in arid-subhumid ecosystems: A meta-analysis of fertilization studies. *Journal of Arid Environments*. 75: 675-680.

Yahdjian, L., Sala, O.E., and Austin, A.T. 2006. Differential controls of water input on litter decomposition and nitrogen dynamics in the Patagonian Steppe. *Ecosystems*. 9: 128-141.

Yang, F., Zhou, G., Hunt, J. E., and Zhang, F. 2011. Biophysical regulation of net ecosystem carbon dioxide exchange over a temperate desert steppe in Inner Mongolia, China. *Agriculture, Ecosystems and Environment*. 142(3-4): 318-328.

Yépez, E.A., Scott, R.L., Cable, W., and Williams, D. 2007. Intraseasonal variation in water and carbon dioxide flux components in a semiarid riparian woodland. *Ecosystems*. 10: 1100-1115.

APPENDIX A

URBAN LANDSCAPES EDDY COVARIANCE AND ANCILLARY DATASETS

This appendix describes a digital repository of the eddy covariance and ancillary datasets for the four urban landscapes. The datasets are organized within the digital folder "Perez-Ruiz Dissertation/APPENDIX_A" https://drive.google.com/drive/folders/1orHDRpy9hhXbhHgdNRaLH4KpccLCiTOw?usp=sharing with four urban landscapes folders and an ancillary folder, as follows:

Folder Name	Description
Ancillary	Ancillary data used, as traffic counts data and vegetation indices.
Mesic_Landscape	Data from the mesic landscape site.
Parking_Lot	Data from the parking lot.
Reference_Suburban	Data from the suburban neighborhood.
Xeric_Landscape	Data from the mesic landscape.

The following folders are within each mobile tower folder:

Folder Name (\Urban_Landscape\)	Description
Data_Processed	Excel sheet(s) containing all meteorological and flux variables, post processing. Finalized table.
Photos	Photographs of each deployment.
Raw_Data	High frequency non-processed raw data

Additional datasets for the sites can be found in the digital repository in the next link:

https://doi.org/10.5281/zenodo.3625224

APPENDIX B

NORTHWESTERN MEXICAN ECOSYSTEMS EDDY COVARIANCE AND ANCILLARY DATASETS

This appendix describes a digital repository of the eddy covariance and ancillary datasets for three ecosystems of northwestern México. The datasets are organized within the digital folder "Perez-Ruiz Dissertation/APPENDIX_B" https://drive.google.com/drive/folders/1_OMGbYIBREOXj9StDL3nIcVdxeFD5Ctp?usp=sharing with three ecosystems folders and an ancillary data folder, as follows:

Folder Name	Description
Ancillary_Data	Data from the the rain gauge network, met stations and long-term precipitation and fluxes.
OS	Data from the Oak Savanna site.
RM	Data from the Riparian Mesquite Site.
SS	Data from the Subtropical Scrubland Site.

The following folders are within EC tower site:

Folder Name (\EC_Tower\)	Description
Gap_Filling	Files obtained from the gap filling and flux partitioning from the REddyProc online tool.
Photos	Photographs from each site.
Processed_Data	Processed data obtained from the EddyPro Software.
Raw_Data	High frequency non-processed raw data.

Additional datasets for the sites can be found in the digital repository in the next link:

https://doi.org/10.5281/zenodo.3522331

APPENDIX C

JER EDDY COVARIANCE AND ANCILLARY DATASETS

This appendix describes a digital repository of the eddy covariance and ancillary datasets for a mixed shrubland of the Chihuahuan Desert in the Jornada Experimental Range (JER). The datasets are organized within the digital folder "Perez-Ruiz Dissertation/APPENDIX_C" https://drive.google.com/drive/folders/1uRG3yawb2NVx8YzDOaTJF_mrXecMF-UP?usp=sharing as follows:

Folder Name	Description
Processed_Data	Full time series of processed data of hydrological, fluxes and meteorological data as well as ancillary measurements for the Jornada Experimental Range
Raw_Data	High frequency non-processed raw data for the Jornada Experimental Range

The following folders are within Processed_Data folder:

Folder Name	Description
Footprint	Footprints obtained using the method by Kljun et al., 2015
Full_Time_Series	This folder contains the full time series of hydrological, fluxes and meteorological datasets.
Gap_Filling	Files obtained from the gap filling and flux partitioning from the REddyProc online tool.
EddyPro	Files obtained after processing in the software EddyPro

More data can be found in the digital repository at:

https://ameriflux.lbl.gov/sites/siteinfo/US-Jo2

APPENDIX D

SRER EDDY COVARIANCE AND ANCILLARY DATASETS

This appendix describes a digital repository of the eddy covariance and ancillary datasets for a mesquite savanna of the Sonoran Desert in the Santa Rita Experimental Range (JER). The datasets are organized within the digital folder "Perez-Ruiz Dissertation/APPENDIX_D" https://drive.google.com/drive/folders/1cLUI3-0B2gqE8EdqLLmFQ4OnSwrGIiv9?usp=sharing as follows:

Folder Name	Description
Processed_Data	Full time series of processed data of hydrological, fluxes and meteorological data as well as ancillary measurements for the Santa Rita Experimental Range
Raw_Data	High frequency non-processed raw data for the Santa Rita Experimental Range

The following folders are within Processed_Data folder:

Folder Name	Description
Footprint	Footprints obtained using the method by Kljun et al., 2015
Full_Time_Series	This folder contains the full time series of hydrological, fluxes and meteorological datasets.
Gap_Filling	Files obtained from the gap filling and flux partitioning from the REddyProc online tool.
EddyPro	Files obtained after processing in the software EddyPro

More data can be found in the digital repository at:

https://ameriflux.lbl.gov/sites/siteinfo/US-SRS

APPENDIX E

FIELD DATALOGGER PROGRAMS

This appendix describes a digital repository of the datalogger programs used to obtain, process and retrieve fluxes, meteorological and ancillary measurements in all sites studied in this dissertation. The files are organized within the digital folder "Perez-Ruiz Dissertation/APPENDIX_E" https://drive.google.com/drive/folders/17v_tV9_kAQDRz6BPG3q2M-okMYjIkp9h?usp=sharing with three folders for each chapter, as follows:

Folder Name	Description
CH2	Contains the datalogger programs for the four urban landscapes studied in Chapter 2.
CH3	Contains the datalogger programs for the three ecosystems studied in Chapter 3.
CH4	Contains the datalogger programs JER and SRER study sites.

CH1 folder includes the next datalogger programs:

- Mobile Eddy Covariance Tower Datalogger Program

CH2 folder includes the next datalogger programs:

- Subtropical Scrubland Eddy Covariance Tower Datalogger Program
- Subtropical Scrubland Meteorological Data Datalogger Program
- Riparian Mesquite Eddy Covariance Tower Datalogger Program
- Oak Savanna Meteorological Data Datalogger Program

CH3 folder includes the next datalogger programs:

- Jornada Experimental Range Eddy Covariance Tower Datalogger Program
- Jornada Experimental Range Soil Moisture and Temperature Transects Sample
- Santa Rita Experimental Range Eddy Covariance Tower Datalogger Program
- Santa Rita Experimental Range Soil Moisture and Temperature Transects Sample

APPENDIX F

EDDY COVARIANCE DATA PROCESSING

This appendix describes a digital repository of the processing files used to obtain the half-hour eddy covariance processing data used in this dissertation. The files are organized within the digital folder "Perez-Ruiz Dissertation/APPENDIX_F" https://drive.google.com/drive/folders/1DLNlFTp7ksw9sRxLeq_pCuLgNgvqzyFY?usp=sharing with three folders for each chapter, as follows:

Folder Name	Description
CH2	Contains the processing files used to obtain the half-hour eddy covariance processing data used in Chapter 2.
CH3	Contains the processing files used to obtain the half-hour eddy covariance processing data used in Chapter 3.
CH4	Contains the processing files used to obtain the half-hour eddy covariance processing for the JER and SRER sites.

In Chapter 2, the software used to process the eddy covariance data was Edire, which is based on the use of a set of two scripts, (a) a script specifying the processing steps which is called Processing List and (b) a script specifying the data structure of the raw data files which is called Format List. As a result, folder \CH2 contains a file named XXXX_Proc_List describing the processing steps and a file called XXXX_Form_List for each urban landscape, where XXXX refers to the site name.

For Chapter 3 and 4, the software used to process the eddy covariance data was EddyPro, which is based in the use of two different files, (a) a file specifying processing settings to calculate the eddy covariance data, called EddyPro Project File (.eddypro), which includes information about datasets dates, file format, flux averaging, flux filtering, raw data processing steps, statistical tests, spectral analysis and corrections and

output files format; and (b) a metadata file including all the required information from the site, including location, called METADATA File (.metadata), which includes information about the elevation, canopy characteristics, file duration, data acquisition rate, instruments specifications and raw file description. As a result, folders \CH3 and \CH4 will include a set of two files for each site, a filed called XXX.eddypro containing the information of the data project and a file called XXXX.metadata containing the station info, instruments, and raw file description, where XXXX refers to the site name.

APPENDIX G

GIS DATA REPOSITORY

This appendix describes a GIS data repository for all the sites studied in the dissertation, as stored in a digital format. The GIS repository includes sensor locations, remote sensing imagery, land cover classifications, soil classifications, digital elevation models and boundaries. Files have a projected coordinate system in UTM using the datum WGS1984. After the file descriptions tables of each chapter, an image with sample GIS data is provided.

The GIS data is organized within the digital folder "Perez-Ruiz Dissertation/APPENDIX_G" https://drive.google.com/drive/folders/1fA-rY9W0m5mp5RnN2sTZfrJd5dQis83S?usp=sharing as follows:

Folder Name	Description
CH2	Contains the GIS data used in Chapter 2.
CH3	Contains the GIS data used in Chapter 3.
CH4	Contains the GIS data used in Chapter 4.

CH2 folder content:

File Name	Description
XL_Footprint.shp	Polygon of the 80% source area footprint of the xeric landscape site.
PL_Footprint.shp	Polygon of the 80% source area footprint of the parking lot site.
ML_Footprint.shp	Polygon of the 80% source area footprint of the mesic landscape site.
REF_Footprint.shp	Polygon of the 80% source area footprint of the suburban reference site.
XL_80_Source.tif	1-m resolution raster of the 80% source area contribution of the xeric landscape site.
PL_80_Source.tif	1-m resolution raster of the 80% source area contribution of the parking lot site.

ML_80_Source.tif	1-m resolution raster of the 80% source area contribution of the mesic landscape site.
REF_80_Source.tif	1-m resolution raster of the 80% source area contribution of the suburban reference site.
EC_Towers.shp	Locations of the eddy covariance towers.
Aerial_Image.tif	1-m aerial image of the Phoenix Metropolitan Area obtained from the National Agriculture Imagery Program (NAIP).

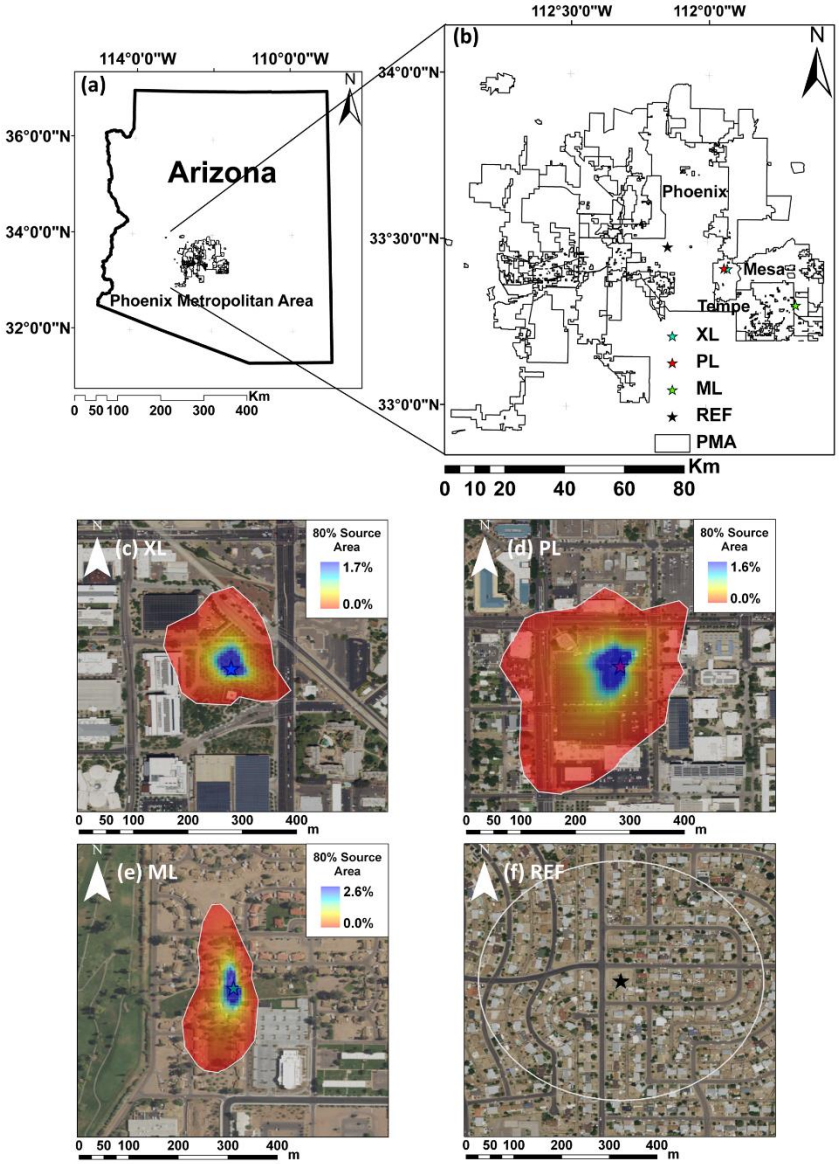

Figure G.1. Example of some GIS data used in Chapter 2.

CH3 folder content:

File Name	Description
EC_Towers.shp	Location of the eddy covariance towers.
Rain_Gauges.shp	Location of the rain gauges.
Temp_&_RH.shp	Location of air temperature and relative humidity probes.
dest2018gw.shp	Administrative divisions of Mexico showing the 32 states.
usv250s6gw.shp	1:250,000 Land Use and Vegetation map of Mexico.
eda251mgw.shp	1:250,000 Soil types map of Mexico.
h12b81 (folder)	Folder containing the topography elements of the topographic chart h12b81 of INEGI.
h12b82 (folder)	Folder containing the topography elements of the topographic chart h12b82 of INEGI.
h12b83 (folder)	Folder containing the topography elements of the topographic chart h12b83 of INEGI.
h12b12 (folder)	Folder containing the topography elements of the topographic chart h12b12 of INEGI.
h12b22 (folder)	Folder containing the topography elements of the topographic chart h12b22 of INEGI.
DEM.tif	15-m resolution digital elevation model of the study site.
Reflectances (folder)	Folder containing the raster files of MODIS 16-day composites of surface reflectance used to obtain NDVI for the year of 2017. The folder contains three folders: • b01: containing the surface reflectance for the red band. • b02: containing the surface reflectance for the near infrared band. • NDVI: containing the calculated NDVI.
Daily (folder)	Folder containing the long-term NDVI daily averages. This files where obtained by averaging the 2002-2017 images of each particular date.

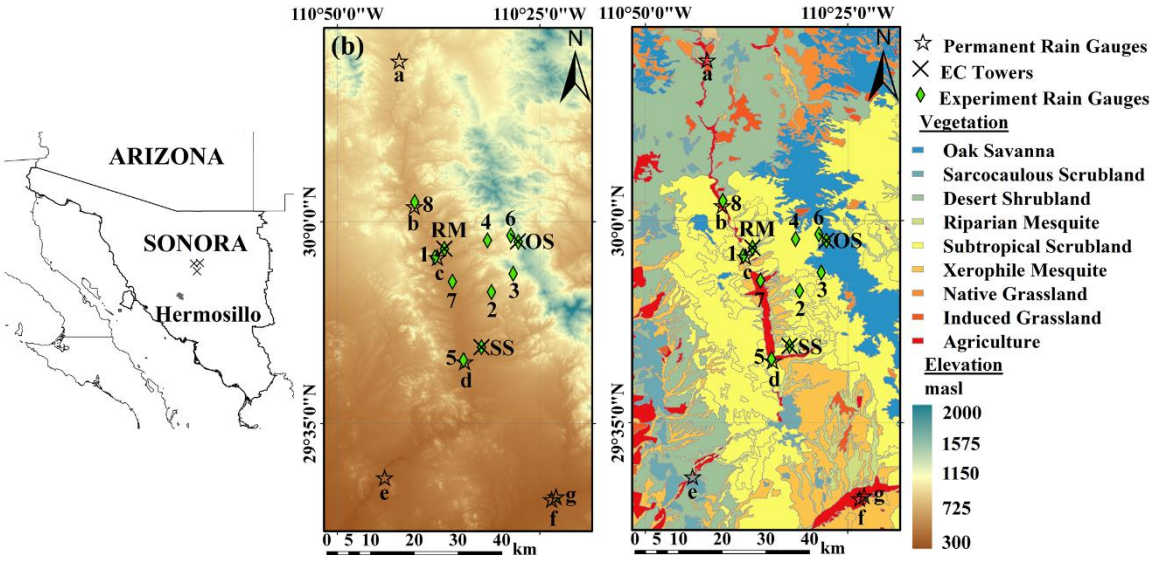

Figure G.2. Example of some GIS data used in Chapter 3.

CH4 folder content:

File Name	Description
JER_Boundary.shp	Boundary of the Jornada Experimental Range.
JER_Watershed.shp	Delimitation of the Tromble Weir watershed in the Jornada Experimental Range.
JER_EC.shp	Location of the eddy covariance tower in the Tromble Weir watershed in the Jornada Experimental Range.
JER_Raingauges.shp	Location of the four rain gauges in the Tromble Weir watershed in the Jornada Experimental Range.
JER_OuletFlume.shp	Location of the Santa Rita Supercritical Flume in the outlet of the Tromble Weir watershed in the Jornada Experimental Range.
JER_InternalFlumes.shp	Location of the three internal mini-flumes in the channels of the Tromble Weir watershed in the Jornada Experimental Range.
JER_COSMOS.shp	Location of the Cosmic-Ray Soil Moisture Sensor in the Tromble Weir watershed in the Jornada Experimental Range.
JER_SMTransects.shp	Location of the three soil moisture and temperature transects in the Tromble

	Weir watershed in the Jornada Experimental Range.
JER_T&RHProbes.shp	Location of the five air temperature and relative humidity probes in the Tromble Weir watershed in the Jornada Experimental Range.
JER_Cameras.shp	Location of the game cameras used to monitor vegetation phenology in the Tromble Weir watershed in the Jornada Experimental Range.
JER_Footprint.shp	2010-2020 80% source area footprint of the eddy covariance tower in the Tromble Weir watershed in the Jornada Experimental Range.
JER_DEM.tif	1-m digital elevation model of the Tromble Weir watershed in the Jornada Experimental Range.
JER_Vegetation.tif	6.5 cm high resolution vegetation classification of the Tromble Weir watershed in the Jornada Experimental Range.
JER_AerialImage.tif	6.5 cm high resolution aerial image of the Trombe Weir watershed in the Jornada Experimental Range.
JER_80SourceArea.tif	2010-2020 1-m 80% source area average contribution of the footprint of the eddy covariance tower on the Tromble Weir watershed in the Jornada Experimental Range.
SRER_Boundary.shp	Boundary of the Santa Rita Experimental Range.
SRER_Watersheds.shp	Delimitation of the watersheds 7 and 8 of the Santa Rita Experimental Range.
SRER_EC.shp	Location of the eddy covariance tower of the watersheds 7 and 8 in the Santa Rita Experimental Range.
SRER_Raingauges.shp	Location of the nine rain gauges of the watersheds 7 and 8 in the Santa Rita Experimental Range.
SRER_OuletFlumes.shp	Location of the two Santa Rita Supercritical Flumes in the outlet of the watersheds 7 and 8 in the Santa Rita Experimental Range.
SRER_COSMOS.shp	Location of the Cosmic-Ray Soil Moisture Sensor of the watersheds 7

	and 8 in the Santa Rita Experimental Range.
SRER_SMTransects.shp	Location of the eight soil moisture and temperature transects of the watersheds 7 and 8 in the Santa Rita Experimental Range.
SRER_T&RHProbes.shp	Location of the five air temperature and relative humidity probes of the watersheds 7 and 8 in the Santa Rita Experimental Range.
SRER_Cameras.shp	Location of the game camera used to monitor vegetation phenology of the watersheds 7 and 8 in the Santa Rita Experimental Range.
SRER_Footprint.shp	2011-2019 80% source area footprint of the eddy covariance tower of the watersheds 7 and 8 in the Santa Rita Experimental Range.
SRER_DEM.tif	1-m digital elevation model of the watersheds 7 and 8 in the Santa Rita Experimental Range.
SRER_Vegetation_2011.tif	1-m 2011 vegetation classification of the watersheds 7 and 8 in the Santa Rita Experimental Range.
SRER_Vegetation_2013.tif	1-m 2013 vegetation classification of the watersheds 7 and 8 in the Santa Rita Experimental Range.
SRER_Vegetation_2015.tif	1-m 2015 vegetation classification of the watersheds 7 and 8 in the Santa Rita Experimental Range.
SRER_Vegetation_2017.tif	1-m 2017 vegetation classification of the watersheds 7 and 8 in the Santa Rita Experimental Range.
SRER_Vegetation_2019.tif	1-m 2019 vegetation classification of the watersheds 7 and 8 in the Santa Rita Experimental Range.
SRER_AerialImage_2011.tif	1-m 2011 aerial image of the watersheds 7 and 8 in the Santa Rita Experimental Range.
SRER_AerialImage_2013.tif	1-m 2013 aerial image of the watersheds 7 and 8 in the Santa Rita Experimental Range.
SRER_AerialImage_2015.tif	1-m 2015 aerial image of the watersheds 7 and 8 in the Santa Rita Experimental Range.

SRER_AerialImage_2017.tif	1-m 2017 aerial image of the watersheds 7 and 8 in the Santa Rita Experimental Range.
SRER_AerialImage_2019.tif	1-m 2019 aerial image of the watersheds 7 and 8 in the Santa Rita Experimental Range.
SRER_80SourceArea.tif	2011-2019 1-m 80% source area average contribution of the footprint of the eddy covariance tower of the watersheds 7 and 8 in the Santa Rita Experimental Range.

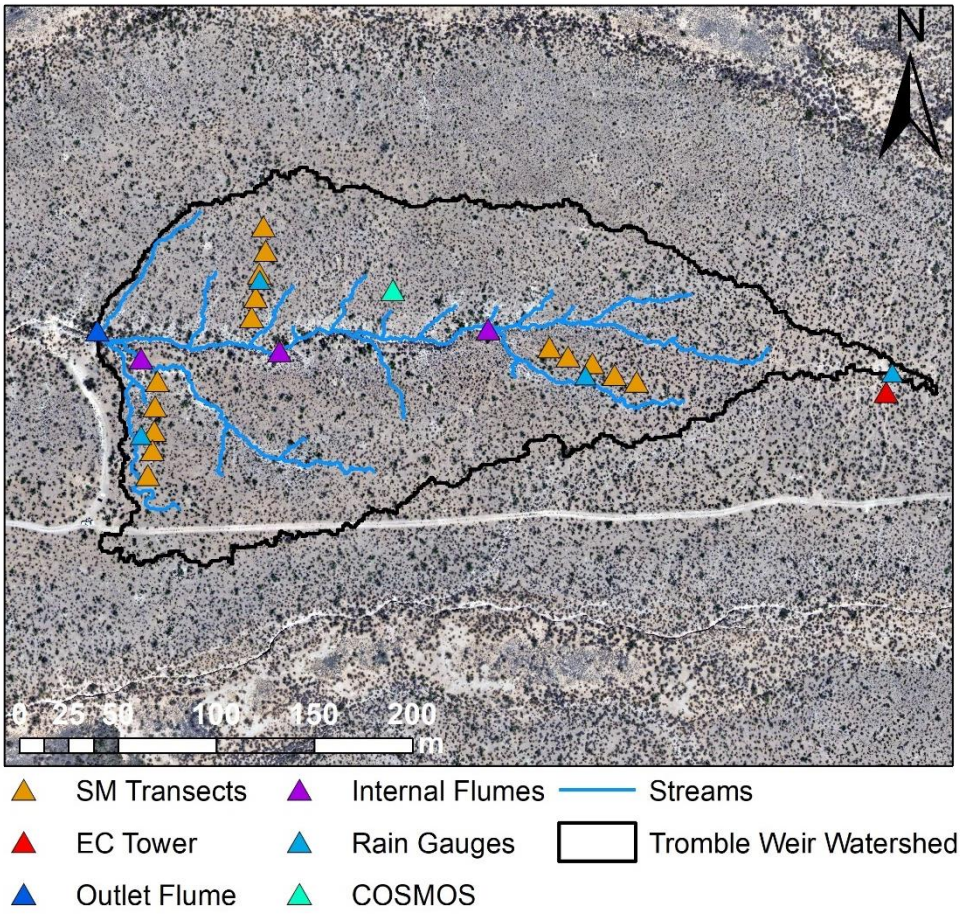

Figure G.3. Example of some GIS data from the Tomble Weir watershed study site in the Jornada Experimental Range.

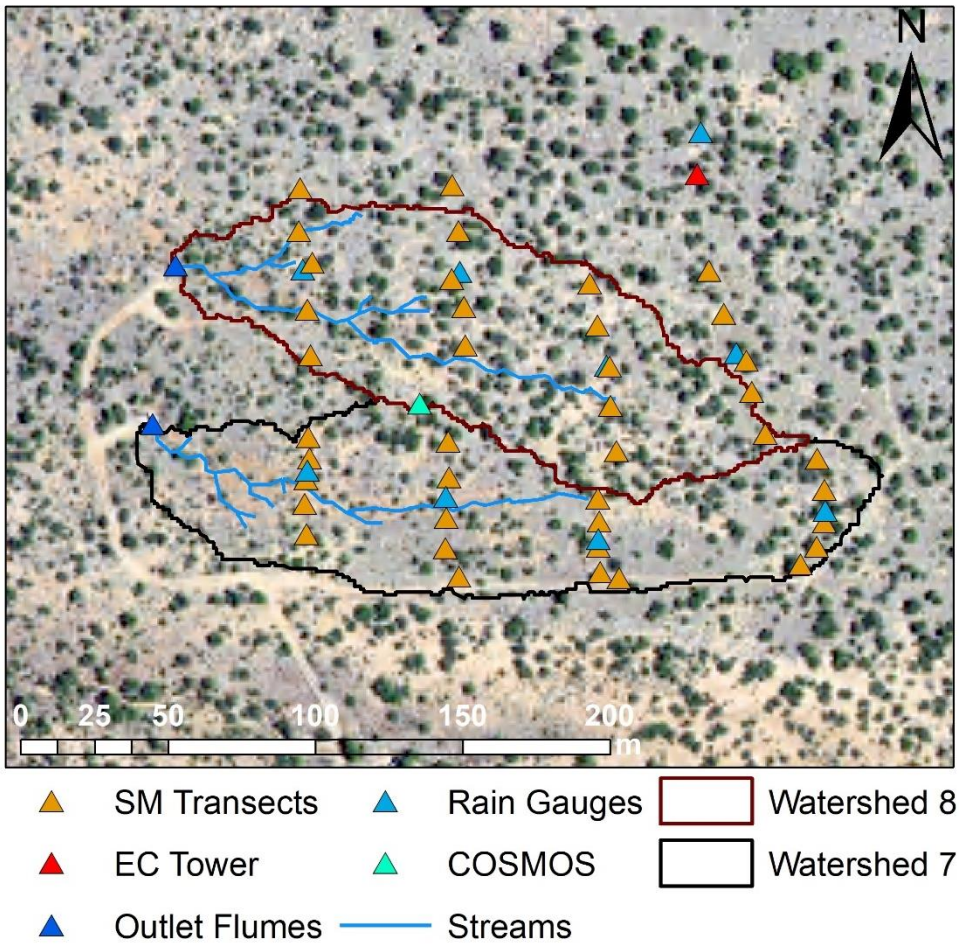

Figure G.4. Example of some GIS data from the watersheds 7 and 8 study site in the Santa Rita Experimental Range.

APPENDIX H

MATLAB SCRIPTS

This appendix describes a repository for Matlab scripts used to analyze the datasets. The scripts are organized within the digital folder "Perez-Ruiz Dissertation/APPENDIX_H" https://drive.google.com/drive/folders/1A4-mgOZe8V6BJPnUluCDow_dwkarCOTP?usp=sharing corresponding to the dissertation chapter in which they were used (Chapter 2, or 3 and 4).

Folder Name	Description
CH2	Contains the Matab scripts used in Chapter 2.
CH3	Contains the Matlab Scripts used in Chapter 3.
CH4	Contains the Matlab Scripts used in Chapter 4.

APPENDIX I

DISSERTATION FIGURES

This appendix describes a repository containing the dissertation figures, in PNG and TIFF format. It also included either Matlab scripts, ArcMap , SigmaPlot or PPT files used to generate each figure within this dissertation.

The dissertation figures, in PNG and TIFF format, with associated scripts or files, are organized within the digital folder “Perez-Ruiz Dissertation/APPENDIX_I” https://drive.google.com/drive/folders/1adasOLRH_IQ3Sx30BwVzDMY-ZK0-r982?usp=sharing as follows:

Folder Name	Description
CH2_Figures	All figures from Chapter 2 (2.1 to 2.10)
CH2_Scripts	Scripts or files to create figures from Chapter 2
CH3_Figures	All figures from Chapter 3 (3.1 to 3.8)
CH3_Scripts	Scripts or files to create figures from Chapter 3
CH4_Figures	All figures from Chapter 4 (4.1 to 4.6)
CH4_Scripts	Scripts of files to create figures from Chapter 4

APPENDIX J

DISSERTATION FINAL DATASETS

This appendix describes a repository containing the final datasets used in Chapters 2, 3 and 4. It includes the final datasets made publicly available through different digital repositories or the final processed data.

The dissertation datasets, in XLSX and CSV format, are organized within the digital folder "Perez-Ruiz Dissertation/APPENDIX_J" https://drive.google.com/drive/folders/19pLg0Xxy3TCxxoMtmSeFgCTY7s2hE_1m?usp=sharing as follow:

Folder Name	Description
CH2	Contains the datasets used in Chapter 2. These files are available through Zenodo in the next link: https://doi.org/10.5281/zenodo.3625224
CH3	Contains the datasets used in Chapter 3. These files are available through Zenodo in the next link: https://doi.org/10.5281/zenodo.3522331
CH4	Contains the datasets used in Chapter 4. These files are available through several digital repositories. The link to the repositories is specified for each file.

CH2 folder includes the next files:

File Name	Description
Sites_Information.xlsx	This file contains the metadata of the four urban landscapes studied in Chapter 2. Data includes name, land cover type, LCZ, location, sampling periods, instruments information, etc.
Meteorology.xlsx	This file contains the half-hour values of the ancillary meteorological data used in Chapter 2. The file contains five spreadsheets: • Read me: contains information regarding variables names, units and description.

	• XL: half-hour meteorological data for the xeric landscape site • PL: half-hour meteorological data for the parking lot site • ML: half-hour meteorological data for the mesic landscape site • REF: half-hour meteorological data for the suburban reference site
Fluxes.xlsx	This file contains the half-hour values of water, energy, and carbon fluxes as well as additional turbulent measurements used in Chapter 2. The file contains five spreadsheets: • Read me: contains information regarding variables names, units and description. • XL: half-hour meteorological data for the xeric landscape site • PL: half-hour meteorological data for the parking lot site • ML: half-hour meteorological data for the mesic landscape site • REF: half-hour meteorological data for the suburban reference site

CH3 folder includes the next files:

File Name	Description
GPS-Hydrometeorological Fluxes.xlsx	This file contains half-hour values of water, energy, and carbon fluxes as well as ancillary meteorological data used in Chapter 3. In the case of water, energy and carbon fluxes, it includes the original fluxes, filtered fluxes and gap-filled fluxes. The file contains four spreadsheets: • Read me: contains information regarding variables names, units and description, as well as relevant information about the study sites, including site name, location, sampling periods,

	vegetation type and instrument characteristics. • Rayon: it includes the half-hour values of water, energy, and carbon fluxes and ancillary meteorological data of the Subtropical Scrubland site. • Opodepe: it includes the half-hour values of water, energy, and carbon fluxes and ancillary meteorological data of the Riparian Mesquite site. • Sierra Los Locos: it includes the half-hour values of water, energy, and carbon fluxes and ancillary meteorological data of the Oak Savanna site.
GPS-Hydrometeorological Precipitation.xlsx	This file contains the daily values of rainfall from the 11 rain gauges installed during the field campaign of Chapter 3. The file contains two spreadsheets: • Read me: contains information regarding relevant information about the rain gauges, including site name, location, sampling periods and rain gauge characteristics. • Daily R: contains daily values of rainfall for the 11 rain gauges installed during the field campaign described in Chapter 3.

CH4 folder includes the next files:

File Name	Description
US-Jo2_HH_201008020000_202101010000_v3.0.csv	This file contains the half-hour values of water, energy and carbon fluxes, ancillary meteorological data and additional information on turbulent fluxes from August 2nd, 2010 to December 31st, 2020. The file corresponds to the data available in the

	Ameriflux network for the site US-Jo2 Jornada Experimental Range Mixed Shrubland https://ameriflux.lbl.gov/sites/siteinfo/US-Jo2 . Data can be obtained through the Ameriflux Data Portal. Information about the description of the variables can be found in the next link: https://ameriflux.lbl.gov/data/aboutdata/data-variables/
JRN_338002_Tromble_precip_data.csv	This file contains the 1-min resolution rainfall from the four rain gauges installed in the Tromble Weir watershed. The rain gauges correspond to the three rain gauges (R2, R3 and R4) accompanying the three soil moisture transects in the site as well as the rain gauge (R_tower) accompanying the eddy covariance tower. Data spans from July 1st, 2010 to December 31st, 2020. This data can be obtained from the EDI Data Portal in the next link: https://portal.edirepository.org/nis/mapbrowse?scope=knb-lter-jrn&identifier=210338002 Metadata from this file can be seen in the next link: https://portal.edirepository.org/nis/metadataviewer?packageid=knb-lter-jrn.210338002.22
JRN_338004_Tromble_transect_VWC_data.csv	This file contains half-hour values of soil volumetric water content at 5cm, 15cm and 30 cm from three soil moisture transects (T1, T2 and T3) in the Tromble Weir watershed. Data spans from June 6th, 2010 to December 31st, 2020. This data can be obtained from the EDI Data Portal in the next link: https://portal.edirepository.org/nis/mapbrowse?scope=knb-lter-jrn&identifier=210338004 Metadata from this file can be seen in the next link:

	https://portal.edirepository.org/nis/metadataviewer?packageid=knb-lter-jrn.210338004.19
JRN_338006_Tromble_tower_meteorology_data.csv	This file contains half-hour values of ancillary meteorological variables obtained from the eddy covariance tower at the Tromble Weir watershed. Data spans from May 28th, 2010 to December 31st, 2020. Data include soil volumetric water content at four depths (5cm, 15 cm, 30 cm and 50 cm), air temperature, relative and absolute humidity, vapor pressure (saturated and deficit), atmospheric pressure, radiation (incoming and outgoing shortwave, solar and net), soil heat flux and soil temperature. This data can be obtained from the EDI Data Portal in the next link: https://portal.edirepository.org/nis/mapbrowse?scope=knb-lter-jrn&identifier=210338006 Metadata from this file can be seen in the next link: https://portal.edirepository.org/nis/metadataviewer?packageid=knb-lter-jrn.210338006.2
JER_Met_2010-2020.xlsx	This file contains the half-hour values of the meteorological data obtained from the eddy covariance tower. Data corresponds to the entire data from 2010-2020 obtained from the table "Met" from the CR5000 datalogger that controls and store the data from the eddy covariance tower. Data has not been processed, filtered or gap filled. The file contains two spreadsheets: • Read me: contains information about the description of the variables. • Met: contains the half-hour values of meteorological data.
JER_Fluxes_2010-2020.xlsx	This file contains the half-hour values of the water, energy and carbon fluxes

	obtained from the eddy covariance tower. Data corresponds to the entire data from 2010-2020 obtained from the table "Fluxes" from the CR5000 datalogger that controls and store the data from the eddy covariance tower. Data has not been processed, filtered or gap filled. The file contains two spreadsheets: • Read me: contains information about the description of the variables. • Fluxes: contains the half-hour values of fluxes.
JER_PTOutlet_2010-2020.xlsx	This file contains the 1-min resolution runoff data. Data corresponds to the entire data from 2010-2020 obtained from the Santa Rita supercritical flume located in the outlet of the Tromble Weir watershed. Data includes the pressure from the pressure transducer, height of water flow, unfiltered runoff in $m^3 s^{-1}$ and mm, and filtered runoff in mm. The file contains two spreadsheets: • Read me: contains information about the description of the variables and the description of the calculation of water height and runoff as well as the runoff filtering and units conversion. • PT: contains the 1-min resolution pressure, water height and runoff.
JER_Runoff_2010-2020.xlsx	This file contains half-hour values of runoff in $m^3 s^{-1}$ and mm from the Santa Rita supercritical flume located in the outlet of the Tromble Weir watershed. Data was aggregated from the data of 1-min values of the JER_PTOutlet_2010-2020.xlsx file described before. It spans

	the entire available data from 2010-2020. The file contains two spreadsheets: • Read me: contains information about the description of the variables. • Q: contains the half-hour values of runoff in $m^3 s^{-1}$ and mm.
JER_Rainfall_2010-2020.xlsx	This file contains half-hour and daily values of rainfall from the four rain gauges in the Tromble Weir watershed. It includes the rainfall values from the individual rain gauges as well as the watershed average obtained using Thiessen polygons. Data has been filtered and corrected. It spans the entire available data from 2010-2020. The file contains three spreadsheets: • Read me: contains information about the description of the variables and the procedures to filter, correct and aggregate the rainfall values. • Half-Hour: contains the half-hour values of rainfall from the four individual rain gauges as well as the watershed average. • Daily: contains the daily values of rainfall from the four individual rain gauges as well as the watershed average.
JER_TransectSM_2010-2020.xlsx	This file contains half-hour values of soil volumetric water content and soil temperature at 5 cm, 15 cm and 30 cm from the three soil moisture transects in the Tromble Weir watershed. It also includes the average soil moisture for the watershed for 5 cm, 15 cm and 30 cm, as well as the watershed average for the rooting zone (40 cm). It spans the

	entire available data from 2010-2020. The file contains three spreadsheets: • Read me: contains information about the description of the variables and the procedures to obtain the average values. • Jun2010-Sep2016: contains the half-hour values organized and processed by Adam Schreiner-McGraw. • Oct2016-Dec2020: contains the half-hour values organized and processed by Eli Perez-Ruiz.
JER_FluxesEddyPro_2010-2020.xlsx	This file contains the half-hour values of the water, energy and carbon fluxes obtained after processing the high frequency flux data using the software Eddy Pro. Data corresponds to the entire data from 2010-2020 obtained from the file labeled "full_output" created by EddyPro. Data has not been filtered or gap filled. The file contains two spreadsheets: • Read me: contains information about the description of the variables. • Fluxes: contains the half-hour values of fluxes processed by EddyPro.
JER_FluxesGapFilled_2010-2020.xlsx	This file contains the half-hour values of the water, energy and carbon fluxes obtained after performing the gap filling and flux partitioning using the tool REddyProc (https://www.bgc-jena.mpg.de/bgi/index.php/Services/REddyProcWeb). Data corresponds to the entire data from 2010-2020 obtained from the output file generated by REddyProc. Data was filtered prior to the gap filling and flux partitioning. The file includes the filtered original data,

	gap filled data, flux partitioned data and ancillary variabes. The file contains two spreadsheets: • Read me: contains information about the description of the variables, the filtering process and information about the REddyProc tool. • GF: contains the half-hour values of original filtered data, gap filled data and flux partitioning.

APPENDIX K

SUPPLEMENTARY EFFORTS

This appendix describes a repository containing the description and data obtained from additional efforts performed during the duration of my Ph. D. These supplementary efforts include:

- Installation of microclimatic sensors (Air temperature and relative humidity probes).
- Installation of game cameras for the monitoring of phenology and hydroclimatic events.
- Flux footprint analysis.
- Infiltration tests using a single-ring infiltrometer.

All data obtained from the supplementary efforts can be found in the folder "Perez-Ruiz Dissertation/APPENDIX_K" https://drive.google.com/drive/folders/1ozQaEqetoUxjmTJn0UidTqc6CFJdsjAF?usp=sharing

K.1. Installation of microclimatic sensors (Air temperature and relative humidity probes).

As part of the efforts to continue with the instrumentations of the Tromble Weir watershed, a set of five air temperature and relative humidity probes were installed in the watershed to monitor the microclimatic conditions induced by elevation and aspect. The sensor installed were HOBO Pro v2 Temperature/Relative Humidity data loggers (Figure K1.1), which have a built-in temperature and relative humidity sensors. Sensors were protected with a solar radiation shield (Figure K1.2) and installed in different locations.

Figure K.1.1. HOBO Pro v2 Temperature/Relative Humidity data loggers with built-in temperature and relative humidity sensors.

Figure K.1.2. Air temperature and relative humidity sensors installed in the field site, including the solar radiation shield.

Sensors were located to capture the variation of microclimatic conditions with elevation and aspect. With that in mind, the sensors were placed in the next locations:

- North facing hillslope.
- South facing hillslope.
- Low elevation channel.
- High elevation channel.
- High elevation flat surface (in the eddy covariance tower.

Figure K1.3 shows the location of the five sensors in relation to elevation and stream network within the watershed. Even when the sensors are still installed in the watershed, I stopped the data retrieval on July 17th, 2018. Available data can be found in the folder "Air Temperature and Relative Humidity" in the digital repository of this appendix.

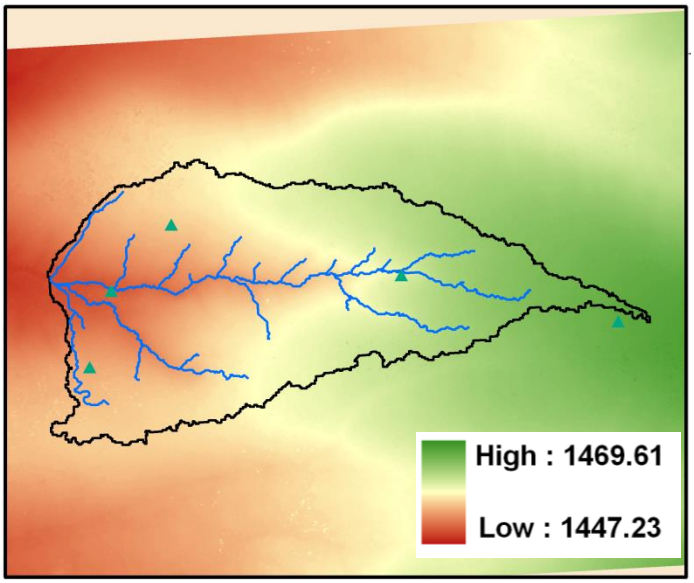

Figure K.1.3. Location of the air temperature and relative humidity probes (green triangles) within the Tromble Weir watershed. The gradient represents elevation in meters.

K.2. Installation of game cameras for the monitoring of phenology and hydroclimatic events.

A set of five game cameras (Figure K.2.1) were installed in the Tromble Weir watershed. The cameras were Moultrie M-550 Game Cameras. Installation started on October 29th, 2016, with the setup of two cameras, one located facing upstream of the Santa Rita supercritical flume in the outlet of the watershed and another in the eddy covariance tower. The initial objectives of the cameras were: (1) take advantage of the motion detection and infrared features of the game cameras to try to capture runoff event reaching the watershed outlet, and (2) to monitor the phenology of the entire watershed

with the camera in the eddy covariance tower using the option of schedule photographs. Three more game cameras were installed in subsequent months. The additional cameras were installed facing upstream of the internal mini flumes with the objective of capture runoff events in the internal flumes.

Figure K.2.1. Moultrie M-550 game camera used to monitor the Tromble Weir watershed.

Cameras were setup to detect movement through the motion-detection sensors and to capture photographs every 30 minutes from 10:00 to 14:00. Photographs were stored in an internal memory card and included a strip with information of the photograph taken, including temperature, camera ID, date and time. Here I present a sample photograph of each camera and their respective name.

Figure K.2.2. Photograph of the view of the Tromble Weir watershed from the eddy covariance tower camera.

Figure K.2.2. Photograph of the view upstream of the outlet flume of the Tromble Weir watershed.

Figure K.2.3. Photograph of the view upstream of the mini flume of channel 1.

Figure K.2.4. Photograph of the view upstream of the mini flume of channel 2.

Figure K.2.5. Photograph of the view upstream of the mini flume of channel 3.

Photographs were retrieved at every field trip and troubleshooting included the replacement of batteries, the correct replacement of the camera and empty the memory card. I stopped the photographs retrieval on February 16th, 2019. Unfortunately, the game cameras were not able to detect runoff events through the motion-detection sensors, however, the complete set of photographs from the five cameras offered an extraordinary option to monitor phenology of the plants of the watershed as well as to capture the variability of the hydroclimatology of the site.

Photographs taken during the entire sampling period can be found in the folder "Phenocam" in the digital repository of this appendix. Within the folder, the next folders can be found:

Folder Name	Description
Channel 1	Contains the photographs of the game camera facing upstream of channel 1.
Channel 2	Contains the photographs of the game camera facing upstream of channel 2.
Channel 3	Contains the photographs of the game camera facing upstream of channel 1.
Outlet	Contains the photographs of the game camera facing upstream of the watershed outlet.
Tower	Contains the photographs of the game camera in the eddy covariance tower.

K.3. Flux footprint analysis.

Flux footprints are commonly used to have a better interpretation of the flux tower measurements, as they provide the size, position, and direction of the source areas from where the fluxes are being measured. Obtaining the flux footprint is crucial to have a right understanding of the landscape elements that are influencing the behavior of the flux. As part of the analysis performed during this dissertation, the flux footprints were obtained for all the eddy covariance towers used in chapters 2, 3 and 4.

For Chapter 2, footprints for the eddy covariance towers were obtained using the method by Komann and Meixner (2001) using the software EdiRe. This is a crosswind integrated model based on the solution of the two-dimensional advection-diffusion equation given for power-law profiles in wind velocity and eddy diffusivity. Contributing distances are calculated according to:

$$f_x = \frac{1}{\Gamma(\mu)} \frac{\xi^{\mu}}{x^{1+\mu}} e^{-\xi/x} \quad \text{(K.3.1)}$$

where *x* is the distance from the location of the anemometer measured in the wind direction, $\xi = \xi(z)$ is a flux length scale that depends on the height above the ground *z*, μ is a dimensionless model constant and $\Gamma(\mu)$ is the gamma function. The equation is used to calculate *x*, given the fraction of the flux contribution of interest (10%, 30%, etc.). The equation for the peak distance is explicitly derived by the authors by finding the maximum from the former equation:

$$x_{peak} = \frac{\xi}{1+\mu} \quad \text{(K.3.2)}$$

For Chapters 3 and 4, footprints were obtained using the Kljun et al. (2004). The footprint is calculated according to the next formulas:

Peak contribution distance in meters:

$$x_{peak} = X^*_{peak} z_m \left(\frac{\sigma_w}{u_*}\right)^{-0.8}, X^* = c - d \quad \text{(K.3.3)}$$

NN% contribution in meters:

$$x_{NN\%} = X^*_{NN\%} z_m \left(\frac{\sigma_w}{u_*}\right)^{-0.8}, X^*_{NN\%} = L'_{NN\%} \cdot c - d \quad \text{(K.3.4)}$$

where *NN%* is the represents the % of distance ranging from 10% to 90%, z_m is the height of turbulent measurements, σ_w is the standard deviation of vertical velocity fluctuations, u_* is the friction velocity, $L'_{NN\%}$ is the distance corresponding to *NN%*, and *c* and *d* are parameters obtained using the equations 13 to 16 in Kljun et al. (2004). The footprint parameterization is valid only in certain ranges of micrometeorological

conditions. In particular, the model is claimed to be valid if the following conditions hold:

- The measurement height is lower than the boundary layer height.
- The terrain is dynamically homogeneous.
- The stability parameter is in the range of: $-200 < \zeta < 1$.
- The friction velocity is larger than a specific threshold: $u_* \geq 0.2$ m s^{-1}.
- The measurement height is larger than 1 m: $z_m \geq 1$m.

Footprints were calculated using a Matlab script downloaded from the Kljun Flux Footprint Prediction site in the next link: https://footprint.kljun.net/

Footprints for Chapters 2, 3 and 4 can be found in APPENDIX A, B, C, D and G and the scripts used to calculate the footprints can be found in APPENDIX A and H.

K.4. Infiltration rate estimations using a single-ring infiltrometer.

During the summer of 2018, as part of the research activities of an undergraduate student having a Research Experience for Undergraduate (REU), measurements of saturated hydraulic conductivity (Ksat). Measurements were done using a single-rin infiltrometer as described in the Chapter 8 of the book Monitoring Manual for Grassland, Shrubland and Savanna Ecosystems, Volume II: Design, supplementary methods and interpretation. A total of 56 sampling locations were selected to perform infiltration rates test across the study site trying to encompass all the variability of soil conditions, including bare soil and soil under the canopy of individual shrublands, grasses, mixture of shrublands and shrub-grass mixes. Figure K.4.1 shows the sampling locations.

The single-ring infiltrometer consisted in a metal infiltrometer ring of 12.5 cm of diameter and an infiltration water bottle of 8.7 cm diameter with an attached ruler to measure the level of water (Figure K.4.2). Ancillary materials, such towels, plastic bags, cups, gallons of water, etc., were used to support the measurements. The methodology consisted in the next set of steps:

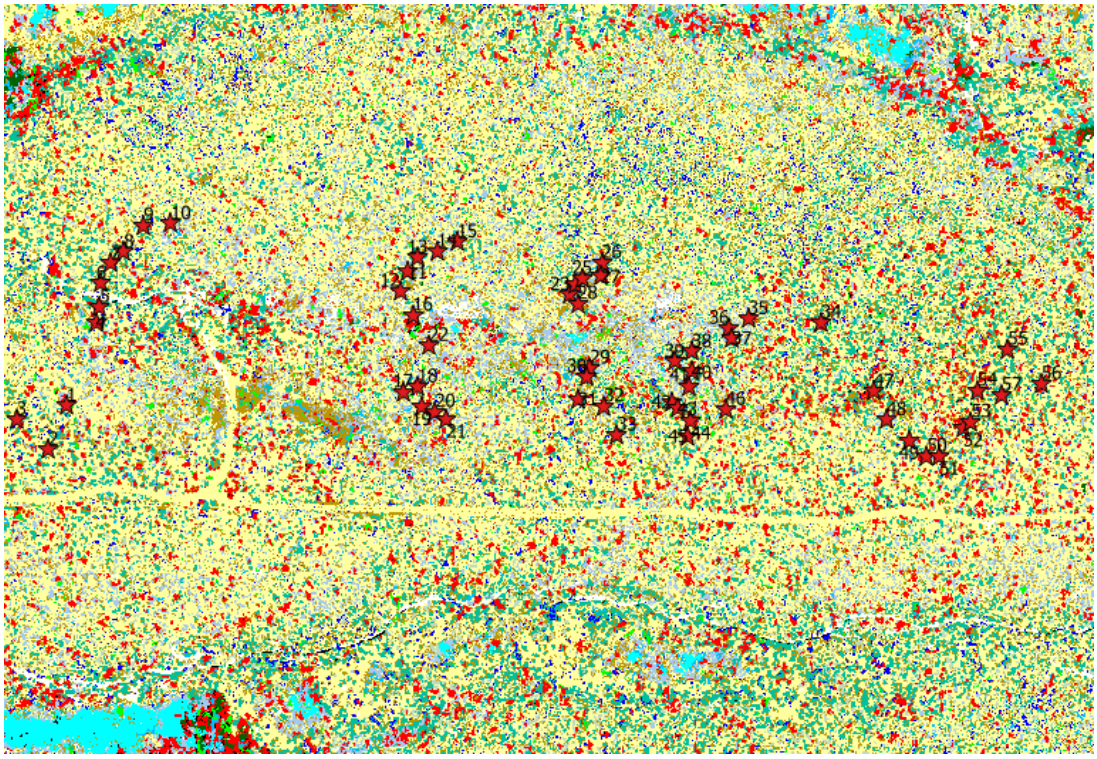

Figure K.4.1. Sampling locations for infiltration rate estimations.

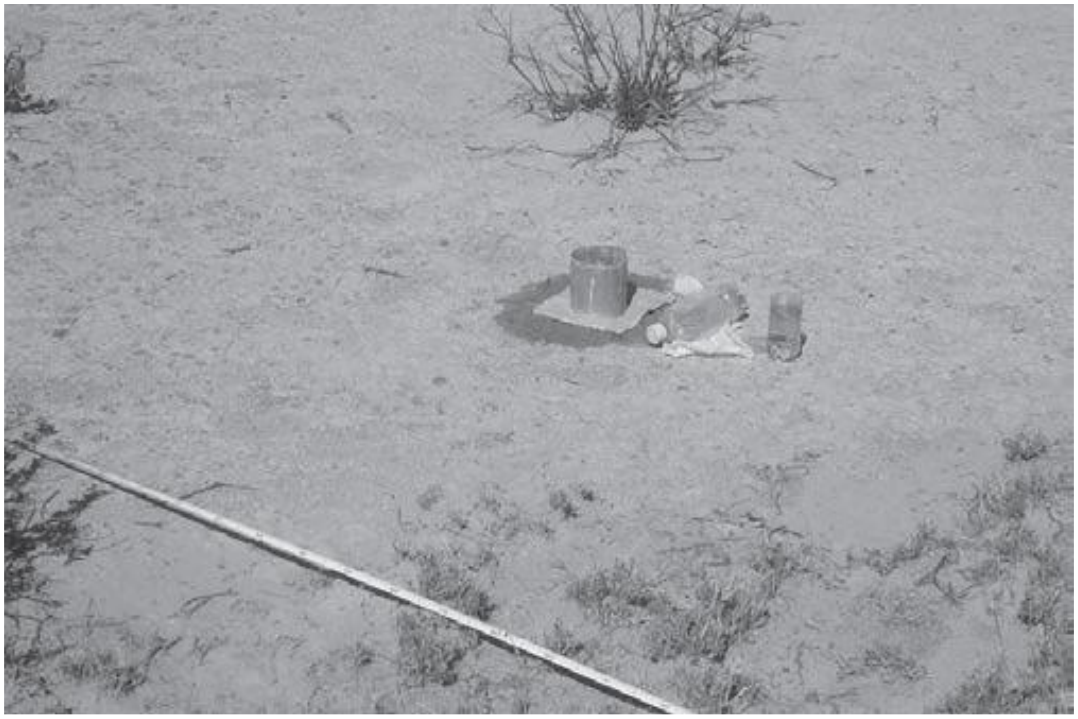

Figure K.4.2. Single-ring infiltrometer.

1. Determine the location of the test and get coordinates.
2. Record the vegetation class of the sampling point.
3. Pre-wet the soil to a depth of at least 4 cm (Figure K.4.3).

Figure K.4.3. Pre-wetting of the soil.

4. Insert the infiltrometer ring to a depth of 3 cm (Figure K.4.4).

Figure K.4.4. Inserting infiltration ring to 3 cm.

5. Add water to the ring without disturbing the soil surface (Figure K.4.5).

Figure K.4.5. Adding water to the ring using a plastic bag.

6. Watch for leaks (Figure K.4.6).

Figure K.4.6. Water leaking from the infiltrometer ring.

7. Place infiltrometer water bottle in the ring (Figure K.4.7).

Figure K.4.7. Suspending the infiltrometer water bottle in the infiltrometer ring.

8. Adjust the pipette to maintain the water in the ring at 3 cm (Figure K.4.8).

Figure K.4.8. Adjusting the pipette

9. Record the water level in the bottle with the help of the ruler.
10. Wait for the water level in the bottle to drop at least 50 mm.
11. Record the infiltration end time and measure the distance the water level has dropped

To calculate the actual infiltration rate, the actual diameter of the infiltrometer ring and water bottle needs to be known. The steps followed to calculate the infiltration rate in mm/hr are shown next:

1. Calculate the cross-sectional area of the infiltrometer water bottle.
2. Calculate the cross-sectional area of the infiltrometer ring.
3. Calculate the correction factor for the difference between the area of the bottle and the area of the ring. Correction factor = bottle area/ring area.
4. Calculate the infiltration time in hours.
5. Calculate the infiltration rate in mm/hr. Infiltration rate = distance the water dropped (in mm) divided by the amount of time it took to drop (in hours).
6. Calculate the soil infiltration rate (corrected for the difference in area between the ring and the bottle). This is done by multiplying the infiltration rate from step 5 by the correction factor from step 3.

Values of saturated hydraulic conductivity for the 56 sampling points were stored in an excel file. The excel file as well as the vector file containing the locations of the sampling points can be found in the folder “Infiltration Rates” in the digital repository of this appendix.

APPENDIX L

STUDY SITES PHOTOGRAPHS

This appendix a series of photographs of the study sites, including instrumentation, landscapes characteristics, sampling activities hydrometeorological events, etc. Each photograph includes a brief description. Photographs can be found in the digital folder “Perez-Ruiz Dissertation/APPENDIX_L” https://drive.google.com/drive/folders/1GNttJD8zmwhC1OEYmFHdNQxoMvw1bxZH?usp=sharing . Credit of the photographs belong to Eli R. Perez-Ruiz unless it is specified in the description.

L.1 Urban Landscapes of Chapter 2.

Figure L.1.1. Eddy covariance tower installed in the Xeric Landscape. Credit: Nicole Templeton.

Figure L.1.2. Eddy covariance tower installed in the Parking Lot. Credit: Nicole Templeton.

Figure L.1.3. Eddy covariance tower installed in the Mesic Landscape. Credit: Nicole Templeton.

Figure L.1.4. Eddy covariance tower of the Suburban Reference site. Credit: Nicole Templeton.

Figure L.1.5. Photograph of the mobile tower used to setup the eddy covariance system. Credit: Nicole Templeton.

L.2. Ecosystems of northwestern Mexico studied in Chapter 3.

Figure L.2.1. Eddy covariance tower in the Subtropical Scrubland site.

Figure L.2.2. Photograph of the Subtropical Scrubland site before the monsoon.

Figure L.2.3. Photograph of the Subtropical Scrubland site during the monsoon.

Figure L.2.4. Eddy covariance tower in the Riparian Mesquite site.

Figure L.2.5. Photograph of the Riparian Mesquite site before the monsoon.

Figure L.2.6. Photograph of the Subtropical Scrubland site during the monsoon.

Figure L.2.7. Eddy covariance tower in the Oak Savanna site.

Figure L.2.8. Photograph of the Oak Savanna site before the monsoon.

Figure L.2.9. Photograph of the Oak Savanna site during the monsoon.

Figure L.2.10. Photograph of the location of a rain gauge before the monsoon.

Figure L.2.11. Photograph of the location of a rain gauge during the monsoon.

Figure L.2.12. Rainfall event in a mountain range near Rayon, Sonora, Mexico during the monsoon.

L.3. Tromble Weir watershed and instrumentation in the Jornada Experimental Range

Figure L.3.13. Landscape view of the mixed shrubland in the Tromble Weir watershed.

Figure L.3.14. Landscape view of the mixed shrubland in the Tromble Weir watershed.

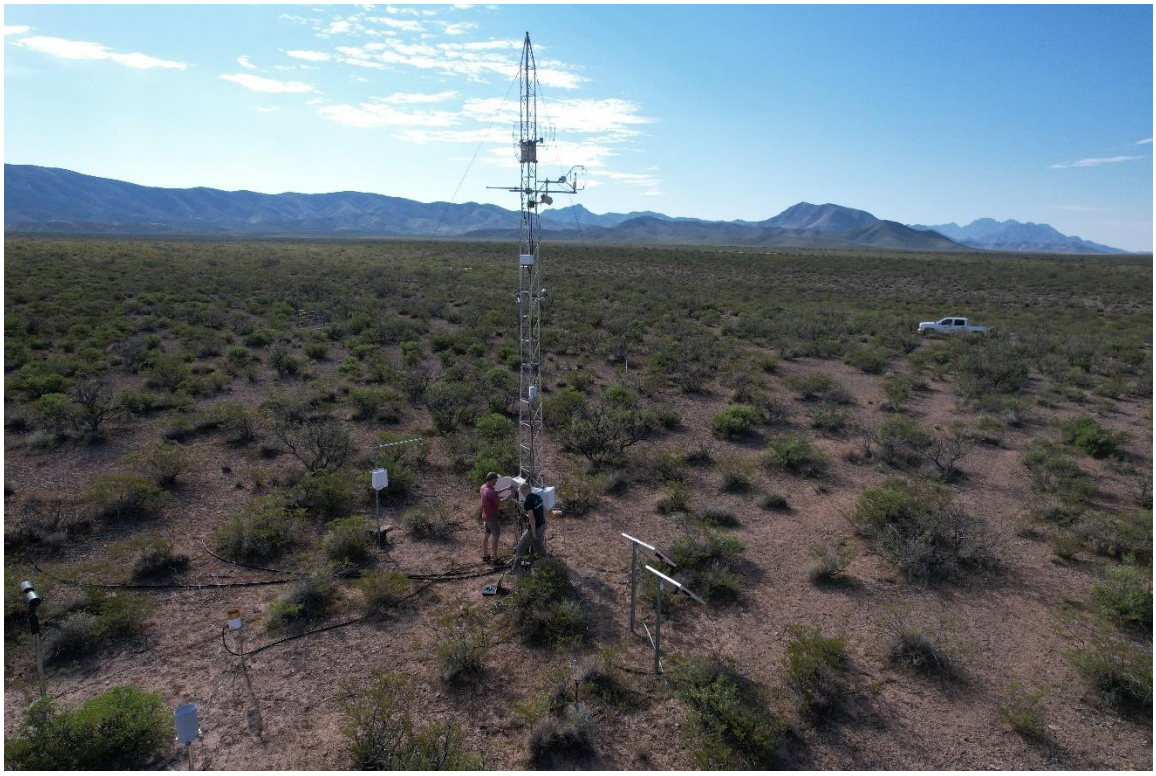

Figure L.3.15. Aerial view of the eddy covariance tower in the Tromble Weir watershed (Credit: Zhaocheng Wang).

Figure L.3.16. Santa Rita supercritical flume installed in the outlet of the Tromble Weir watershed (Credit: Turnbull et al., 2013).

Figure L.3.17. Phenology of the mixed shrubland in the Tromble Weir watershed showing the dry winter, the spring bloom and the green summer.

Figure L.3.18. Monsoon precipitation event over the San Andreas mountains near the Tromble Weir watershed.

Figure L.3.19. Monsoon precipitation event over the San Andreas mountains near the Tromble Weir watershed.

Figure L.3.20. Soil profile in one of the channels in the Tromble Weir watershed.

Figure L.3.21. Rain gauge and datalogger case in one of the soil moisture transects in the Tromble Weir watershed. (Credit: Zachary Keller).

Figure L.3.22. Photograph of an internal mini flume. (Credit: Zachary Keller).